Computationally Modelling Subcluster Mergers

Modelling Young Massive Cluster Formation: Mergers

By Jeremy Karam,

A Thesis Submitted to the School of Graduate Studies in the Partial Fulfillment of the Requirements for the Degree Master of Science

McMaster University

Master of Science (2021)

Hamilton, Ontario (Department of Physics and Astronomy)

TITLE: Modelling Young Massive Cluster Formation: Mergers

AUTHOR: Jeremy Karam (McMaster University)

SUPERVISOR: Dr. Alison Sills

NUMBER OF PAGES: xiv, 107

Abstract

Star cluster formation involves the conversion of molecular gas into stars inside giant molecular clouds (GMCs). Such a process involves many dynamical evolution mechanisms, including mergers between smaller star clusters (subclusters) on which we focus in this thesis. We take results of simulations performed by Howard et al. 2018 (H18) which found that young massive cluster (YMC) formation is heavily dependant on the process of subcluster mergers, and we simulate said mergers at higher resolution. Subclusters inside such GMC simulations are modelled using the sink particle prescription which does not resolve individual star particles or gas parcels inside the subcluster they represent. We employ a more controlled method in simulating subcluster mergers to better understand the response of the stellar and gas components of a subcluster from the merger process. To do this, we take the parameters of the sink particles created in H18 and set up spheres of stars and gas. We use the AMUSE framework to couple the N-body evolution of the stars to the smoothed particle hydrodynamics (SPH) evolution of the gas such that both components of a given cluster can realistically react to each other. We model 15 of these mergers and find that once the velocity at which the two clusters collide (collisional velocity) exceeds $\approx 10\text{kms}^{-1}$, the resultant cluster is not monolithic (i.e. it still contains two separate stellar components) while all other simulations merge into one monolithic stellar and gas component cluster. We also find that, regardless of the collisional velocity of masses of the component clusters, all resultant clusters lose a fraction of their stellar and gas mass. This fraction is directly proportional to the collisional velocity and is a discrepancy between the sink particle prescription (where all mass is contained inside a constant sink particle accretion radius) and real cluster mergers. A further discrepancy we find is that all simulations result in a cluster whose outermost regions are expanding and that the rate of this expansion is somewhat proportional to the collisional velocity of the merger. These results point to the inaccuracy of the sink particle prescription and allow us to develop tools to improve on it in future

simulations. Next, we fit commonly used analytical density profiles to both the stellar and gas component of our resultant clusters and find that, while they do not provide particularly excellent fits, they provide constraints on what is an acceptable fit. Lastly, we analyze the amount by which gas with potentially star forming densities increase due to the merger and we find that all mergers increase their star forming gas mass fraction by roughly 50 per cent implying that mergers may be an effective tool for triggering star formation.

Acknowledgements

I would first like to thank Dr. Alison Sills for her cosmic amount of patience with me. While there were many hurdles, she helped me stumble through to get to the other side. I would next like to thank Claude and Marta whose advice during work outings lead me down particularly fruitful paths. I would like to give a special thank you to Aiyman whose help was absolutely vital to some components of chapter 3. Also my parents, whose grocery trips helped me as I holed myself up to write this thesis. Lastly, I would like to thank Veronika, without whom I would probably have never finished this thesis.

Contents

List of Figures

List of Tables

Chapter 1

Introduction

Young massive clusters (YMCs) are dense collections of stars, sometimes embedded in clouds of molecular gas, with masses often $> 10^4 M_\odot$ and ages < 10Myr (Portegies Zwart et al. 2010). Early stages of the formation of such clusters is thought to involve the conversion of molecular gas into stars inside a giant cloud of molecular gas (GMC) through gravitational collapse in the densest regions of these clouds (Lada and Lada 2003). However, this conversion of molecular gas into stars may not be the only process required to form a bound cluster of stars on the mass scales of most YMCs. Namely, computational simulations show that *mergers* of stellar groups can help in reproducing oberved properties of YMCs. For example, simulations done by Fujii et al. (2012) show that the radial stellar density profile of the YMC R136 (seen in figure 1.1) can be reproduced through such mergers. Through computational simulations of GMC collapse under self-gravity, studies find that these small groups of stars (hereafter referred to as embedded subclusters) that form in dense regions of GMCs will eventually undergo multiple mergers, thus building up mass, and eventually leading to the formation of a YMC (Howard et al. 2018, hereafter referred to as H18). Furthermore, evidence for such mergers has also been found through observations. An example is the observation done by Zeidler et al. (2021) of the cluster Westerlund 2. The authors show that it can be

resolved as two distinct groups of stars containing cores with radial velocities towards one another, implying that a merger of these stellar groups will happen in the future.

The GMC environment in which these clusters form and grow, contains a large range of local densities, making it computationally expensive to simulate all scales at the same time in a single simulation (Stahler and Palla 2004, Bleuler and Teyssier 2014). To combat this, simulators have used *sink particles* as a representation of small subcluster scales (Banerjee and Kroupa 2017, Howard et al. 2018, Dobbs et al. 2020, Fukushima and Yajima 2021). Sink particles are simplified models of clusters which carry global parameters of the cluster they represent (for example, total stellar mass, total mass in stars and gas, position, and velocity of the subcluster) and are allowed to evolve in the simulation through interactions with other sinks, and the ambient molecular gas (Federrath et al. 2010). Each of these sink particles has an accretion radius unique to the simulation but shared among all sinks. Within this sink accretion radius lies the entirety of the mass of the subcluster. This sink radius also helps define how a given sink reacts with the simulation around it by acting as a distance within which ambient gas can be accreted onto the sink or two sinks can merge with one another.

The large scale GMC collapse simulations performed by H18 made use of this sink particle implementation. The authors created $10^7 M_\odot$ spherical GMCs and allowed it to evolve. Through turbulence induced as an initial condition in their simulations, dense filamentary structures began to appear, within which, sink particles began to form. These sink particles were used to represent subclusters in their GMC simulations. Though the sink was meant to represent a subcluster, it provided no information regarding the positions, or velocity of any of the individual stars or any of the gas that made up each subcluster.

Sink particles in H18 were prone to *prompt* mergers throughout the H18 simulations simulation. This lead the authors to conclude that subcluster mergers were an essential

part of the formation process of YMCs in GMCs. However, because the sink particle implementation prevents a simulator from resolving positions or velocities of the stars or gas in the subcluster, this method of YMC formation does not provide enough insight into how the individual components of the subcluster react to mergers with other subclusters. Though previous simulations have looked at subcluster mergers through a purely N-body analysis (Fujii et al. 2012), as well as through the coupling of N-body mechanics with an analytic potential function that represents a gas component (Banerjee and Kroupa 2015) there have yet to be studies focused on how both the stellar and gas component of an embedded subcluster react to mergers with other subclusters. As such, it is still unclear how each component of an embedded subcluster reacts to the merger process inside a GMC. The goal of this thesis is to fill in this gap in our understanding of YMC formation. We have simulated more realistic subcluster mergers through the coupling of a distinct stellar component and gas component.

Our method also serves as a means by which simulators can improve their sink particle prescription. By taking sink particles from H18 and modelling their mergers as a collection of stars and gas, we are able to analyze how some of the key assumptions made in the sink particle prescription hold. In this way, we provide simulators with the ability to maintain the use of sink particles in their large scale simulations, but suggest to them ways in which their sink models can be changed to more accurately model real subcluster mergers.

The remainder of chapter 1 is structured as follows: first, we review the basics of star cluster formation inside GMCs. We then discuss star cluster morphologies. We move on to outline various models of GMC simulations that deal with star cluster formation and evolution. Finally, we provide an in depth description of the H18 simulation.

FIGURE 1.1: Image of R136 (credit: NASA, ESA, F. Paresce (INAF-IASF, Bologna, Italy), R. O'Connell (University of Virginia, Charlottesville), and the Wide Field Camera 3 Science Oversight Committee)

1.1 Star Cluster Formation in Giant Molecular Clouds: Theory and Simulations

In this section, we set the stage for our project by discussing the current understanding of star and star cluster formation in GMCs.

1.1.1 Theory

GMCs are the hubs of star formation and star cluster formation (Lada and Lada (2003)). As a GMC is a collection of molecular gas, it is subject to many internal and external forces that govern its evolution. Such a self gravitating system may eventually collapse once internal, outwards pushing pressures can no longer hold up against inward pushing gravitational contraction. Under such gravitational influence, collapse takes place on the *free-fall* timescale. This can be defined as

$$t_{ff} = \sqrt{\frac{3\pi}{32G\bar{\rho}}} \tag{1.1}$$

where $\bar{\rho}$ is the average density and G is Newton's gravitational constant. This instability between gravitational forces pulling the cloud inwards towards collapse and kinetic energy working to keep the cloud from collapsing can be summarized in the following equation (Bertoldi and McKee 1992):

$$\alpha = \frac{T}{|W|} \approx a\frac{5\sigma^2 R}{GM} \tag{1.2}$$

where σ is the velocity dispersion of the cloud, M is its mass, a is a parameter that accounts for deviations from spherical symmetry (but is often set to $a \approx 1$), T is the kinetic energy of the cloud, and W is its potential energy. Alpha is known as the *virial parameter*. For spherically symmetric systems, the limits on this parameter help to quantify the future state of the GMC: $\alpha = 1$ is a complete balance of outward pressures

with inward gravity, $\alpha < 1$ represents the regime in which the gravitational potential outmatches the kinetic energy (the process that leads to this collapse is known as *Jeans instability*), and $\alpha > 1$ is the regime in which the kinetic energy surpasses the potential energy.

Turbulence further complicates the situation by working against gravity as a form of kinetic energy to shape the GMC. As a GMC collapses, dense filamentary structure becomes visible (André et al. 2014). Within these filaments, observers have noticed dense cores which can go on to form individual stars (Könyves et al. 2010). As the GMC evolves, its continued collapse may cause these dense filaments to feed material into the accreting protostellar core which, in turn, increases its mass. One factor that helps determine the efficiency with which a prestellar core is converted into stellar mass is the strength of the gas ejected by that protostar as a consequence of conservation of angular momentum. These ejecta are known as *protostellar outflows*. Processes such as these can affect the final mass of the star that forms (Matzner and McKee 2000, Guszejnov et al. 2020). This implies that stars of varying masses can form in the filaments of collapsing GMCs. A schematic of this star formation event can be seen in figure 1.2. At the densest intersections of filaments, this can lead to the formation of groups of stars bound together gravitationally rather than just a single star. However, this does not tell us how very massive collections of stars (e.g. YMCs) can form in the GMC environment. To come to an answer to this question, we can look towards numerical simulations of GMC collapse that include a star cluster formation prescription.

1.1.2 Simulations

Hydrodynamical simulations of GMC collapse show similar results to one another regarding the location of star forming regions, consistent with theory stated above. Whether simulators trigger turbulence in their GMC through colliding two cylindrical gas flows

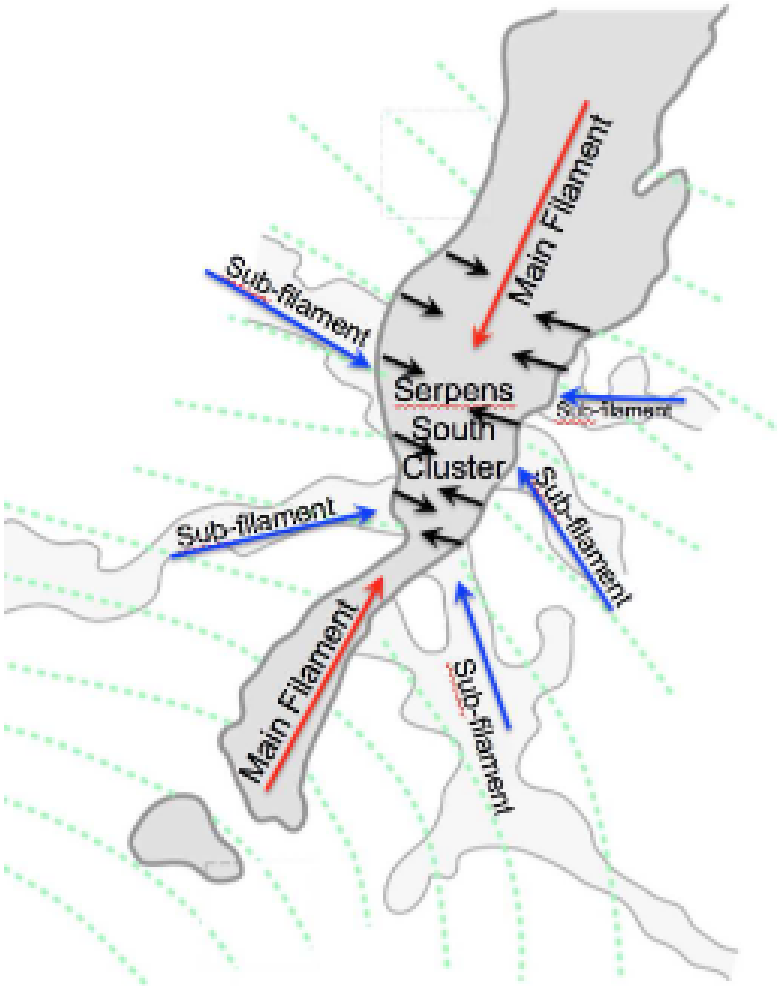

FIGURE 1.2: A schematic of the star formation process present in the Serpens South Cluster. Arrows mark velocity gradient with red showing accretion from host filament, blue showing infall from surrounding cloud, and black showing radial contraction of the host filament (André et al. 2014 and references therein). Used with permissions from the University of Arizona Press ©.

(e.g. Vázquez-Semadeni et al. 2017) or through inducing turbulence via a turbulent velocity spectrum (e.g. Fukushima and Yajima 2021), dense filamentary structure is ubiquitous across these simulations. Many GMC collapse simulations have tried to bridge the evolutionary gap between groups of stars and massive star clusters. An example of such a simulation is that done by Chen et al. (2021). Here, the authors tested various initial GMC density distributions to understand which ones lead to the formation of a massive cluster. The authors find that the formation of their most massive cluster by the end of most of their simulations is heavily dependant on the merging of smaller subclusters along dense filaments in their cloud. This has also been found in simulations done by Lahén et al. (2020a) who analyze the results of a dwarf galaxy merger simulation carried out by Lahén et al. (2020b) and find that a YMC forms through mergers of smaller subcluster, in line with observations that find YMCs often form in active galactic mergers such as the Antannae system due to the extremely dense regions in an active merger (Zhang et al. 2001). Though the formation mechanisms of massive clusters in these GMC simulations may be well constrained through these methods, none were able to constrain the reaction of the subclusters to the merger process as they evolve in the GMC simulation. This is because, as we reach star cluster densities, the density contrast between star forming regions and those regions that have yet to get to star forming densities inside the GMC becomes extremely high. This makes it difficult to simulate both regimes in one simulation. Mathematically, this can be described using the *Courant condition* (Courant et al. 1967) which states:

$$\Delta t \leq \frac{\Delta x}{c_s} \tag{1.3}$$

where Δt is the maximum timestep, Δx is the spatial resolution of the region of interest, and c_s is the local sound speed. In words, this equation illustrates the need for lower timesteps in regions that require higher spatial resolution (small Δx) such as dense star forming regions in GMCs which eventually becomes far too computationally expensive.

Subgrid models help to solve this problem by representing a newly formed subcluster as a set of parameters that describe the subcluster (i.e. its mass, position in the GMC, and velocity) rather than a collection of individual stellar particles, thus drastically shortening computer runtimes. An example of such a subgrid model is the sink particle prescription outlined in Federrath et al. (2010). In this model, sink particles are point particles in GMC simulations that are allowed to move freely throughout the simulation box and interact with gas and other sinks around it. As outlined by Federrath et al. (2010), a sink particle is formed once a patch of gas in the simulation satisfies the following conditions: it must be above a density threshold set by the user, it must be at the highest level of refinement allowed by the simulation code, it must be Jeans unstable (strong gravitational forces pushing towards collapse against weak outwards pressure), and finally, it must not be within one *accretion radius* of another sink particle (else it will be accreted onto that nearby sink particle). The accretion radius associated with these sink particles is the means by which sink mergers and gas accretion onto sinks is mediated. It is done in the following ways:

- Firstly, as a sink particle moves through the simulation and interacts with surrounding gas, it has the chance to accrete that gas if the gas is within the sink particle's r_{sink}, and if the gas is gravitationally bound to the sink particle. *The resulting total gas mass in that given sink particle increases by an amount directly equivalent to the newly accreted gas mass.*

- Second, if two sink particles are within one r_{sink} from each other and are gravitationally bound to each other, they merge into one. The resultant sink particle's mass is the sum of that of the parent sinks and the resultant sink's velocity is taken as the centre of mass velocity of the merger. As sink particles mask the physics of the stellar and gas component of the subcluster they represent, *how the stars and gas react to subcluster mergers is unknown.*

Despite these caveats, the increased computational efficiency afforded by the sink particle perscription is often worth it when it comes to simulating the collapse of very large mass GMCs. To better understand the specific physics being masked by these sink particles, and why it is important to resolve them as a collection of stars and gas, we take our discussion to the next scale down and journey through star clusters.

1.2 Star Clusters

The definition of a star cluster has been widely discussed since the early working definition given by Trumpler (1930) which states that: a star cluster must be a collection of at least 12 stars and its overall shape and size can be determined by its gravitational potential. More recently, star cluster definitions have considered the boundedness of the group of stars to differentiate from an association of field stars (Portegies Zwart et al. 2010). Furthermore, studies have shown that a star cluster's shape is not only affected by the mass of its member stars, but of the environment in which the cluster is located. As star clusters are gravitational systems, the radial distribution of their stellar component is subject to change under the influence of dynamical interactions between the stellar members. This change in distribution may lead to the unbinding, or removal, of stellar members from the host cluster.

1.2.1 Dynamics of Stellar Systems

A method by which stellar systems can lose stellar mass (through the unbinding of stellar members from the host system) is through *two-body relaxation* which is the process by which a single star's trajectory is altered by the presence of another single star through close encounters (Spitzer 1940). Close encounters such as these lead to an exchange of energy between stars and, eventually, stars that lie on the tail end of the energy distribution of the cluster are given enough kinetic energy to become unbound from the host cluster in a process known as stellar *evaporation*. Therefore, we can use the timescale

of evaporation to understand how long a star cluster may survive before gravitational effects cause it to evaporate.

To understand the timescales on which this dynamical evolution takes place, we begin by defining the half-mass relaxation time using Spitzer and Hart (1971):

$$t_{rh} = 0.138 \frac{M^{1/2} r_{hm}^{3/2}}{G^{1/2} m_* \ln(\Lambda)} \tag{1.4}$$

where M is the cluster mass, r_{hm} is the radius which encloses half of the cluster mass, G is Newton's gravitational constant, m_* is the average stellar mass of the cluster and $\Lambda \approx 0.4N$ where N is the total number of stars in the system. While the relaxation time is the time it takes for a star in the cluster to lose all memory of its initial orbit due to gravitational interactions with surrounding stars, t_{rh} is this time at the half mass radius r_{hm} of the cluster. Numerical integrations done by Gnedin and Ostriker (1997) find that the timescale for evaporation to destroy a star cluster is related to the concentration of that cluster $c = \log(r_t/r_c)$ but, on average, find $t_{ev} \approx 30 t_{rh}$ in the presence of a galactic potential. Lastly, the relaxation time t_r can be related to the *crossing time* t_{cr} of the system (the amount of time it takes on average for a star to travel from one side of the cluster to the other) using

$$t_{cr} \approx \frac{7 \ln \Lambda}{N} t_r \tag{1.5}$$

A contributing factor to the complexity of gravitational interactions in stellar systems such as star clusters is the fact that stars of varying masses can reside in the same cluster. To better understand the distribution of stellar masses inside a star cluster, a stellar *initial mass function* (IMF) can be used. The IMF is a probability distribution function that can be applied to a set of particles to randomly distribute to them mass. Many forms of the IMF have been introduced beginning in 1955 with the Salpeter (1955) IMF. However, the form of this IMF extended to infinity as one looked towards lower mass

stars. In other words, the Salpeter IMF too heavily favoured the production of low mass stars.

To correct this, Kroupa (2001) introduced a form of the IMF that splits the mass range into three regions, each with their own slope. The Kroupa (2001) IMF takes the form:

$$\epsilon(m) = m^{-a} \tag{1.6}$$

with

$$a = 0.3 \; for \; m < 0.08 M_{\odot}$$

$$a = 1.3 \; for \; 0.08 M_{\odot} < m < 0.5 M_{\odot}$$

$$a = 2.3 \; for \; m > 0.5$$

The Kroupa and the similar looking Chabrier (2005) IMFs are commonly used in numerical simulations to apply masses to component stars in star clusters.

1.2.2 Star Cluster Morphology

Star cluster morphology is not always perfectly spherical and such deviations from spherical symmetry can have an impact on the star cluster's evolution (e.g. Parker and Meyer 2012) making it important to resolve such intricacies in star cluster simulations. Kuhn et al. (2014) studied clusters in nearby massive star forming regions through the MYSTIX (Feigelson et al. 2013) sample. They created 2D surface density maps for young stars in each of the star forming regions and found that they can be grouped morphologically using fitted ellipses of the stellar density. Many of star clusters in their sample had morphologies that were not spherical.

Though a star cluster can begin with a non-spherical morphology, it may evolve into a smooth, relaxed state (Cartwright and Whitworth 2004, Schmeja and Klessen 2006).

For example, N-body simulations done by Allison et al. (2010) show that initially subvirial clumpy clusters (clusters containing subclumps with one larger host cluster) can undergo subclump mergers and lead to massive runaway stars similar to the results obtained by Fujii et al. 2012. Such signatures can not be obtained through the evolution of more spherical clusters on short timescales. Although, embedded subclusters contain background gas along with a stellar component which was not modelled in these simulations. Simulations performed by Sills et al. 2018 included gas and focused on the evolution of the linear chain of subclumps DR 21 as seen in figure 1.3 and found that all subclusters had completely merged promptly within 1Myr to form something more resembling a smooth isolated cluster.

1.3 H18 Simulations

In this section, we discuss Howard et al. (2018) in depth. We talk about the methods used to set up their simulations as well as some key results.

1.3.1 Methods

Howard et al. (2018) (H18) carried out radiation hydrodynamics simulations using the FLASH (Fryxell et al. 2000) code. These simulations studied the evolution of initially spherical $10^7 M_\odot$ GMCs with a virial parameter of $\alpha = 3$. This is the upper limit of GMC mass in the authors suite of GMC collapse simulations. The authors induced turbulence and these random velocities lead to shocks withing the GMC along which star clusters began to form as sink particles though their choice of α led to dispersion in the outer regions of the cloud. The goal of this study was to understand the formation of Young Massive Clusters (YMCs) in GMCs. Throughout the simulations, the most massive sink formed would accrete much of the mass around it and merge with smaller sink particles thus growing in size. An example of the growth of clusters through accretion and mergers in two of their simulations can be seen in figure 1.4. The blue star in this figure shows

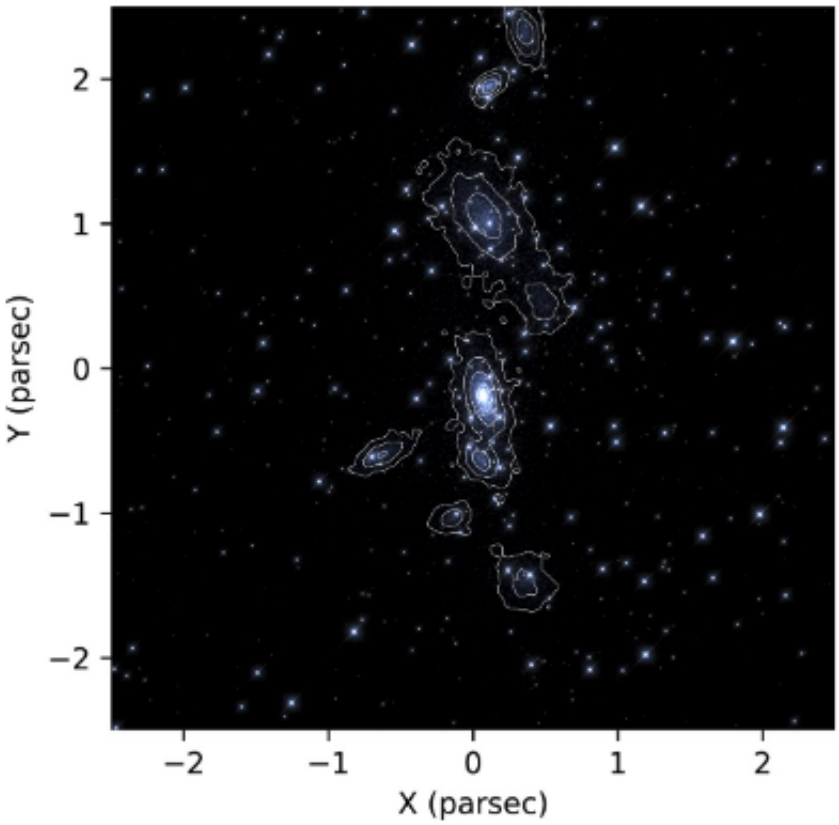

FIGURE 1.3: Simulated initial distribution of stars and gas for the cluster DR21. Stars are shown as blue/white objects while gas distribution can be seen through contour lines representing its surface density. (Figure 1 from Sills et al. (2018))

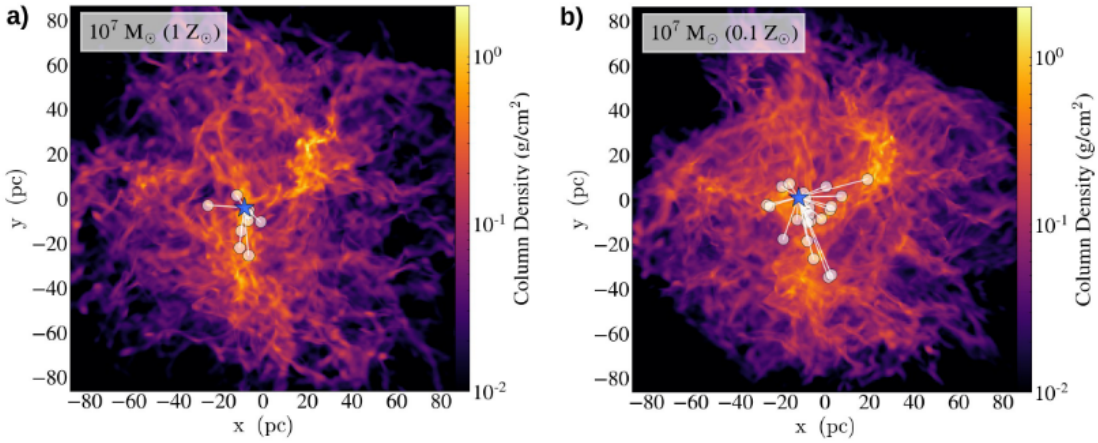

FIGURE 1.4: Column density maps for the GMCs from H18. Snapshots are taken at $t = 1.54$Myr which corresponds to the time when, what will become the most massive cluster (blue star), forms. White circles represent smaller clusters that will eventually merge with the blue star (Howard et al. 2018).

the most massive sink particle formed in their two simulations. This most massive sink forms in the densest filament near the centre of the collapsing GMC and smaller sink particles form around it in less dense filaments (shown as white circles in the figure). By the end of these simulations, many of the smaller sink particles will merge with the largest one and a YMC sized sink will form.

Once a sink particle is placed, a subgrid model is used to describe star formation inside that particle: the sink particle is assumed to be comprised solely of gas initially, and the authors convert that gas into stars such that the stellar mass distribution follows a Chabrier (2005) IMF. In agreement with observations of local star forming clumps in the Milky Way done by Lada and Lada (2003), the authors convert 20 per cent of this gas mass into stellar mass. This conversion takes place once every $t_{ff} \approx 0.36 Myr$ so that gas that is accreted onto the sink at later times can contribute to the sink's stellar mass and the stellar mass of each sink is not constant throughout the simulation.

1.3.2 H18 Results

The H18 simulations resulted in the formation of YMCs in their high column density filaments through subcluster mergers and gas accretion (see figure 1.4). These YMCs continue to absorb smaller subclusters and accrete filamentary gas. The merger tree highlights the importance of subcluster mergers in the creation of YMCs through GMC collapse. Connected by the dashed line on the bottom of each panel is the largest cluster in their simulation. The shaded region represents the percentage of the mass of that sink particle than can be attributed to mergers with other sinks. We can therefore see that by the end of the simulations, $\approx 45\% - 50\%$ of the final YMC's mass is owed to mergers. As expected as well, mergers are more plentiful in the $0.1Z_{\odot}$ case because lower metallicity leads to less gas dispersal around sink particles which allows for more sinks to form and in turn merge with other sinks.

By combining the results from this study and previous simulations of $10^{4-6}M_{\odot}$ GMCs (Howard et al. 2017, Howard et al. 2018), H18 noted a strong power law relationship between the initial mass of their GMC and the mass of the most massive YMC formed by the end of their simulations. This relationship lasts over 3 orders of magnitude of GMC masses.

Hierachical merging happens throughout all regions of their GMC as it collapses. As subclusters travel along filaments and accrete gas, they merge and build up to a YMC. This merger and gas accretion process occurs mostly in filaments along which these subclusters travel. The results of the H18 simulation therefore lend themselves well to the idea that *subcluster mergers are vital in the formation of YMCs in GMCs*. As such, it is crucial for us to understand the details of this astrophysical process.

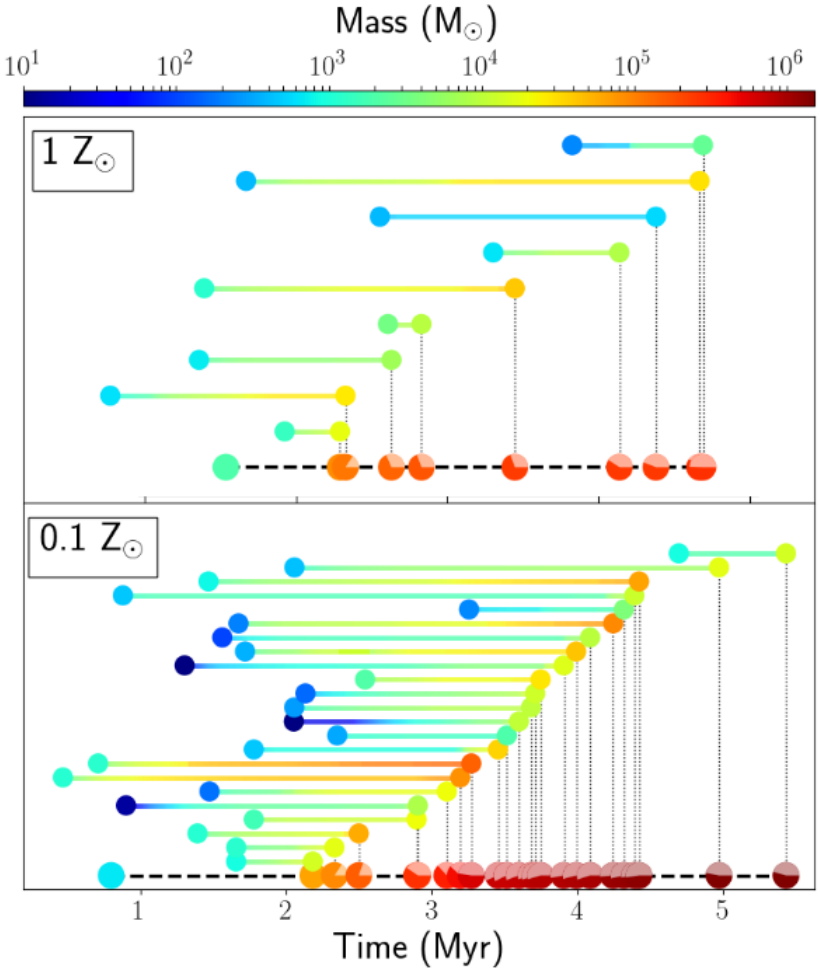

FIGURE 1.5: Merger trees, where x-axis shows time, for the YMC in the $1Z_\odot$ and $0.1Z_\odot$ H18 simulations respectively. Each circle represents a subcluster and the bottom circles connected by dashed lines represent the most massive sink particles in each respective simulation. Each vertical dotted line shows a merger between one sink and the most massive sink. Sinks grow in mass through gas accretion as can be seen by looking at the colour gradient connecting each sink to its vertical dotted line. The lighter shaded region in the most massive sink represents the fraction of that mass that can be attributed to sink particle mergers (Howard et al. 2018).

1.4 Thesis Overview

In this thesis, we model star clusters as discrete collections of stars and gas. We simulate pairs of star clusters and investigate the properties pertaining to bound members, cluster growth, and density profiles of the resultant cluster. We have looked at a number of star cluster pairs from the H18 simulations as well as mergers that are not present in H18 but involve the merging of sinks from H18. In chapter 2, we discuss the numerical methods used for our simulations. In chapter 3, we present results from our simulations. In chapter 4, we discuss conclusions and outline avenues for future work.

Chapter 2

Computational Methods

Our star cluster model involves the evolution both the stellar and gas components present in the cluster. To do this, we employ the Astrophysical Multipurpose Software Environment (AMUSE) (Portegies Zwart et al. 2009, Pelupessy et al. 2013, Portegies Zwart et al. 2013, Portegies Zwart and McMillan 2018) which is a collection of publicly available community codes, each able to model specific astrophysical processes. We use the `GADGET-2` (Springel 2005) smoothed particle hydrodynamics (SPH) code to model our cluster's gas component, and the `hermite0` (Makino and Aarseth 1992) N-body dynamics code to model our cluster's stellar component. We use the `BRIDGE` (Fujii et al. 2007) scheme to connect both components such that they can react to each other in the simulation.

We begin this chapter with a brief discussion of AMUSE including how the `BRIDGE` scheme communicates with the two components of our star cluster. We then move to a brief review of SPH and N-body mechanics. To end the chapter, we introduce analysis tools that will be important in guiding our physical understanding of our results.

2.1 AMUSE

AMUSE is a software environment that contains within it many codes that allow one to simulate a variety of astronomical phenomena ranging from processes involving stellar evolution, to dynamical interactions, and hydrodynamics. The simulation codes are written mainly in `C` and `fortran` by physicists in the field, yet are all wrapped neatly in `python` syntax. This allows the user access to complicated codes in a simpler environment. Each of these astronomical phenomena have associated with them many solvers and it is the user's job to pick which one best matches their needs. One can then call the respective codes from a master `python` script along with any other conditions necessary to their specific code.

With the vast collection of codes in AMUSE, it is only natural to wonder if there is a way for them to communicate with one another. The example pertinent to our project is the coupling hydrodynamics (gas particles) to N-body dynamics (star particles). For the codes responsible for these processes to communicate to one another, we use the BRIDGE scheme (Fujii et al. 2007) found in AMUSE. This allows outputs from the hydrodynamics solver to be fed to the N-body dynamics solver so that the gas properties (particle locations, velocities, etc.) can affect the star particles (and vice versa). We explain this scheme below.

2.1.1 BRIDGE

The BRIDGE scheme provides a method by which two systems with differing internal dynamics can communicate with one another in a single code. The BRIDGE scheme allows both systems to evolve independently of one another and to occasionally communicate with one another by means of periodic velocity kicks.

For our purposes, we are using BRIDGE to couple two codes in AMUSE (our N-body and SPH solvers) into one single code which involves the splitting of the N-body and

hydrodynamics operators such that they can evolve on their own before communicating with one another. Derivation of this method through operators relies on the formalism introduced by Wisdom and Holman (1991) and Duncan et al. (1998) which takes the Hamiltonian of an entire system and splits it into components representative of the two subsystems (in our case, stars and gas). If we consider the Hamiltonian operator of our entire system, we can write it as a combination of the stellar dynamics Hamiltonian H_s and the hydrodynamics Hamiltonian H_g as follows:

$$H_{tot} = H_s + H_g + H_{s,g} \tag{2.1}$$

where $H_{s,g}$ represents the interaction Hamiltonian between the two subsystems. H_g includes the total evolution of the gas system, including shocks and pressure forces (these are taken into account in the `GADGET-2` code as described in section 2.2). The formal time evolution of this system can then be written using

$$e^{\tau \vec{H}} = e^{\tau/2\vec{H_{s,g}}} e^{\tau(\vec{H_s}+\vec{H_g})} e^{\tau/2\vec{H_{s,g}}} \tag{2.2}$$

where the vector symbol has now turned our each exponential into an operator. In words, the right hand side of this equation represents evolving the system under the influence of $H_{s,g}$ (interactions between the stars and gas) for half a time-step, then moving onto the stellar component H_s and gas component H_g evolutions for a full timestep, and finally, the interaction once more for half a timestep.

In practice, the above formalism requires the gas and stars to evolve on their own separately using either the `hermite0` scheme or `GADGET-2` scheme respectively after initially interacting with one another. In order, the BRIDGE scheme is carried out in the following way: first, create a tree to calculate the accelerations $\mathbf{a}_{g \longrightarrow s,0}$ and $\mathbf{a}_{s \longrightarrow g,0}$ between the stellar and gas components of the subcluster. We use the `AMUSE` code `BHTree`

written by Jun Makino using Barnes and Hut (1986) to create this tree. Next, use

$$\mathbf{v'}_{s,0} = \mathbf{v}_{s,0} + \frac{1}{2}\Delta t \mathbf{a}_{g\longrightarrow s,0} \tag{2.3}$$

to provide a velocity kick to the stellar velocities $\mathbf{v}_{s,0}$ to obtain a new velocity for each star $\mathbf{v'}_{s,0}$. Similarly, the gas velocities are updated using

$$\mathbf{v}_{g,\frac{1}{2}} = \mathbf{v}_{g,0} + \frac{1}{2}\Delta t \mathbf{a}_{s\longrightarrow g,0} \tag{2.4}$$

For the next time step, the stellar and gas positions and velocities are evolved on their own using `hermite0` for the stars and `GADGET-2` for the gas and using the outputs of the above equations. To finish the timestep, BRIDGE applies one more velocity kick after having calculated the new accelerations $\mathbf{a}_{g\longrightarrow s,1}$ and $\mathbf{a}_{s\longrightarrow g,1}$. The forms of these kicks follow

$$\mathbf{v}_{s,1} = \mathbf{v'}_{s,1} + \frac{1}{2}\Delta t \mathbf{a}_{g\longrightarrow s,1} \tag{2.5}$$

and

$$\mathbf{v}_{g,1} = \mathbf{v'}_{g,1} + \frac{1}{2}\Delta t \mathbf{a}_{s\longrightarrow g,1} \tag{2.6}$$

where $\mathbf{v'}_{s,1}$ and $\mathbf{v'}_{g,1}$ are the velocities obtained from the `hermite0` and `GADGET-2` N-body and hydro solvers for the stars and gas respectively. After this last kick, the timestep is over and the process repeats. The user must specify the frequency of interactions between the two subsystems by means of a bridge timestep Δt_B so that the code knows how long to evolve the stars and gas separately before letting them communicate. Through initial tests, we find that the optimal bridge timestep for our system is $\Delta t_B \approx 800$yr because it does the best job at conserving total energy throughout the simulation.

Now we will discuss how the evolution of these star and gas particles are performed in their own respective solver after their initial interaction with each other and before their final one in the BRIDGE scheme. We begin with the gas particles and smoothed

particle hydrodynamics (SPH).

2.2 Smoothed Particle Hydrodynamics (SPH)

SPH is a method of simulating the evolution of fluids that treats the fluid as a collection of discrete particles, not confined to a grid (Monaghan 1992). However, hydrodynamics requires that each particle be described as a smoothed out distribution of density rather than a point particle. Because of this, each SPH particle represents a smoothed density distribution given by

$$\rho_j(\mathbf{r}) = m_j W(|\mathbf{r} - \mathbf{r_j}|, h) \tag{2.7}$$

where ρ_j is the contribution to the total density at some position $\mathbf{r}$ by a particle of mass m_j. The function $W(\mathbf{r}, h)$ is know as the smoothing kernel and allows us to understand the mass distribution of particle j. Therefore, particles can interact with one another if they are inside each others kernel function. Originally, kernels took on a Gaussian shape whose variance was given by h and whose mean was 0 (Gingold and Monaghan 1977). However, because Gaussians extend to infinity, this was dropped in favour of a kernel that satisfies contact support: meaning that particles can be outside the influence of one another, and therefore have no interactions thus increasing computational efficiency. This is the case if the separation of the particles is larger than the extent of the kernel function $|\mathbf{r}| > h$. A good choice of kernel function is therefore the spline kernel described as follows

$$W(\mathbf{r}, h) = \frac{8}{\pi h^3} \begin{cases} 1 - 6(\frac{r}{h})^2 + 6(\frac{r}{h})^3 & 0 \leq \frac{r}{h} \leq \frac{1}{2} \\ 2(1 - \frac{r}{h})^3 & \frac{1}{2} < \frac{r}{h} \leq 1 \\ 0 & \frac{r}{h} > 1 \end{cases} \tag{2.8}$$

because it imposes the limit that $W = 0$ for particles whose position away from the particle of interest is larger than h. This spline kernel is used in the SPH code `GADGET-2` (Springel 2005) which we use to model our cluster's gas evolution.

With a given kernel function, we can find other physical quantities related to the fluid by means of an interpolating function. Following Monaghan (1992), the integral interpolant of a function $A(\mathbf{r})$ is given by

$$A(\mathbf{r}) = \int A(\mathbf{r}')W(\mathbf{r} - \mathbf{r}', h)d\mathbf{r}' \tag{2.9}$$

where the integral is done over all space. To apply this to numerical work, we can rewrite the above equation as

$$A(\mathbf{r}) = \Sigma_{j=1}^{N} m_j \frac{A_j}{\rho_j} W(|\mathbf{r} - \mathbf{r_j}|, h) \tag{2.10}$$

In practice, both the smoothing lengths h_j and the density ρ_j of the jth particle must obey the implicit equation

$$\frac{4\pi}{3} h_j^3 \rho_j = \bar{m} N_{SPH} = M_{SPH} \tag{2.11}$$

where $\bar{m}$ is the average mass of the particles, and N_{SPH} is the number of neighbours. This implies the need for an adaptive h_i throughout the simulations as densities around each particle change.

One can see from the above equations that the choice of SPH particle mass m_j is important in determining the density at a given point the simulation and, in turn, the resolution of the simulation. By taking a fixed amount of total gas mass, and evenly distributing particles, all of mass m_j in the simulation, one can alter the resolution of their simulation by means of smaller inter-particle separations as long as the width of

the kernel h is defined such that a fixed mass is contained in one smoothing volume (Springel and Hernquist 2002).

To find the equations of motion of each gas particle, Springel and Hernquist (2002) show that the Lagrangian of the entire system (considering the kinetic and thermal energies) combined with the constraints put on the system through equation 2.11, lead to

$$\frac{d\mathbf{v_i}}{dt} = -\sum_{j=1}^{N} m_j [f_i \frac{P_i}{\rho_i^2} \nabla_i W_{ij}(h_i) + f_j \frac{P_j}{\rho_j^2} \nabla_i W_{ij}(h_j)] \tag{2.12}$$

where P_i is the pressure of the ith particle, $W_{ij}(h) = W(|\mathbf{r_i} - \mathbf{r_j}|, h)$ and

$$f_i = [1 + \frac{h_i}{3\rho_i} \frac{\delta \rho_i}{\delta h_i}]^{-1} \tag{2.13}$$

obtained from the Lagrangian multipliers provided by the constraints in equation 2.11.

In order to account for any shocks that may occur throughout the gaseous component of our star clusters, it is important to understand how `GADGET-2` implements *artificial viscosity* in their simulation code.

Physically, a shock is not an infinitely sharp discontinuity. Rather, it takes place over a very small range (only a few particle mean free paths) making it difficult to resolve computationally. In order to broaden the shock front such that it is able to be resolved in numerical codes, artificial viscosity is used (given by Π_{ij}). As seen in Springel (2005), the viscous force is given by

$$\frac{dv_j}{dt}_{visc} = -\sum_{i=1}^{N} m_i \Pi_{ji} \nabla_j \bar{W}_{ji} \tag{2.14}$$

Here, Π_{ji} is only non-zero when particles are travelling towards one another in physical space. This constraint allows the artificial viscosity to only be used during shocks, and

not appear in other parts of the simulation. This can be defined mathematically as:

$$\Pi_{ji} = -\frac{\alpha}{2}\frac{(c_j + c_i - 3w_{ji})w_{ji}}{\rho_{ji}} \tag{2.15}$$

only if $\mathbf{v}_{ji} \cdot \mathbf{r}_{ji} < 0$ where v_{ji} and r_{ji} are the differences in particle velocity and position respectively between the jth and ith particle. In the above equation, c_j and c_i are the sound speeds associated with the jth and ith gas particles, and $w_{ji} = \frac{\mathbf{v}_{ji}\cdot\mathbf{r}_{ji}}{|\mathbf{r}_{ji}|}$. Here, α is a free parameter that regulates the strength of the viscosity. With this, shocks in the gas component of our cluster can be handled inside the `GADGET-2` code.

2.3 N-Body Mechanics

We now move onto a discussion regarding the means by which the gravitational interactions between our star particles our modelled in our star cluster simulations. We use a fourth order Hermite Scheme (Makino and Aarseth 1992) to calculate gravitational interactions between the stars in our simulations. The outline of this scheme is described here.

Each particle is given its own time t_i, timestep Δt_i, position $\mathbf{x_i}$, velocity $\mathbf{v_i}$, acceleration $\mathbf{a_i}$, and jerk $\dot{\mathbf{a}}_\mathbf{i}$ at a given time in the simulation. The minimum $t_i + \Delta t_i$ associated with these particles is selected as the global time (set as t_g) for all particles (including the particle associated with t_g) in the simulation and the positions, and velocities of all particles are calculated at this timestep using

$$\mathbf{x_{i,p}} = \mathbf{x_{i,0}} + \Delta t_i \mathbf{v_{i,0}} + \frac{1}{2}\Delta t_i^2 \mathbf{a_{i,0}} + \frac{1}{6}\Delta t_i^3 \dot{\mathbf{a}}_\mathbf{i,0} \tag{2.16}$$

$$\mathbf{v_{i,p}} = \mathbf{v_{i,0}} + \Delta t_i \mathbf{a_{i,0}} + \frac{1}{2}\Delta t_i^2 \dot{\mathbf{a}}_\mathbf{i,0} \tag{2.17}$$

where $\Delta t_i = t_g - t_i$. To update the particle associated with t_g, we must calculate the acceleration and jerk felt from all other particles in the simulation. This is done using

$$\mathbf{a_j} = \sum_i^N G m_i \frac{\mathbf{x_{ij}}}{(x_{ij}^2 + \epsilon^2)^{3/2}} \tag{2.18}$$

$$\dot{\mathbf{a}}_\mathbf{j} = \frac{d\mathbf{a_j}}{dt} = \sum_i^N G m_i [\frac{\mathbf{v_{ij}}}{(x_{ig}^2 + \epsilon^2)^{3/2}} + \frac{3(\mathbf{v_{ig}} \cdot \mathbf{x_{ij}})\mathbf{x_{ij}}}{(x_{ij}^2 + \epsilon^2)^{5/2}}] \tag{2.19}$$

In the above equations, $\mathbf{x_{ij}} = \mathbf{x_{i,p}} - \mathbf{x_{j,p}}$ and $\mathbf{v_{ij}} = \mathbf{v_{i,p}} - \mathbf{v_{j,p}}$. ϵ is the softening parameter introduced to prevent acceleration calculations from producing values that tend to infinity. Moving now to the corrector component of the scheme, we can use the third order Hermite interpolation, defined as

$$\mathbf{a_j}(t) = \mathbf{a_{0,j}} + \Delta t \dot{\mathbf{a}}_\mathbf{0,j} + \frac{\Delta t^2}{2}\mathbf{a}^{(\mathbf{2})}_\mathbf{0,j} + \frac{\Delta t^3}{6}\mathbf{a}^{(\mathbf{3})}_\mathbf{0,j} \tag{2.20}$$

to find the second and third derivatives of the acceleration vector.

$$\mathbf{a}^{(\mathbf{2})}_\mathbf{0,j} = \frac{-6(\mathbf{a_{0,j}} - \mathbf{a_{1,j}}) - \Delta t_j(4\dot{\mathbf{a}}_\mathbf{0,j} + 2\dot{\mathbf{a}}_\mathbf{1,j})}{\Delta t_j^2} \tag{2.21}$$

$$\mathbf{a}^{(\mathbf{3})}_\mathbf{0,j} = \frac{12(\mathbf{a_{0,j}} - \mathbf{a_{1,j}}) + 6\Delta t_j(\dot{\mathbf{a}}_\mathbf{0,j} + \dot{\mathbf{a}}_\mathbf{1,j})}{\Delta t_j^3} \tag{2.22}$$

The final step is to add these corrections to the position and velocity using

$$\mathbf{x_j}(t_j + \Delta t_j) = \mathbf{x_{j,p}} + \frac{\Delta t_j^4}{24}\mathbf{a}^{(\mathbf{2})}_\mathbf{0,j} + \frac{\Delta t_j^5}{120}\mathbf{a}^{(\mathbf{3})}_\mathbf{0,j} \tag{2.23}$$

$$\mathbf{v_j}(t_j + \Delta t_j) = \mathbf{v_{j,p}} + \frac{\Delta t_j^3}{6}\mathbf{a}^{(\mathbf{2})}_\mathbf{0,j} + \frac{\Delta t_j^4}{24}\mathbf{a}^{(\mathbf{3})}_\mathbf{0,j} \tag{2.24}$$

and update the timestep using

$$\Delta t_j = \sqrt{\eta \frac{|\mathbf{a_{1,j}}||\mathbf{a^{(2)}_{1,j}}| + |\dot{\mathbf{a}}_{\mathbf{1,j}}|^2}{|\dot{\mathbf{a}}_{\mathbf{1,j}}||\mathbf{a^{(3)}_{1,j}}| + |\mathbf{a^{(2)}_{1,j}}|^2}} \tag{2.25}$$

η is a control parameter to control the accuracy of the new timestep. The second order derivative in the above equation can be calculated using

$$\mathbf{a^{(2)}_{1,j}} = \mathbf{a^{(2)}_{0,j}} + \Delta t_j \mathbf{a^{(3)}_{0,j}} \tag{2.26}$$

Note as well that because we are using a third order interpolation scheme, $\mathbf{a^{(3)}_{1,j}} = \mathbf{a^{(3)}_{0,j}}$.

2.4 Model Fits

2.4.1 `Clustertools`

`Clustertools`[1] is a `python` module writted by Jeremy Webb that has many functions which make the analysis of star cluster properties very simple. Chief among these functions are those that can produce cluster profiles using the positions, velocities, and masses of the particles in the cluster. One important example of these profile functions is `clustertools.rho_prof`. This function takes either component of star cluster, and returns the density profile for that component. To do this, the code bins the star cluster into radial bins, the number of which is set by the user. A key requirement in the binning process is that every bin must contain an equal number of particles. To calculate the density in each bin, this function takes the sum of the masses of every particle in the bin, and divides by the volume calculated as

$$V = \frac{4\pi}{3}(r^3_{max} - r^3_{min}) \tag{2.27}$$

[1] https://github.com/webbjj/clustertools

where r_{max} and r_{min} are the top and bottom limits for a corresponding bin respectively. The function finally assigns the resulting density to the radial distance r corresponding to the average radial distance of each particle from the cluster centre (i.e $r = \frac{\sum_i r_i}{N}$ where N is the number of particles).

An important caveat to the requirement that each bin contains an equal number of particles is that, often times, the particles in our star clusters are not evenly distributed. This effect is especially visible at r values where stars are more diffuse, and the density falls off rapidly. The small densities at large r means the final bin in `clustertools.rho_prof` would span a wide radial distance in order to maintain a constant number of stars in each bin. Because we are representing each bin (which contains many stars) as a single density at a given radius, there must be some error associated with the final density of each bin.

The definition of variance is given by

$$\sigma^2 = \frac{\sum_i (x_i - \bar{x})^2}{n - 1} \tag{2.28}$$

where x_i is the parameter of interest of the ith particle, $\bar{x}$ is the average of that parameter, and n is the total number of particles in the given bin. In order to arrive at a density variance, we need to find the variance in our mass measurement M and our r measurement from each particle in a given bin. We do this by substituting $x = M$ and $x = r$ into equation 2.28 for the mass and radial variance calculations respectively.

Given the definition of density in each bin as the total mass divided by equation 2.27, we can relate the mass and radial variances to the density variance for the ith bin using

$$\sigma_{\rho,i} = \sqrt{(\frac{\delta\rho}{\delta M}\sigma_{M,i})^2 + (\frac{\delta\rho}{\delta r}\sigma_{r,i})^2} \tag{2.29}$$

which leads to

$$\sigma_{\rho,i} = \frac{3M_i}{4\pi r_i^3}\sqrt{\frac{\sigma_{m,i}^2}{M_i^2} + \frac{9\sigma_{r,i}^2}{r_i^2}} \tag{2.30}$$

With this, we can now calculate the density profile of a given set of particles with associated error on each measurement.

Using the density profiles calcualted by `Clustertools`, we are able to fit density models to our clusters. The three models we focus on are the EFF, Plummer (1911), and King (1966) models. We carry out our fits using the Levenberg-Marquardt (Levenberg 1944) method which minimizes the χ^2 defined as

$$\chi^2 = \sum_i \frac{(O_i - M_i)^2}{\sigma_i^2} \tag{2.31}$$

where O_i is the value of the density of the cluster calculated using `clustertools.rho_prof` in the ith bin, M_i is the value of the density calculated using either of the three models (EFF, Plummer, or King) in the ith bin, and σ_i is the density variance in the ith bin.

We now discuss the three models in more detail starting with the Plummer model.

2.4.2 Plummer Model

A Plummer 1911 model is a density distribution that has been used in numerous simulations to represent the initial conditions of star clusters. This model is in dynamical equilibrium and its derivation requires a potential energy function given by

$$\phi(\mathbf{r}) = \frac{-GM}{(r^2 + a^2)^{1/2}} \tag{2.32}$$

where G is Newton's gravitaional constant, M is the mass of the system, r is the distance away from the system centre, and a is a scale parameter. This helps define the clusters core. Furthermore, this model assumes spherical symmetry and we can therefore replace

r with r. To derive the density profile from the potential, we use the Poisson equation

$$\nabla^2\phi = -4\pi G\rho \tag{2.33}$$

which results in

$$\rho(r) = \frac{M}{4\pi}\frac{3a^2}{(r^2+a^2)^{1/2}} \tag{2.34}$$

It is helpful to look at equations 2.32 and 2.34 in terms of the central potential (ϕ_0) and central density (ρ_0)

$$\phi(r) = \phi_0(1+\frac{r^2}{a^2})^{1/2} \tag{2.35}$$

and

$$\rho(r) = \rho_0(1+\frac{r^2}{a^2})^{-5/2} \tag{2.36}$$

where $\phi_0 = -\frac{GM}{a}$ and $\rho_0 = \frac{3M}{4\pi a^3}$ which helps illustrate that as we get to infinitely small r, the potential is represented by that of a particle with mass M and radius a.

In order to set up a Plummer sphere in position and velocity space, one can look at the method outlined in Aarseth (1974) which is described as follows. First, we want to populate a Plummer sphere with N-body particles. For this derivation, we elect to use N-body units (Heggie and Mathieu 1986) which set $G = M = R = 1$ where M is the total mass of the system, and R is the *virial radius* of the system which is the radius within which $T = -\frac{1}{2}U$. We then integrate equation 2.34 to find an expression for the mass enclosed in a sphere of radius r

$$M(r) = r^3(1+r^2)^{-3/2} \tag{2.37}$$

The next step is to generate a random number X and set $M(r) = X$. This allows us to solve for r and ensure that the resulting position follows the density profile outlined by

equation 2.34. Rearranging equation 2.37 leads us to

$$r = (X^{-2/3} - 1)^{-1/2} \tag{2.38}$$

With this, we can randomly populate the sphere of radius r with Cartesian coordinates (x, y, z) using two more randomly selected numbers Y and Z in the following way:

$$z = (1 - 2Y)r \tag{2.39}$$

$$x = (r^2 - z^2)^{1/2} cos(2\pi Z) \tag{2.40}$$

$$y = (r^2 - z^2)^{1/2} sin(2\pi Z) \tag{2.41}$$

which allows for an isotropic sampling of positions.

The Plummer sphere model is such that the entire system is in a steady state, and the velocities of each star are isotropically distributed. Sampling velocities for our newly initiated stars relies on the escape velocity of the system. The escape velocity of our cluster can be calculated using equation 2.32 and the kinetic energy of the system. Because equation 2.32 is the potential per unit mass, we can find the escape velocity v_e through

$$\frac{1}{2} m v_e^2 + m\phi(r) = 0$$

$$v_e = \sqrt{-2\phi(r)} = 2^{1/3}(1 + r^2)^{-1/4} \tag{2.42}$$

where v_e is the escape velocity. We can then use the magnitude of the velocity V to find each component such that $V = qv_e$ where q is between 0 and 1. To ensure that the resulting velocities are isotropic, we find the velocity components (u, v, w) using 2

new random numbers Y_v and Z_v in the same way as equations 2.39, 2.40, and 2.41 but setting r as V.

Both components (stars and gas) of each of our star clusters are set up using Plummer spheres as shown in figure 2.1. We choose the scale radius such that the half mass density of each component is in the range given by Portegies Zwart et al. (2010) ($10^{2-4}\mathrm{M}_{\odot}\mathrm{pc}^3$). The masses of each of the stars are sampled randomly from a Kroupa (2001) IMF which is similar to that introduced in Chabrier (2005). In this figure, the stellar component shows slight deviations around the idealized Plummer density profile due to the fact that we have a limited number of stars in each cluster. As we get to a smoother distribution (gas) the density profile matches much closer to that of an idealized Plummer sphere.

2.4.3 King (1966) Model

Observations presented by von Hoerner (1957) and King (1962) showed that local Milky Way star clusters do not extend to infinity, but rather, are cut off from tidal forces by the Milky Way. The extent of a given star cluster can then be described using the *tidal radius*. The tidal radius is the distance away from the cluster centre where gravitational interactions from the surrounding galaxy overpower those from the star cluster, and a lone star can be stripped from the cluster (von Hoerner 1957). Therefore, in the King (1966) model, no stars that exist beyond the tidal radius are a part of the star cluster and the density profile does not extend to infinity like the Plummer model described above. To account for this in the radial density distribution, one needs to prevent the distribution of particles whose total energy is > 0, in other words, particles who are removed by tidal forces from the parent galaxy. The velocity distribution function is Maxwellian that is truncated at the escape velocity v_e of the cluster, thus ensuring no stars are initiated with $v > v_e$.

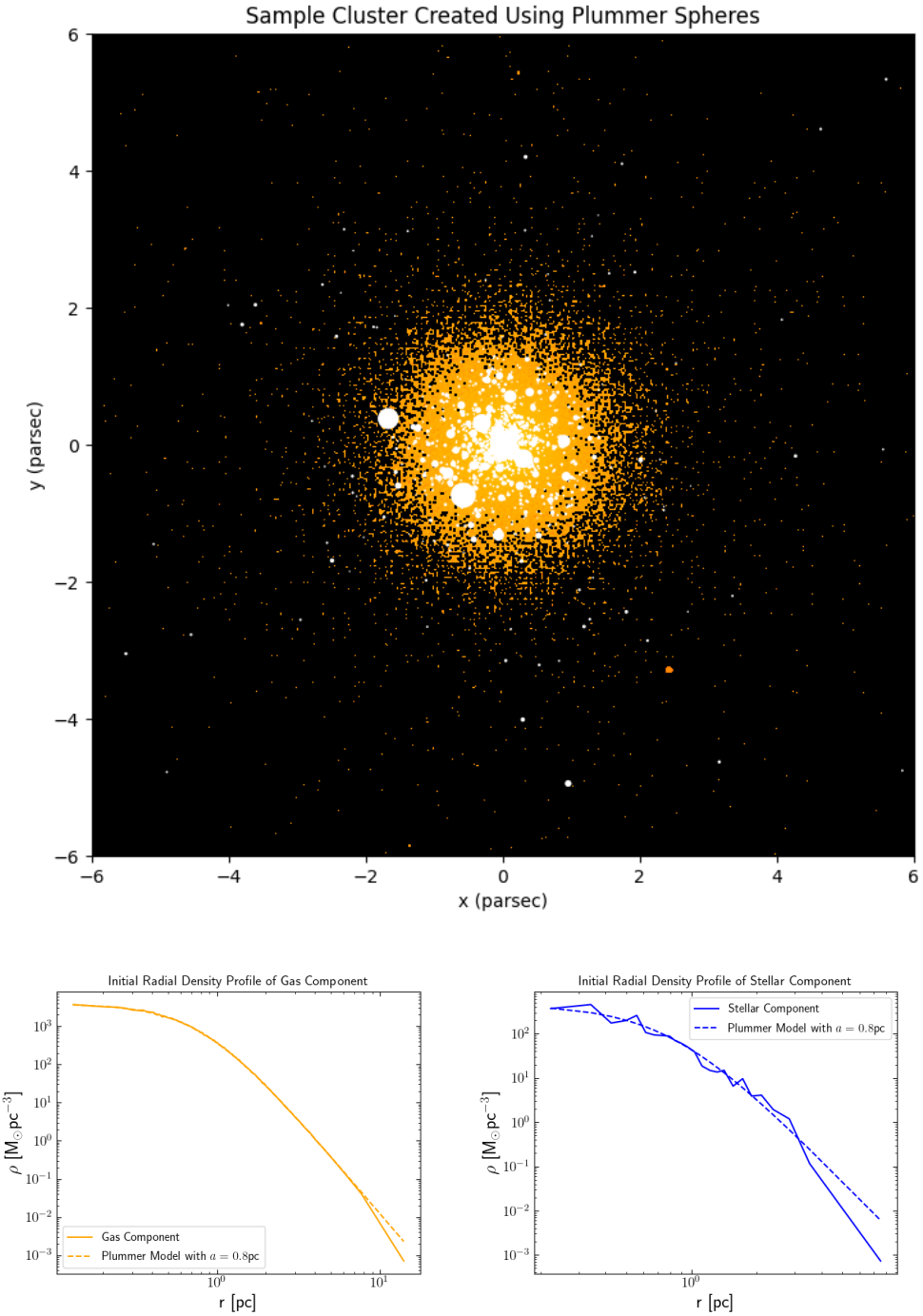

FIGURE 2.1: A sample star cluster created using Plummer spheres for the stars (white circles) and gas (orange). The size of the white circles is scaled by the stellar mass which is applied using a Kroupa IMF.

To find the density ρ as a function of position r, one must solve the Poisson equation:

$$\frac{d^2V}{dr^2} + \frac{2}{r}\frac{dV}{dr} = 4\pi G\rho \tag{2.43}$$

where V is the potential of the cluster. However, this is often rewritten in terms of $W = -2j^2V$ (where j is the reciprocal of the standard deviation of the Gaussian distribution that represents the energy distribution function and V is the potential) and $R = \frac{r}{r_c}$ where $r_c \approx$ the core radius of the cluster. This takes the form

$$\frac{d^2W}{dR^2} + \frac{2}{R}\frac{dW}{dR} = -9\frac{\rho}{\rho_0} \tag{2.44}$$

The King (1966) models are therefore dependant on two parameters: W_0 which is a unitless constant that quantifies the degree of central concentration of the cluster, and r_c the core radius which can also be converted to the tidal radius using the parameter $c = \log_{10}(r_t/r_c)$ when a tidal force from a surrounding galaxy acts on the cluster. The first step in this calculation process is to calculate the quantity

$$\psi = e^W \int_0^W e^\eta \eta^{3/2} d\eta$$

$$= \frac{3}{4}\sqrt{\pi}[e^W Ef(\sqrt{W}) - \frac{2}{\sqrt{\pi}}\sqrt{W}(\frac{2}{3}W + 1)] \tag{2.45}$$

where Ef is the error function. This is proportional to the density as a function of W, $\rho(W)$. One can then substitute $\rho(W)$ into equation 2.44 to solve for the density as a function of position r. To carry out this numerical integration, we use the `python` module `galpy`[2] (Bovy 2015).

The tidally truncated nature of King models lend themselves to fit well to older more

[2] https://github.com/jobovy/galpy

dynamically evolved globular clusters (Grudić et al. 2018, Zocchi et al. 2012). The King profile is also commonly used as initial conditions for stellar positions in a similar way to the Plummer profile (Mackey and Gilmore 2003a, Whitehead et al. 2013).

2.4.4 Elson, Fall, and Freeman (EFF 1981) Model

Surface brightness profiles are not well described by truncated King models, rather, the gentle curves in their tails are better represented by the profile introduced by Elson et al. (1987) hereafter EFF (Portegies Zwart et al. 2010):

$$\Sigma(r) = \Sigma_0(1 + \frac{r^2}{a^2})^{-\gamma/2} \tag{2.46}$$

or, the volume density profile:

$$\rho(r) = \rho_0(1 + \frac{r^2}{a^2})^{-\frac{\gamma+1}{2}} \tag{2.47}$$

Here, a is a scale radius that differentiates the core of the distribution from the tail. Equation 2.47 is very similar to equation 2.34. The main difference comes from the ability of the EFF to have a varying slope in the tail end of the density profile. The profile was introduced as a way to fit observations of young star clusters in the Large Megellanic Cloud (LMC) and the authors find that γ values between 2.2 and 3.2 provide the best fit to their observations.

An example of an EFF fit to a cluster's stellar density distribution can be seen in figure 2.2 which is a resolved image of the cluster Westerlund 2 which has been identified as consisting of two subclusters on route to merging in the near future (Zeidler et al. 2021). Highlighted in this image are the best fit core radius r_c of each subcluster, the half mass radius r_{hm} of each subcluster, and the scale radius a of each subcluster. While

a theoretical definition of this radius was introduced in King (1966) as

$$r_c = \sqrt{\frac{3\sigma_v^2}{4\pi G \rho_0}} \tag{2.48}$$

where σ_v is the cluster velocity dispersion, and ρ_0 is the central density of the cluster, in situations where the velocity dispersion or central density of a system are not well constrained, the EFF model can provide an analytic solution to r_c (provided that equation 2.47 fits the data of the cluster well) using

$$r_c = a(2^{2/\gamma} - 1)^{1/2} \tag{2.49}$$

2.5 Merger Simulation Methods

In the following sections, we summarize the numerical methods being used in our simulations, outline the process by which we initialize our isolated clusters, starting from initial particle distributions, and the conditions used to determine when both are ready to be set on their collision course. We then outline the initial setup of our merger and the parameters of interest when choosing which mergers to include from the H18 simulations.

2.5.1 Isolated Clusters

We set up initial conditions for our individual clusters using parameters taken from the H18 sink particles, specifically, the mass in stars (M_*) and the total mass in stars and gas (M_{tot}). The initial distributions of our N-body and SPH particles follow a Plummer (Plummer 1911) sphere with a scale radius chosen such that the half mass density of the cluster starts as $\rho_{hm} = 10^3 M_\odot/pc^3$. This density choice is consistent with observed YMC densities (Portegies Zwart et al. 2010). Given a ρ_{hm}, and the total mass of the cluster, we can calculate the half mass radius r_{hm} which we convert to a Plummer scale

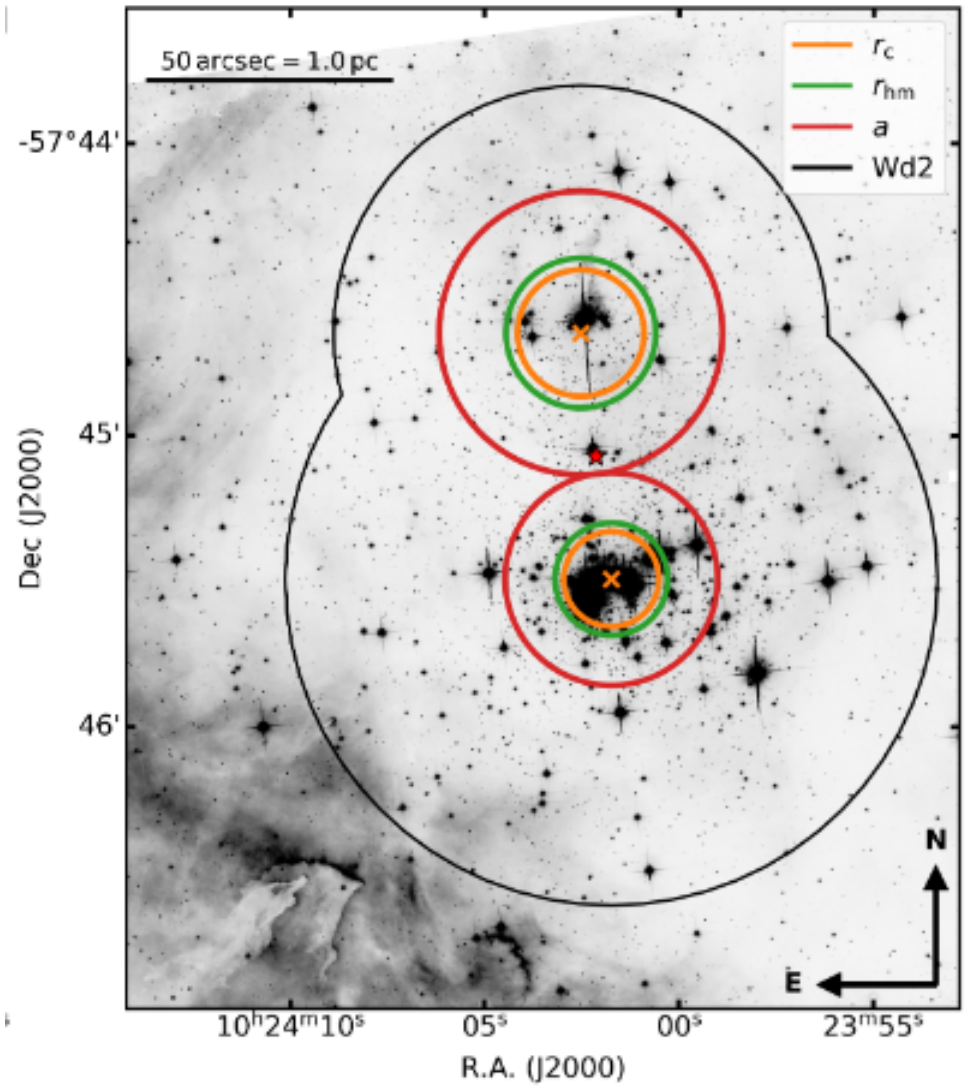

FIGURE 2.2: Image of Wd2 taken by HST F814W (Zeidler et al. 2021). ©AAS Reproduced with permission.

radius using $a \approx 1.3 r_{hm}$. This way, the scale radius a is dependant on ρ_{hm} (which we choose as a constant) and the total mass of the cluster allowing for more massive clusters to have larger initial a values. This allows us to simulate a wider range of cluster masses without running into extremely small timesteps by virtue of high central densities (see equation 1.3). However, our process outlined above allows our clusters to vary in size: through imposing a half mass density, the size of a depends on the total mass of the cluster. Our initial scale radii for our clusters is such that there is either stars or gas located beyond the H18 sink particle accretion radius or $r_{sink} \approx 1.7$pc for all of our simulations. In order to relate our results to the H18 sink particles, we focus on the `change` imposed on the resultant cluster by the merger through comparing it with the clusters before they have merged (see section 3.2).

The number of SPH particles in our simulations is given by $N = M_g/m_{SPH}$ where M_g is the total mass in gas of the sink particle taken directly from H18, and $m_{SPH} = 0.06 M_\odot$. A lower m_{SPH} brings the resolution to a point where our run times get too high. Furthermore, our choice of m_{SPH} leads to a smoothing length $h \approx 0.01$pc which is significantly smaller than the core radii in our clusters implying sufficient spatial resolution of our smallest scales in our simulations. Stellar masses are sampled from a Kroupa (Kroupa 2001) IMF between $0.15 M_\odot$ and $100 M_\odot$. The gas temperature is chosen to be $10K$, consistent with GMC temperatures from H18. We assign each particle a velocity which we sample using the method outlined in Aarseth (1974) and in section 2.4.2. We calculate the velocity dispersion of our stellar and gas component separately and scale the velocities of each such that both are initially in virial equilibrium ($2K_{s,g}/|P_{s,g}| = \alpha_{s,g} = 1$).

Next, we allow our cluster to evolve in its own isolated simulation box. We do this so that the stars can have time to react to the new potential introduced by the gas, and vice versa in a process called *numerical relaxation*. In order to decide when our clusters are done numerically relaxing, we look at the evolution of the core radii for the stars

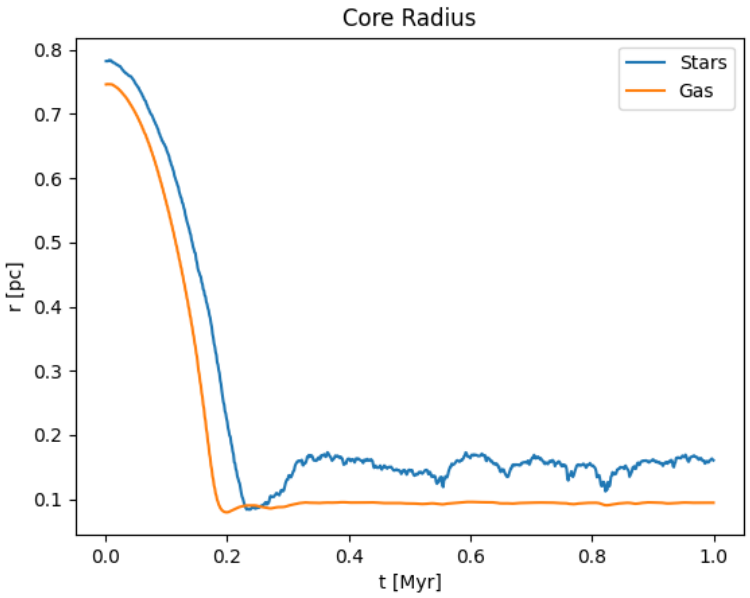

FIGURE 2.3: Evolution of the core radius for an isolated cluster

and gas as a function of time, as shown in figure 2.3 for an example cluster. Up until 0.21Myr, the core radii are decreasing drastically until both become stable. This effect comes from both stellar and gas components reacting to the potential of the other. In this example, to ensure stability, we take the snapshots of this cluster after $t = 0.21$Myr as our initial conditions for our merger simulation. This corresponds to roughly 0.01 N-body times. Because we set up all of our clusters with the same initial half mass density, every cluster in our suite of simulations shares the same conversion between N-body and physical times initially. The crossing timescale is defined as $t = r_{vir}/v$ where r_{vir} is normalized to 1 in N-body units (Heggie and Mathieu 1986) and v is the velocity of a star. Assuming virial equilibrium, as N-body units do, we can find that the velocity in the above equation $v \propto \sqrt{r_{hm}^3/M_{hm}} \propto \rho_{hm}^{-1/2}$ which means, regardless of our cluster mass, 1 N-body dynamical time is always the same physical time for every simulation of our isolated cluster systems initially but can change as the system evolves. Furthermore, every cluster's core radius will numerically relax in the same timeframe as the example

above (within ≈ 0.01 N-body times). Note, although the decrease in the core radius can cause a deviation of ρ_{hm} away from $10^3 M_\odot pc^{-3}$, the value of ρ_{hm} never exceeds the upper limit shown in Portegies Zwart et al. (2010). It stays within the quoted range of $10^2 M_\odot pc^{-3} < \rho_{hm} < 10^4 M_\odot pc^{-3}$.

As our isolated clusters relax, we find some movement off from the centre for both the stellar and gas components. We move both components to the centre of the simulation box and subtract the total centre of mass velocity before the relaxed clusters are set to merge with one another.

2.5.2 Merger Setup: The Creation of the Resultant Cluster

H18 ran two GMC simulations: one at one solar metallicity ($1Z_\odot$) and the other at $0.1Z_\odot$. We take our mergers from the $1Z_\odot$ simulation. Each sink pair we take was separated by a distance d before they merged with one another in H18 and, throughout the GMC evolution, eventually merged. Many, but not all, of the mergers contained sink particles that have undergone previous mergers. For these, H18 constructed a merger tree wherein a given sink particles merger history can be recorded as seen in figure 1.5. This involves taking careful note of the time between a sink particle's first merger and its second and third and so on. For our simulations, we want to keep our simulation time below the first expected supernovae explosions as this is the time when most to all of the gas mass has been removed from a star cluster (e.g Pelupessy and Portegies Zwart 2012). Furthermore, our stellar mass range lies within that expected to go supernova in $\approx$ 3Myr (e.g Meynet and Maeder 2003). Therefore, we run all our simulations for 3Myr after the clusters have been initiated in the merger simulation box. We further restrict our sampling of H18 sink mergers by only including those that have never undergone a merger previous to the one we simulate. We refer to these as *first contact* mergers. Through simulating these mergers, we are able to provide constraints

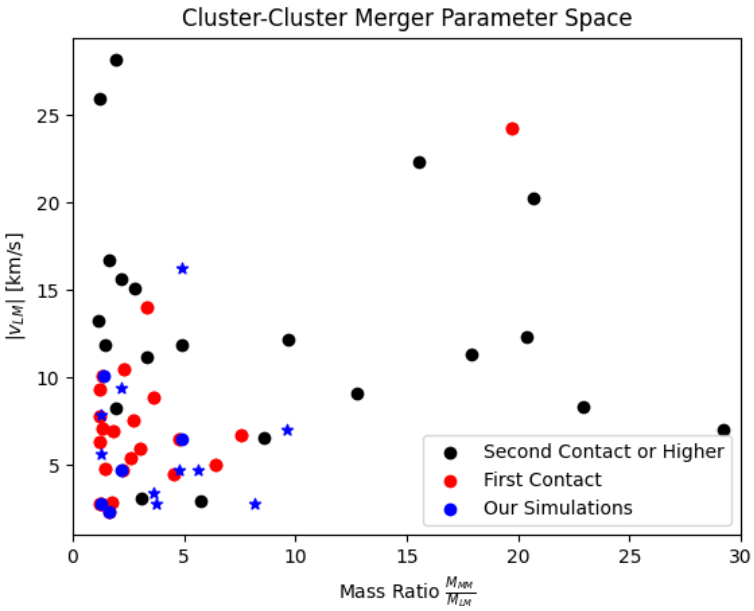

FIGURE 2.4: The parameter space from which our collisions are being sampled. Black points represent second contact mergers or higher. Red points represent first contact mergers i.e. mergers where both members in the cluster pair have not undergone any previous mergers. Blue points represent the mergers we model for our simulations.

on what the distribution of stars and gas for a second contact merger should look like, allowing us to simulate many more H18 sink mergers in the future.

We select merger pairs from the H18 simulation based on the mass ratio of the pair ($f_M = \frac{M_{MM}}{M_{LM}}$ where M_{MM} and M_{LM} are the sum of the stellar and gas masses for more massive and less massive cluster respectively) and the velocity of the colliding cluster (v_{LM}). A plot of the mergers in this parameter space from the H18 simulation can be seen in figure 2.4. For this plot, we have limited the mass ratio range to be from 0 to 30. This cuts out only 2 mergers that have mass ratios of ≈ 100 and ≈ 400.

We simulate 5 of these first contact mergers (labelled run 1-5, shown in blue as circles, see table 2.1), giving us 10 isolated clusters in total. These 10 clusters provide us with a significant range in cluster masses while not containing clusters that are too large thus

Run number	$M_{MM,s}[10^4 M_\odot]$	$M_{MM,g}[10^4 M_\odot]$	$M_{LM,s}[10^4 M_\odot]$	$M_{LM,g}[10^4 M_\odot]$	$d[pc]$	$v_{LM}[kms^{-1}]$
1	0.3	2.1	0.2	1.2	2.7	2.3
2	0.05	0.3	0.02	0.2	2.4	2.8
3	0.1	0.8	0.06	0.4	4.9	4.7
4	0.4	1.6	0.1	0.3	2.9	6.5
5	0.4	0.5	0.3	0.3	3.3	10
2to3	0.1	0.8	0.02	0.2	2.4	2.8
2to5	0.4	0.5	0.02	0.2	2.4	3.4
3to1	0.3	2.1	0.06	0.4	4.9	4.7
3to4	0.4	1.6	0.06	0.4	4.9	4.7
2_2v	0.06	0.3	0.02	0.2	2.4	5.6
2to1	0.3	2.1	0.02	0.2	2.4	2.8
2to4	0.4	1.6	0.02	0.2	2.4	7.0
2_2p8v	0.06	0.3	0.02	0.2	2.4	7.8
3_2v	0.1	0.8	0.06	0.4	4.9	9.4
4_2p5v	0.4	1.6	0.1	0.3	2.9	16

TABLE 2.1: Parameters for our merger simulations. Column 1: the name of the run, column 2: the mass of the more massive cluster in stars, column 3: mass of the more massive cluster in gas, column 4: mass of the less massive cluster in stars, column 5: mass of the less massive cluster in gas, column 6: the initial separation along the x-axis of the two clusters, column 7: the x-velocity kick given to the less massive cluster towards the origin. The horizontal line splits the models taken directly from H18 sinks (upper) and those given some alteration (lower). Runs are ordered by increasing collisional velocity.

keeping simulation times reasonable. This spread in cluster mass can be translated to a spread in collision mass ratio f_M.

Along with the H18 mergers, we simulate mergers that were not present in H18 (called other models, shown in blue as stars). To do this, we use a cluster from one H18 merger and collide it with a cluster from another H18 merger (for example, we take the less massive cluster from the run1 pair and simulate its merger with the more massive cluster from the run3 pair in table 2.1 and the run is labelled run3to1) allowing us to better sample the parameter space from figure 2.4. The last alteration we make to the H18 model runs in table 2.1 is increasing or decreasing the collision velocity v_{LM} while keeping all other parameters the same. These runs are labelled as run$x$_yv where x is the label of the H18 model run we are updating, and y is the factor by which we multiply v_{LM} for that run. The yellow points include both of these alterations. All of our merger simulations are done head on.

Once each cluster has reached the relaxation point outlined in section 2.5.1, we take the newly relaxed system of stars and gas and initialize them together in a new simulation box as follows:

- The more massive cluster is placed at position $(x, y, z) = (0, 0, 0)$ with no velocity
- The less massive is placed a distance $x = d$, away from more massive cluster and is given a velocity v_{LM} in the x-direction towards the origin.

Chapter 3

Results

3.1 Resultant Cluster Properties

We begin with a discussion of a typical merger from our sample (run 3 in table 2.1). The total masses of the more and less massive clusters in the merger are 0.9 and 0.5 $\cdot 10^4 M_\odot$ respectively resulting in a mass ratio of $f_m = 2$ which, coupled with a collisional velocity of $v_{LM} = 4.7 \text{kms}^{-1}$ places this merger in the region of parameter space where we find most of the first contact mergers from H18 as seen in figure 2.4. Most of the total mass of both clusters resides within $r_{sink} \approx 1.7$pc (80 per cent of the more massive cluster mass, 90 per cent of the less massive cluster's mass). Snapshots of this merger can be seen in figure 3.1.

The white circles shown in figure 3.1 represent the stars belonging to the less massive cluster, and the blue circles represent those belonging to the more massive cluster. The size of each circle scales with the mass of the star it represents. The orange points show the gas in the simulation. At the beginning of the simulation, the kick given to the less massive cluster causes it to travel towards the stationary more massive cluster. After $t \approx 0.7$Myr, the clusters collide with one another as can be seen by the merging of the gas components of each cluster. We denote this time as the collision time t_{col} which

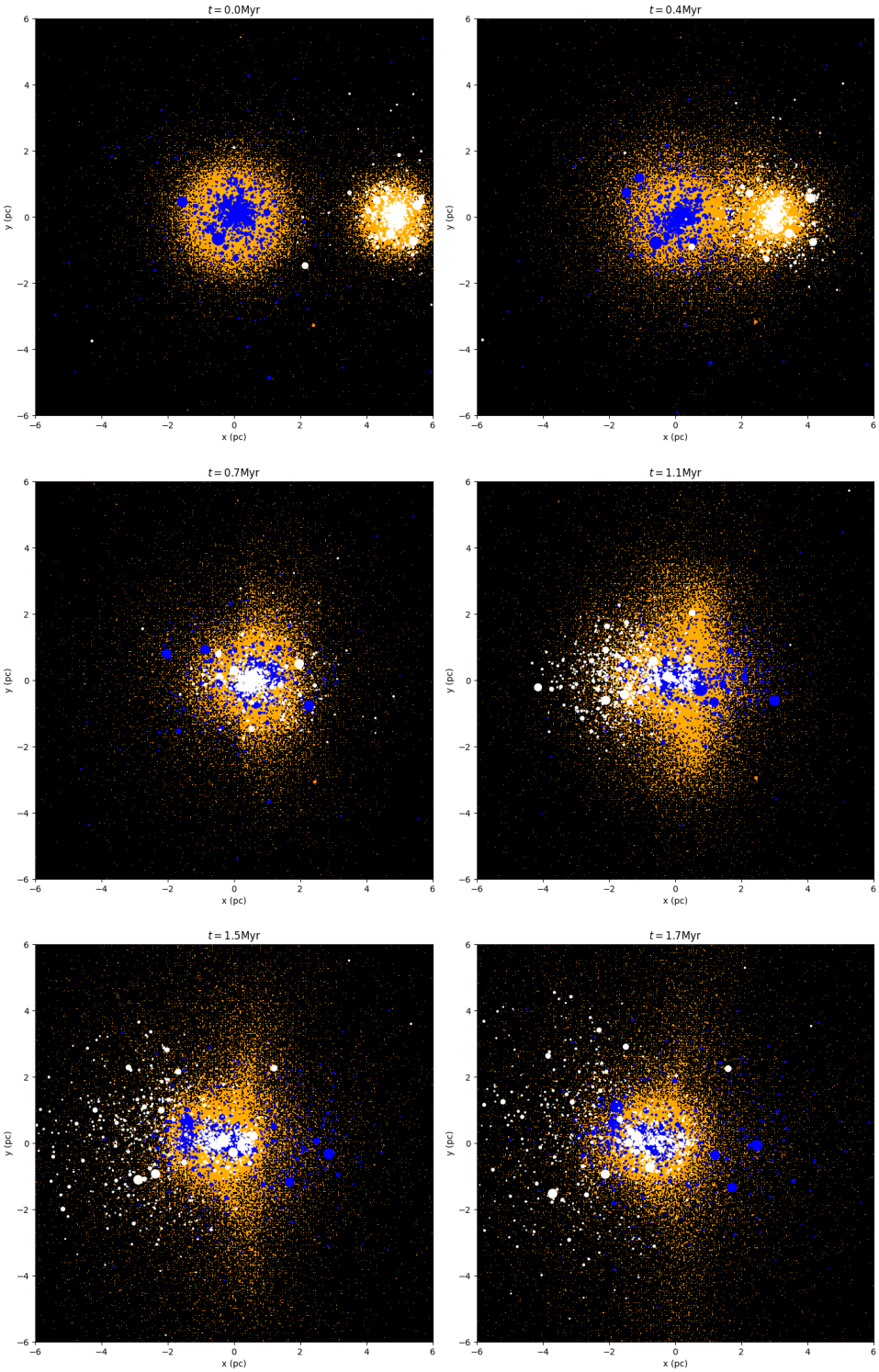

FIGURE 3.1: Snapshots of the stars and gas from merger run 3 leading up to the monolithic time. The circles represent the stars from each cluster (blue belong to less massive cluster, white belong to more massive cluster). Size of the filled circles scales with mass of the star. Time is take with respect to the beginning of the simulation. The left panel on the second row shows the merger at $t = 0.7\text{Myr} = t_{col}$ and the right panel on the second row shows the merger at $t = 1.1\text{Myr} = t_{mon}$.

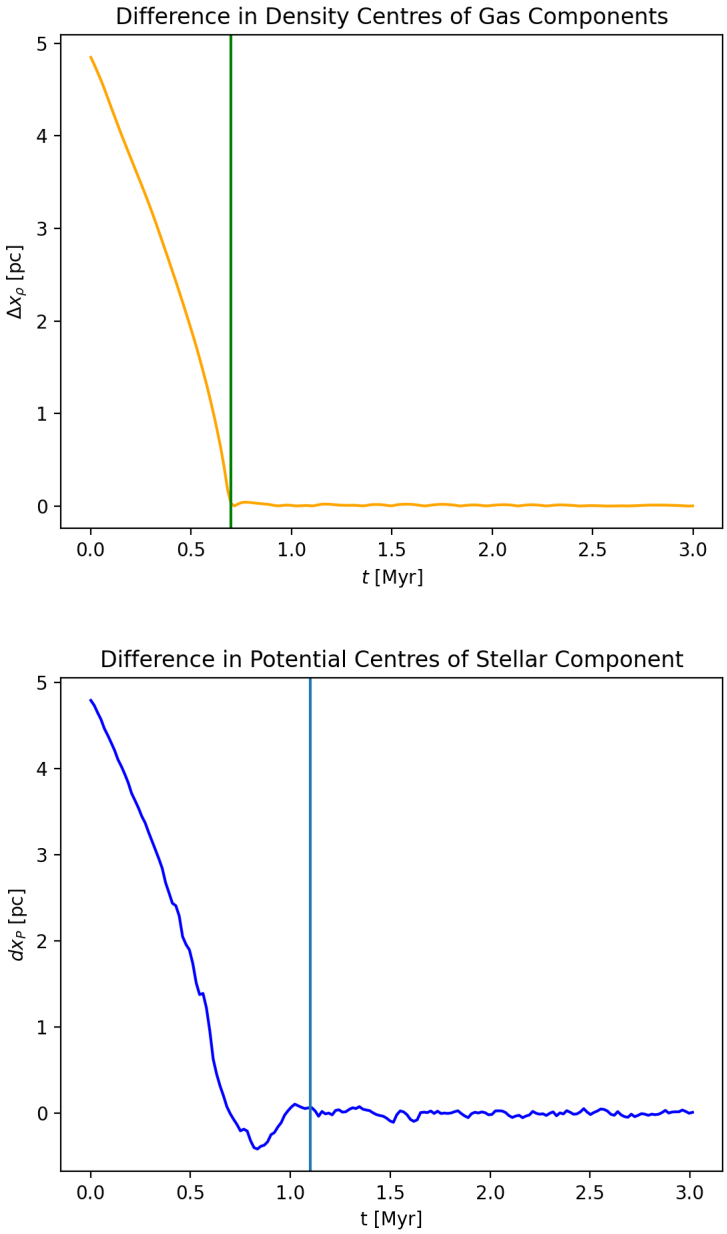

FIGURE 3.2: Definition of the collision time t_{col} (top) and the monolithic time t_{mon} (bottom). These definitions rely on the gas and stellar components separately. t_{col} is determined using the separation of the gas density centres dx_ρ and t_{mon} is determined using the separation of the stellar centres dx_p.

is defined as the time at which the densest point of both gas clouds (density centre) overlap for the first time along the x axis shown in the top panel in figure 3.2. This overlap occurs when the separation of the density centres reaches a minimum. While stars originally belonging to the more massive cluster lie roughly overlapped with the newly merged gas cloud at the time of the collision, stellar members of the less massive cluster accelerate through the merged gas cloud, leading to an increase in the separation of each cluster's stellar component centre of mass. Stars that once belonged to the less massive cluster disperse in the outermost region. The core of the less massive cluster combines with that of the more massive cluster roughly 0.4Myr after the collision, and a single monolithic cluster is formed. We call the time at which the monolithic cluster is formed, the monolithic time and denote it using t_{mon}. An example of our definition of t_{mon} can be seen in the bottom panel of figure 3.2.

To determine t_{mon}, we take an average over the x positions of the n stars that feel the least total potential in both the more and less massive clusters (we call the average of these positions $x_{p,MM}$ and $x_{p,LM}$ for the more and less massive clusters respectively), and look for the time at which x_p of each cluster overlaps as seen in figure 3.2 by calculating dx_p. To find the positions, we choose to average over the 5 per cent of stars with the lowest potential in each cluster. This corresponds to the number of stars located within 1 core radius of each cluster centre before the merger. Therefore, our definition of monolithicity is dependant on the behaviour of the core of each star cluster.

To find the overlap, we begin by averaging dx_p values of each cluster in 0.1Myr time bins. This time scale helps us smooth out noise in the motion of $x_{p,LM}$ after the less massive cluster merges with the more massive one. We then look for the time at which the difference goes below a threshold equivalent to the core radius of the more massive cluster before the merger process. This value is 0.08pc for this merger simulation. Therefore, our definition of monolithicity ensures that the core radii of each cluster remain overlapped.

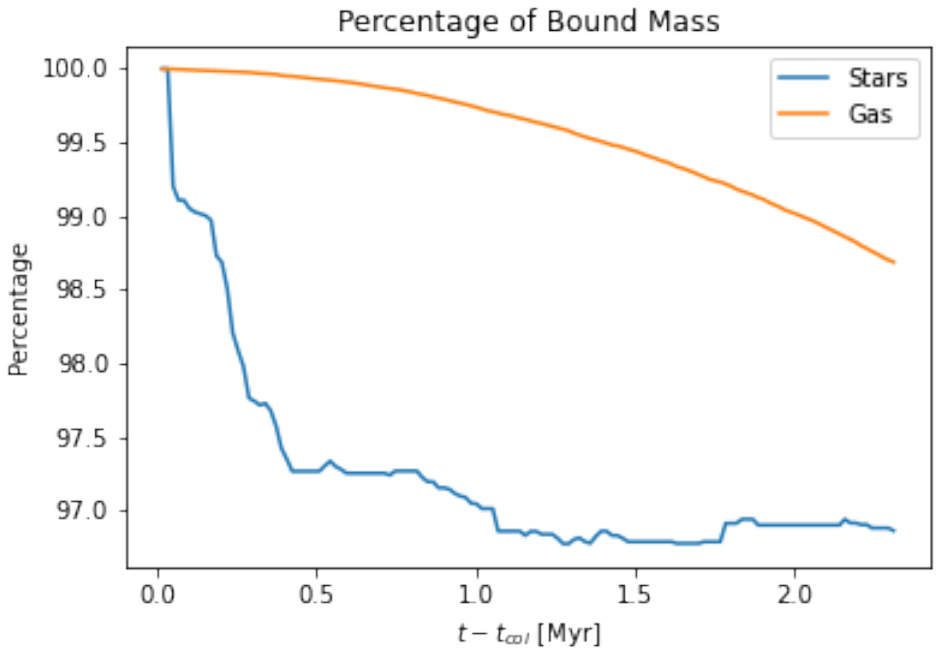

FIGURE 3.3: Bound mass fractions of resultant cluster after merger.

The horizontal line in figure 3.2 indicates the time at which the star cluster cores overlap which happens at $t - t_{col} \approx 0.4$Myr for run3.

3.1.1 Bound Fraction

A constraint of the sink particle prescription used in H18 is that all mass inside each sink remains in the sink throughout the entire simulation. When two parent sink particles merge, the resultant sink's mass will simply be the sum of the masses of each parent. We can test this approximation by looking at the bound percentage of stellar and gas mass in the resultant cluster after the merger takes place. This can be seen in figure 3.3 for run3. We calculate the kinetic energy of each star and gas particle in the simulation and compare it to the potential energy felt on that particle by every other particle in the simulation (stars and gas) and consider a particle bound when its $T + U < 0$ where T is its kinetic energy, and U is its potential. We see that by the end of our simulations, ≈ 3 per cent of stellar mass and ≈ 1 per cent of gas mass has become unbound. Most of

the decrease in bound stellar mass happens immediately after t_{col} as stars that initially belonged to the less massive cluster have been flung out of the gravitational pull of the resultant cluster. This is in contrast to the sink particle prescription. These results are somewhat consistent with simulations done by Banerjee and Kroupa (2015) which quote a negligible amount of unbound stellar mass through merger simulations with an included gas potential. As well, N-body simulations done by Grudić et al. (2018) show that $\lessapprox$ 10 per cent of their stellar mass becomes unbound after the merger of two equal mass Plummer spheres. Therefore, when using sinks to model this subcluster merger, the resultant sink particle's mass is accurate to 95 per cent.

Not all of the resultant sink particles in H18 last for 3Myr after the initial merger has taken place (see section 2.5.2). Though a number of sink particles do not undergo more than one merger in H18, the average time between a first generation resultant sink particle's formation and its second merger in the H18 simulation is $\approx$ 0.4Myr. With this in mind, we can look at figure 3.3 to see how well the sink particle prescription models initial mergers in terms of mass conservation. In this simulation, 0.4Myr after t_{col} we see that the total unbound stellar mass percentage is $\approx$ 5.5 per cent and the unbound gas mass percentage is only $\approx$ 0.3 per cent showing an acceptable conservation of total mass for this simulation. We therefore conclude that in order for this particular sink particle merger to better represent a subcluster merger in the H18 simulation, the resultant sink particle's stellar mass should decrease by $\approx$ 5.5 per cent, and the gas mass should decrease by $\approx$ 0.3 per cent though, as we will see in later sections, these values are tied to the collision al velocities of our simulations and can increase drastically.

3.1.2 Cluster Size

We can now look at the inner, and outer regions of the resultant cluster to better understand where in the cluster is the remaining bound mass most affected. We are looking to see which regions of the cluster experience the most growth due to the merger

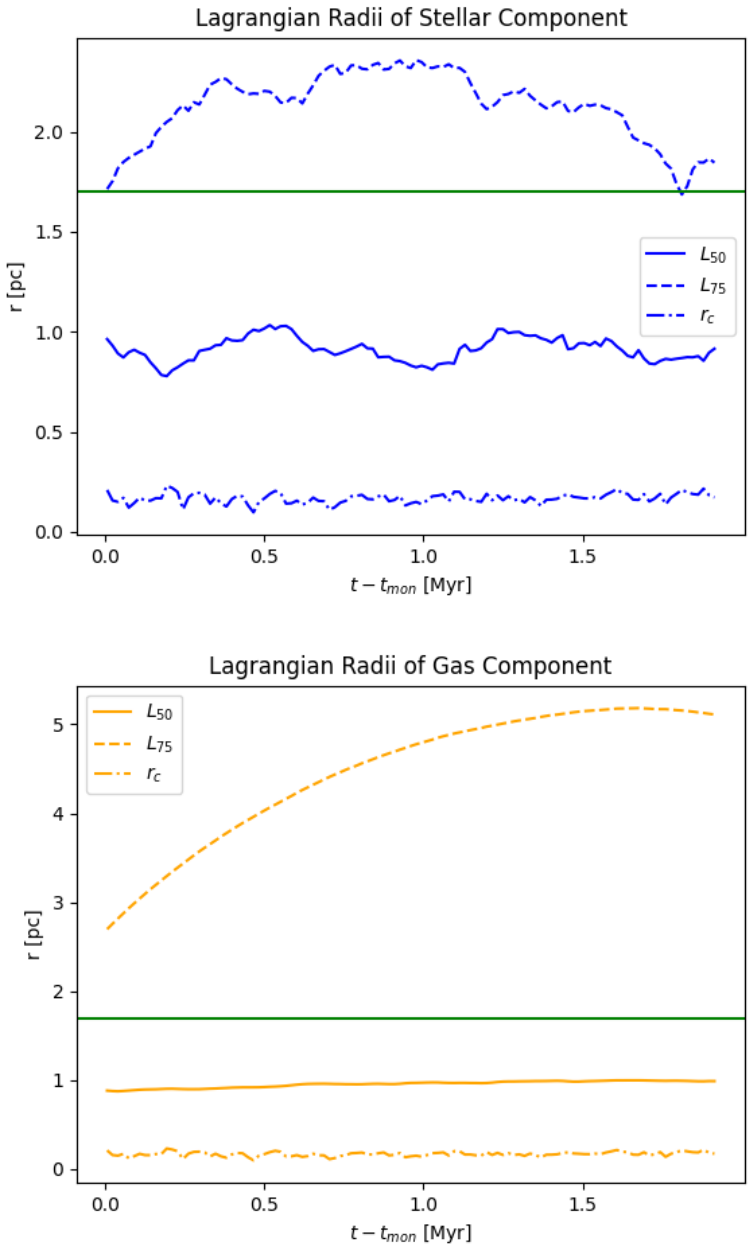

FIGURE 3.4: Core radii, half mass radii and 75 per cent mass radii of stellar (left) and gas (right) component for the resultant cluster after the merger. The green line indicates the sink radius prescribed in the H18 simulations ($r_{sink} \approx 1.7$pc).

process. Furthermore, we can see where in the cluster, this growth results in material being pushed beyond the sink radius. This implies that the sink particle accretion radius in H18 simulations does not necessarily hold 100 per cent of the remaining mass of the cluster after a merger between two sinks has occurred.

Note, the parent clusters that make up the monolithic cluster in run 3 were initialized with most of their total mass (80 per cent and 90 per cent for the more and less massive cluster respectively) within r_{sink}. In runs where this does not hold, and a significant amount of material is initialized beyond r_{sink}, we analyze the fractional growth of the Lagrangian Radii of a given resultant cluster compared to the parent clusters that make it up such that every simulation can be compared equally (see section 3.2). We look at the core, half mass, and 75 per cent mass radius of the resultant cluster (hereafter, when we refer to the resultant cluster, we refer to the bound members of each component only because these would be the members that remain part of the resultant sink particle) after t_{mon} once the cluster has become monolithic which can be seen for both the stellar and gas components in figure 3.4.

The core radius remains stable for the entire simulations after t_{mon} at $r_c \approx 0.2$pc and $r_c \approx 0.1$pc for the stellar and gas components respectively. The core radius of the resultant cluster has grown compared to the original clusters.

Immediately after t_{mon}, the stellar half mass radius $L_{50,s}$ has reached a stable state at a value of 0.9pc which is larger than $L_{50,s}$ of the initial clusters before the merger. Similarly, the gas half mass radius $L_{50,g}$ increases slowly for the entire simulation after t_{mon} and by the end of the simulation, $L_{50,g} \approx 1.1$pc which is also an increase compared to the original clusters before the merger. Though $L_{50,s}$ and $L_{50,g}$ both grow after the collision, neither grow beyond r_{sink} as shown by the green line in figure 3.4 implying that at least 50 per cent of each component of the resultant cluster remains inside the sink particle radius after the merger.

However, if we look at the L_{75} of each component, we see that, at most times after t_{mon}, both components' L_{75} is greater than r_{sink}. As seen in figure 3.4, the stellar component 75 per cent mass radius $L_{75,s}$ increases and oscillates around $\approx$ 1.9pc shortly after t_{mon}. $L_{75,g}$ increases steadily after t_{mon} and does not stop by the end of our simulation. If we look at $L_{75,g}$ at $t = t_{mon}$ and at the end of our simulation, we see that $L_{75,g} \approx$ 2.9pc and 5.4pc respectively. Because these values have moved beyond the sink radius, at least 25 per cent of the stellar and gas mass lies outside the sink radius. Therefore, we see that the resultant sink particle's accretion radius needs to increase in order to keep the remaining bound mass inside the sink.

Though our clusters do not have an accretion radius like sink particles do, we can still look at a cluster analogue to the sink particle accretion radius by looking at the 90 per cent mass radius of the resultant cluster $L_{90,RC}$. This is an analogue to a sink particles accretion radius r_{sink} which contains 100 per cent of a cluster's total mass. We, however, cannot use the 100 per cent mass radius because it is subject to the motions of 1 single N-body or SPH particle leading to too much noise. As well, because r_{sink} contains the entirety of the cluster's mass, we do not look at L_{90} for both components separately as we did above. In this analysis $L_{90,RC}$ is the 90 per cent mass radius of the entire resultant cluster (stellar plus gas component). We show $L_{90,RC}$ normalized by the L_{90} of the entire more massive ($L_{90,MM}$) and less massive ($L_{90,LM}$) parent clusters before the merger in figure 3.5. Directly after t_{mon}, the $L_{90,RC}$ increases and shows no sign of slowing down by the end of our simulation showing us that the outer most regions of the cluster are growing rapidly after the merger. This is partially due to the expansion of the gas component after the collision but, as we will see in later sections, the stellar component of our clusters are also expanding after the merger.

With the resolution in H18 of $r_{sink} = 1.7$pc, this resultant sink particle may be missing the chance to accrete extra gas mass before it merges with other sink particles.

This is due to the sink particle prescription allowing gas accretion to take place if gas is within one r_{sink} and gravitationally bound to the cluster. In this simulation, because the resultant cluster grows compared to the parents that make up the merger, a sink particle prescription which does not allow this growth will potentially be accreting less gas than it should be before it merges with another sink particle. This tells us that, at the resolution provided in H18, this star cluster merger cannot be simulated using sink particles because it may be missing accreted gas mass which may result in a discrepancy regarding the final mass of the YMC formed at the end of the H18 simulations. The magnitude of this discrepancy is dependant on how prompt the secondary merger process is. If the resultant cluster merges with another cluster quickly after it is formed, its $L_{90,RC}$ will not have had enough time to significantly grow, meaning that only a small fraction of extra gas would be added to the resultant sink. However, the longer it takes for a resultant cluster to undergo another merger, the larger $L_{90,RC}$ grows and the more mass it may accrete.

3.1.3 Density Profiles

We now turn our attention to the density profiles of the resultant cluster. In this analysis we treat the stars and gas of the resultant cluster separately and include only bound members of each component. Unbound stars and gas are no longer considered a part of the host cluster and therefore do not contribute to the density profiles.

Our analysis consists of fitting commonly used density profiles to the bound stellar and gas components of the resultant cluster. We fit the Plummer, Elson et al. (1987) (EFF) model, and the King (1966) models to the density profiles. The EFF model is very similar to the Plummer model used to set up our clusters. The only difference could be the slope of the density distribution at large r. This would allow us to compare our resultant cluster to the parents directly to see if changes in the resultant cluster density profile come more from the tail or the core. We bin our data using `Clustertools`.

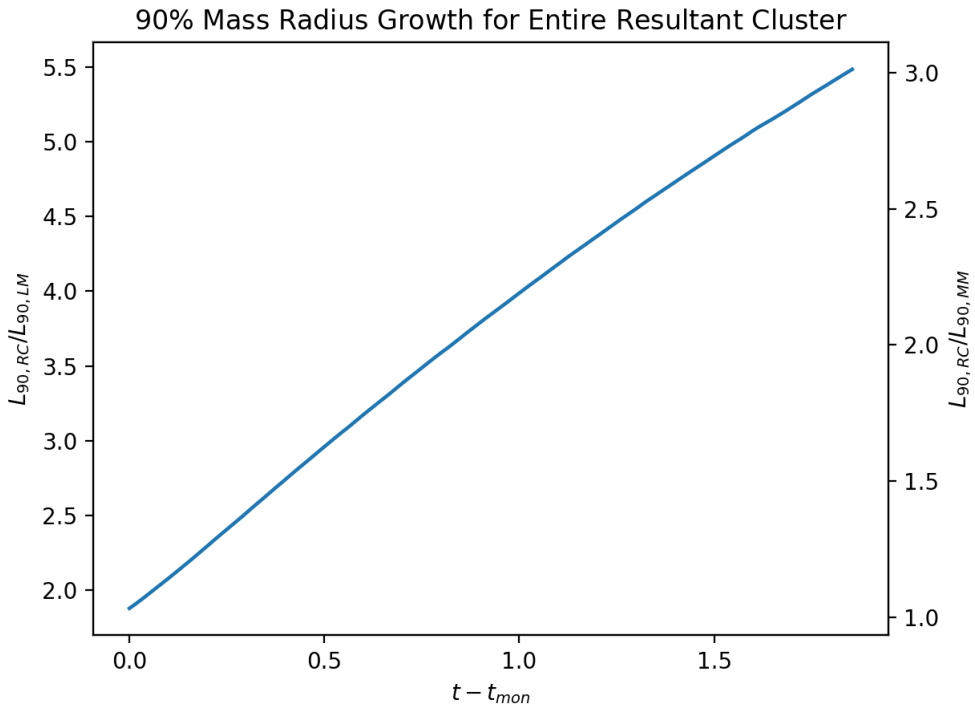

FIGURE 3.5: 90 per cent mass radius for entire (stars and gas) resultant cluster. Y-axes show fractional growth in $L_{90,RC}$ when compared to the more massive (left y-axis) and less massive (right y-axis) parent clusters.

Our bins are centered on the density centre for the stellar component and the density centre for the gas component (the location of highest density in the gas distribution (Portegies Zwart et al. 2010)). For both the stellar and gas components, we find that our choice of density centre over centre of mass does not greatly affect our best fit parameters for any of our models.

We choose $N_s = 25$ radial bins for the stellar component and $N_g = 100$ radial bins for the gas. These values allow us to keep important density characteristics without introducing noise (having too many bins forces us to have too few particles per bin). We then use the `python` function `curve_fit` which uses the Levenberg-Marquardt (LM) method (Levenberg 1944) to minimize the χ^2 and calculate the best fit parameters for each model. We limit our analysis to times t_{mon} and beyond. At this point, the stellar component of the resultant cluster has become monolithic which is a requirement of the 3 models we have chosen.

As a reminder, the EFF model is given by

$$\rho = \rho_0 (1 + \frac{r^2}{a^2})^{-\frac{\gamma+1}{2}} \tag{3.1}$$

The two parameters allowed to vary in the above EFF model are the scale radius a, and the slope of the density tail γ. Note that the Plummer density profile is the same as equation 1 but has $\gamma = 4$ meaning that in the Plummer model, only the scale radius a is allowed to vary. The King (1966) model is integrated using `galpy`[1] and has two parameters that are allowed to vary: the tidal radius of the cluster r_t and W_0 which is a dimensionless number that represents the depth of the potential well created by the distribution. We applied the `curve_fit` algorithm to the stars and gas throughout the evolution of the cluster, to obtain all best fit parameters as a function of time. To

[1] https://github.com/jobovy/galpy

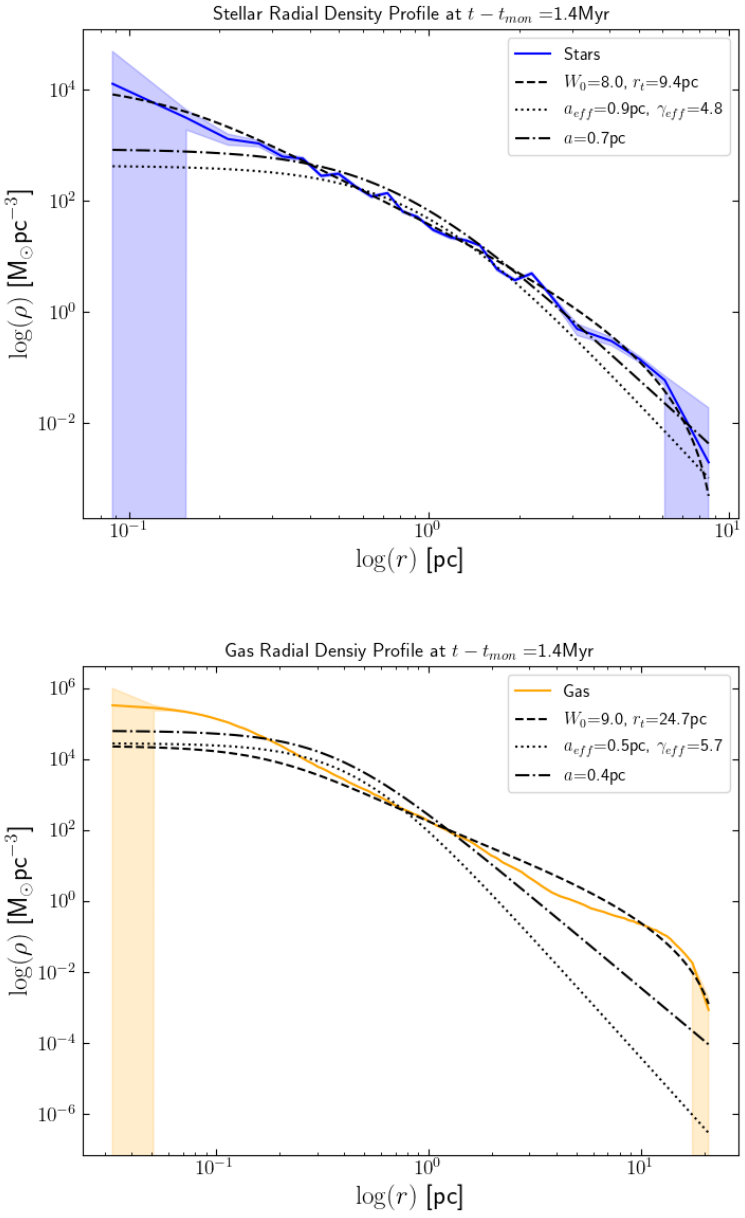

FIGURE 3.6: Stellar and gas radial density profiles plotted with best fit profiles from three theoretical functions: Plummer (dot-dashed), EFF (dotted), and King (dashed). The shaded regions show one standard deviation in the density calculation for a given radial bin.

compare our three models, we analyze the reduced χ^2 (χ^2_{red}) for each model as a function of time, and take the minimum of the three. The corresponding model is thus the one that has minimized χ^2_{red} for that given timestep. We show the snapshot of our analysis at which both the stellar and gas components are fit to the three profiles with the minimum χ^2_{red} in figure 3.6.

We find that the three models above do not fit the density profiles of our resultant cluster well. These three models are best used to describe spherical clusters that have had time to dynamically relax and whose velocity distributions have come closer to Maxwellian (i.e globular clusters) (Mackey and Gilmore 2003b). In contrast, our newly formed resultant cluster has only been alive for a small fraction of its relaxation time and is therefore nowhere near the dynamical state expected for one of these profiles. From our best fits however, we find that the merger process has steepened the surface density in the tail end of our stellar and gas density profiles ($\gamma = 4$ merges into $\gamma = 5$). Furthermore, the $W_0 = 8.1$ for the stars and $W_0 = 9$ for the gas King profiles are consistent with a centrally concentrated cluster as expected after a merger process due to the compactness of the core and the expansion of the outer regions of the cluster.

We conclude that these models can represent the general shape of our stellar and gas components. Furthermore, they can put constraints on what simulators can use as their initial conditions when setting up clusters that are the results of one previous merger.

3.2 Bringing it all Together

In the previous section, we discussed many of the important parameters that help us understand our resultant cluster that is the result of a single merger. This discussion centred around run 3 shown in table 2.1. However, one merger simulation is not a representative sample of the H18 GMC collapse simulation (see figure 2.4). In this section we look at the parameters discussed in section 3 for every merger simulation in

our sample and look for relationships between these parameters and the dimensions that make up our parameter space of interest.

3.2.1 Monolithic Time, Bound Cluster Members and the Parameter Space

We begin with the monolithic time t_{mon}. We calculate t_{mon} for every simulation using the method outlined in the previous section, but tailor it to each individual simulation. Note, there are three simulations whose t_{mon} exceeds the length of the simulation t_{sim}, and we will discuss those in a later section. However, we include them on the plots as "x" symbols. The values plotted for these simulations represent a lower limit to the monolithic time for that given simulation. These mergers result in two clusters whose stellar components are not monolithic by the end of our simulation. However, we are still able to calculate a collision time as the time when the gas cloud's density centres overlap along the x-axis for the first time.

We first show the monolithic time against the collisional velocity in figure 3.7. On the y-axis, we show the monolithic time subtracted by the collision time which tells us how long after each simulation's collision does the resultant cluster become monolithic.

The general trend we see from figure 3.7 is that higher collisional velocity leads to longer $t_{mon} - t_{col}$. There does not seem to be a clear relationship between $t_{mon} - t_{col}$ and f_M. Less massive clusters that are given a larger velocity kick towards the more massive cluster in a merger pair, enter the collision with a high kinetic energy stellar component. Because the stellar component is collisionless compared to the gas component, stars belonging to the less massive cluster pass through those of the more massive cluster at higher velocities, and thus move farther away from the rest of the cluster before being pulled back by gravity. In the simulation with the highest f_M, run2to1, strong gravitational pull-back from the more massive cluster onto the less massive cluster, causes

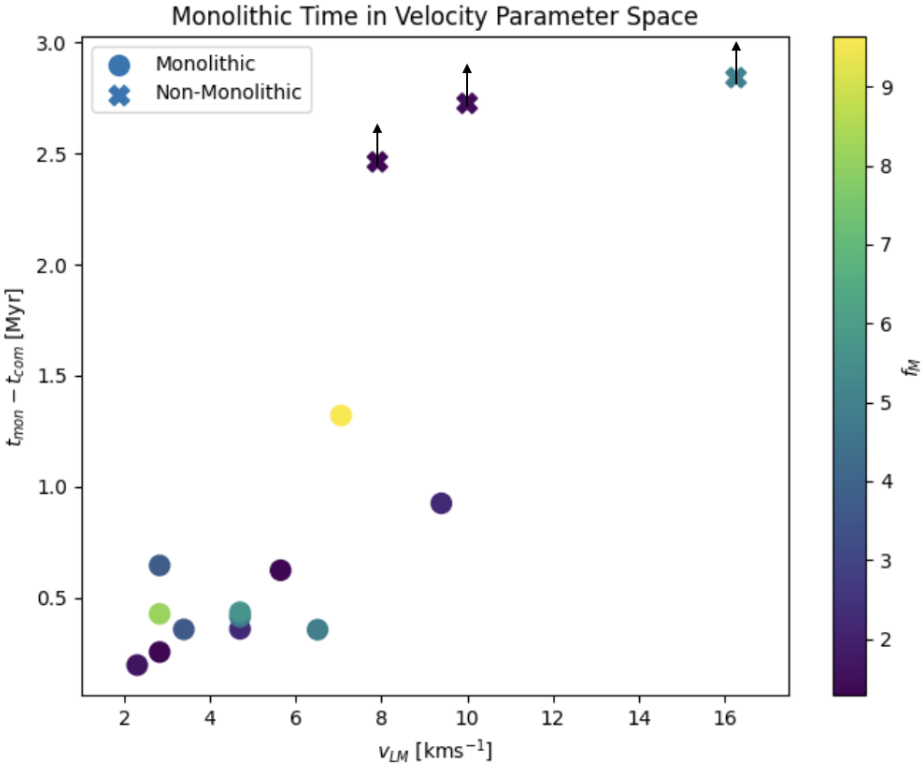

FIGURE 3.7: $t_{mon} - t_{col}$ plotted against the collisional velocity v_{LM} of each simulation. The colourbar values represent mass ratio f_M of each merger. We show both the monolithic ($t_{mon} < t_{sim}$) simulations and the non monolithic ($t_{mon} > t_{sim}$) simulations. The arrows indicate that this is a lower limit of the monolithic time for the non monolithic simulations.

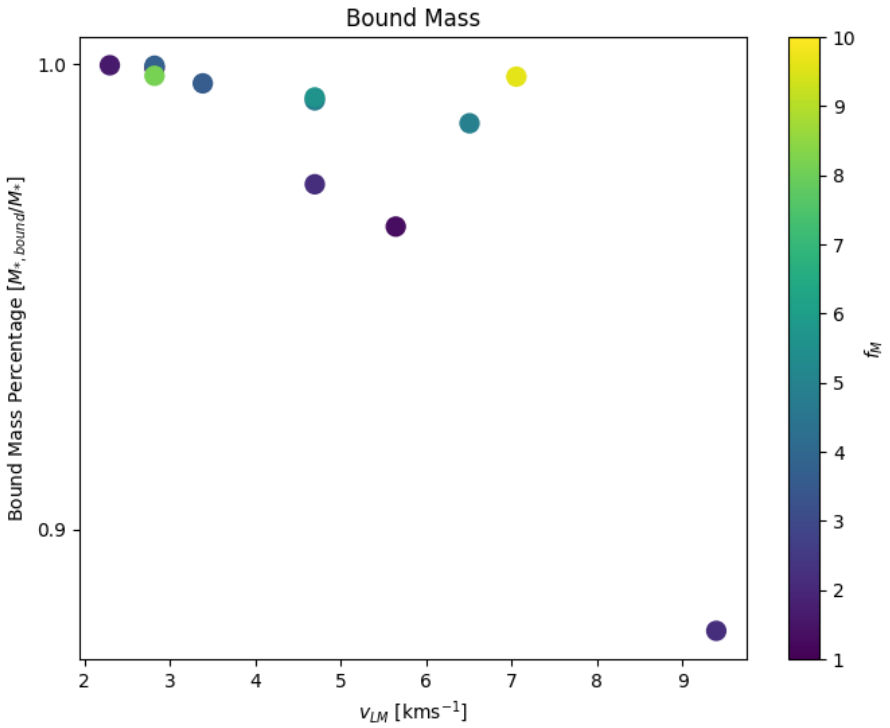

FIGURE 3.8: Remaining bound stellar mass percentage at $t - t_{col} = 0.4$Myr for all mergers whose $t_{mon} < t_{sim}$

the less massive cluster to oscillate around the core of the more massive cluster multiple times until the two finally merge. In cases with lower mass ratios such as run2to3, the less massive cluster stars only pass through the more massive cluster stars once, and do not oscillate once pulled back.

The clusters whose $t_{mon} > t_{sim}$ tend to exist at $v_{LM} \gtrapprox 10\text{kms}^{-1}$ with fairly low f_M. These are our non-monolithic simulations. In these simulations, the stellar components of both clusters never recombine after t_{col} and the resultant state of the merger does not have a monolithic stellar component. The gas component, on the other hand, may be monolithic. This is dependant on the densities of the merging gas clouds (see section 3.4).

From section 3.1.1, we found that the merger process results in a relatively low percentage of stellar and gas mass becoming unbound from the resultant cluster. For the stellar component, this unbound percentage remains constant after t_{col}, but for the gas component, the loss of mass is consistent throughout the simulation after a given simulation's t_{col}. We check to see whether or not there are any correlations between the unbound mass percentage of our resultant clusters and v_{LM} or f_M and find that, consistently, $\lessapprox 5$ per cent of the stellar mass becomes unbound in our resultant cluster at $t - t_{col} = 0.4$Myr as seen in figure 3.8. Because Sills et al. (2018) and Banerjee and Kroupa (2015) find that subcluster mergers tend to happen promptly within 1Myr in their cluster simulations, we can also look at the unbound percentages at $t - t_{col} = 1$Myr. This has the added benefit of applying to GMC regions with lower sink particle number density in which sink particles do not merge as quickly as found in the densest regions of H18. In this case, the unbound stellar mass percentage does not change at all compared to the case where $t - t_{col} = 0.4$Myr. Mergers with higher velocity and lower mass ratios tend to lose more mass, but only in our extreme simulations run3_2v which has a collisional velocities of $v_{LM} \approx 9.4\text{kms}^{-1}$ and mass ratio $f_M \approx 2$ do we lose more than 5 per cent of the stellar mass. In this simulation, we lose 12 per cent. The unbound gas mass percentage behaves in a similar way (strong dependence on v_{LM} and no clear dependence on f_M). However, the unbound gas mass percentage is significantly lower than that of the stars. At both $t - t_{col} = 0.4$Myr and 1Myr, the percentage lies below 1 per cent. Therefore, although a resultant sink particle loses mass after the merger process, the percentage of mass loss is very small before the resultant cluster is likely to merge with another. Not including mass loss in the sink particle prescription is acceptable.

3.2.2 Cluster Growth and the Parameter Space

In order to compare the growth of the inner regions of our resultant cluster for all of our simulations, we look at the growth of the core radius and half mass radius. We average each radii over a given time period and normalize that average by the value of that radius for the more massive cluster before the merger. We choose two time periods for comparison, $t - t_{mon} = 0.4$Myr and $t - t_{mon} = 1$Myr which represent the average time between first and second merger in H18 and the timescale for prompt subcluster mergers from Sills et al. (2018) and Banerjee and Kroupa (2015).

Regarding our normalization, choosing the less massive cluster tells us nothing about how the resultant cluster changes after the merger whereas by choosing the more massive cluster, we gain insight into how the merger process affects the resultant cluster. Therefore, by choosing to look at r/r_{MM}, where r is the radius in question of the resultant cluster, and r_{MM} is that same radius for the more massive cluster initially, we can say that low values of this fraction imply no change in the resultant clusters Lagrangian Radii, and high values imply large change.

We further restrict our analysis in this section to simulations whose $t_{mon} < t_{sim}$. Because this section relies on the calculation of the core radius, and Lagrangian Radii, we cannot consider resultant clusters who are not monolithic. This still leaves us with 12 simulations to consider. We analyze the growth of our simulations whose $t_{mon} > t_{sim}$ in a later section.

Beginning with the stellar component averaged until $t - t_{mon} = 1$Myr as seen in figure 3.9, we find that there is not much of a dependence of the growth in the resultant cluster's core radius on the v_{LM}. However, we find a strong dependence of this growth on f_M. As we get to higher f_M values, we are looking at more minor mergers ($M_{MM} >> M_{LM}$) and, in this limit, the resultant cluster's growth is very minimally affected by the less massive cluster which results in a plateau at $r/r_{MM} \approx 1$ for high f_M. We find that

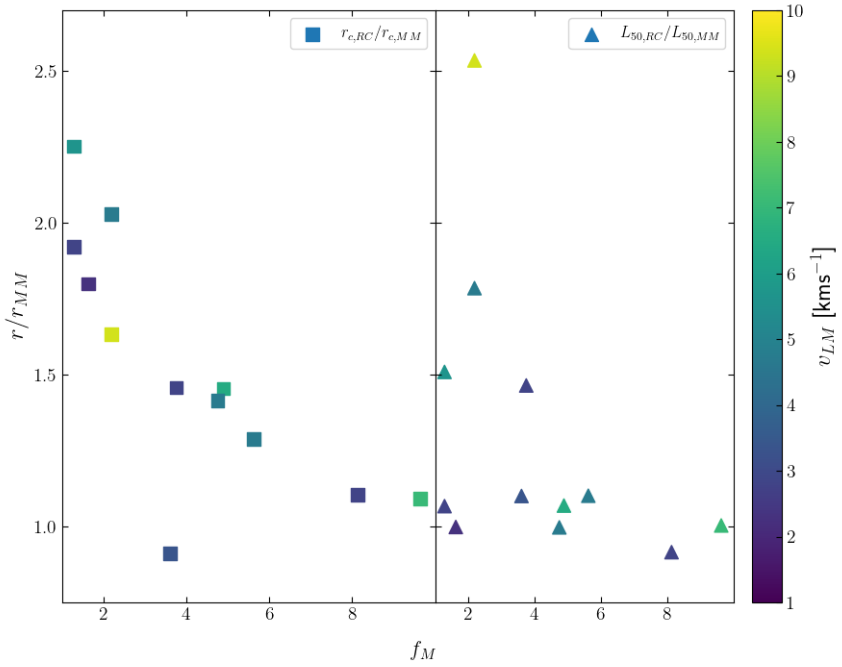

FIGURE 3.9: Inner regions of stellar component of resultant cluster plotted against mass ratio f_M for simulations whose $t_{mon} < t_{sim}$. We average the core radius (left) of the resultant cluster from $t - t_{mon} = 0$ to $t - t_{mon} = 1$Myr and divide it by the core radius of the more massive cluster before the merger such that we can compare understand how much the resultant cluster has `grown` after the merger process. This normalization also allows us to compare all of our simulations to one another on the same space. We do the same for the half mass radius on the right.

the collisional velocity does not seem to have any effect on this trend until we get to the half mass radius, where we find that the trend with f_M starts to disappear due to scatter. High kinetic energy stars originally belonging to the less massive cluster are able to make their way to the outer regions of the cluster where the potential energy is lower and remain there for the remainder of the simulation. This correlates with the slight dependence of the growth in the half mass radii on v_{LM} we see.

At low f_M, because the masses of both clusters are similar, the core of the resultant cluster has gained a significant amount of stellar mass which causes it to grow. Conversely, for high f_M, the stellar core of the resultant cluster gains a fairly small amount of stellar mass compared to the mass of the more massive cluster, and responds by growing very slightly. This tight trend is not present for the half mass radius because it is more dependant on the kinetic energy of the incoming cluster. The half mass radius is located further away from the cluster centre than the core radius which is where many of the high kinetic energy stars are located. We note that in the case where we average up until $t - t_{mon} = 0.4$Myr, the only difference is increased scatter in figure 3.9.

Moving on to the same regions for the gas component, the clear trend with f_M present in the stellar inner region has somewhat disappeared for the core radius. Most of the resultant cluster's core radii have grown somewhere between 1 and 3.2 times their original value. The collisional velocity v_{LM} induces a large amount of scatter in these points. The half mass radius for the resultant cluster gas component $L_{50,RC}$ however, does see a slight trend of decrease with increasing f_M. However, the velocity scatter around the low f_M simulations makes it difficult to ascertain a strong relationship.

Lastly, we can look at the evolution of each simulation's $L_{90,RC}$ as an analogue to that simulations sink particle accretion radius (see section 3.2). We show the values of $L_{90,RC}$ for each simulation, normalized by that simulation's $L_{90,MM}$ plotted for all simulations in which $t_{mon} < t_{sim}$ in figure 3.11. In both plots, it is difficult to see a clear

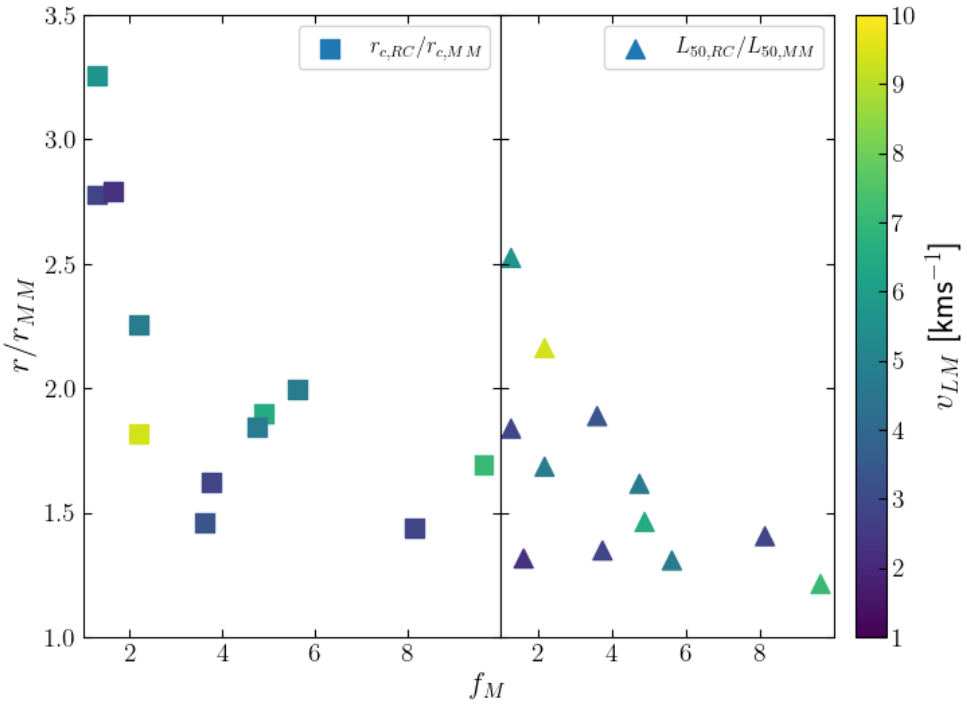

FIGURE 3.10: Same as figure 3.9 but for gas component of resultant cluster.

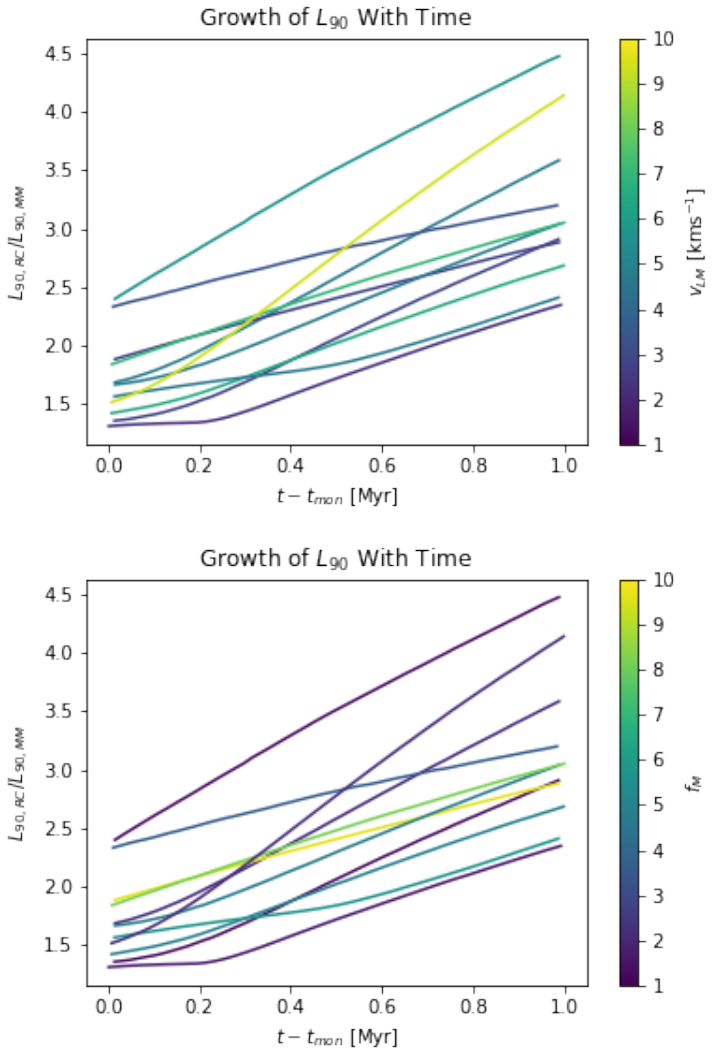

FIGURE 3.11: $L_{90,RC}$ normalized by $L_{90,MM}$ as a function of time after t_{mon} for every merger whose resultant cluster is one monolithic structure.

trend in how the $L_{90,RC}$ grows with either v_{LM} or f_M besides the fact that the merger simulation with the highest collisional velocity has its $L_{90,RC}$ grow at the fastest rate compared to the other simulations. Furthermore, this simulation is in the lower end of the f_M space.

With this, we can conclude that all of our simulations which result in one monolithic resultant cluster exhibit growth in the outer most regions of that cluster after the merger. This growth is absent in the sink particle prescription in GMC simulations. Recall, every sink particle in the H18 simulation is given the same accretion radius $r_{sink} \approx 1.7$pc even those that are the result of previous mergers. Our results show that the star cluster expands after a merger which implies that it cannot be held within a constant accretion radius.

It is important to note that this acts as an upper limit to the amount by which we expect the $L_{90,RC}$ to grow after mergers such as these. In regions where mergers are surrounded by ambient gas, such as a background GMC, the pressures from this background gas would decrease the amount by which the $L_{90,RC}$ grows for our resultant clusters.

3.3 Best Fit Radial Density Profiles and the Parameter Space

Next, we discuss how the three theoretical density profiles (Plummer, EFF, and King, see section 3.1.3) fit to the radial density profiles of all of our simulations in tandem. Similar to the above analysis, we restrict our times to $t > t_{mon}$ because at this time, the resultant cluster is one monolithic form.

We use the same method as in section 3.1.3 to divide our clusters into bins of equal numbers of stars or gas particles. In section 3.1.3 we found that through using 25 and

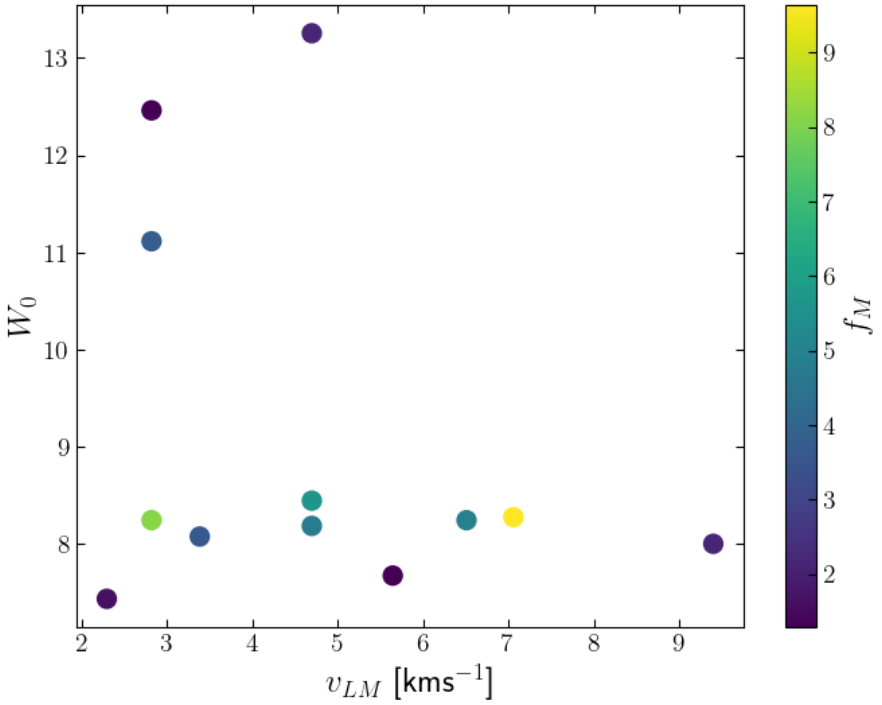

FIGURE 3.12: King W_0 for stellar component of resultant cluster against collisional velocity for all simulations whose $t_{mon} < t_{sim}$. Zocchi et al. (2012) find that King model fits to GCs are best described using $W_0 \approx 7$

100 bins for the stars and gas respectively, there were 80 and 2000 stars or gas particles in each bin. We keep this number of particles in each bin for all of our simulations as it is the resolution at which we find best shows all aspects of the radial density profile of a given component.

For all of our simulations, the range of best fit W_0 values is between 7.5 and 14 with most lying around 8 and only a couple points of scatter above 10. The scatter around a mean of ≈ 8 for W_0 is found at the lower end of the f_M and v_{LM} axes as seen in figure 3.12 which shows the value of W_0 that results in the lowest χ^2_{red} for each simulation plotted against the collisional velocity v_{LM} of that given simulation. This spread indicates that at high mass ratios and low collisional velocities, the resultant cluster can become much

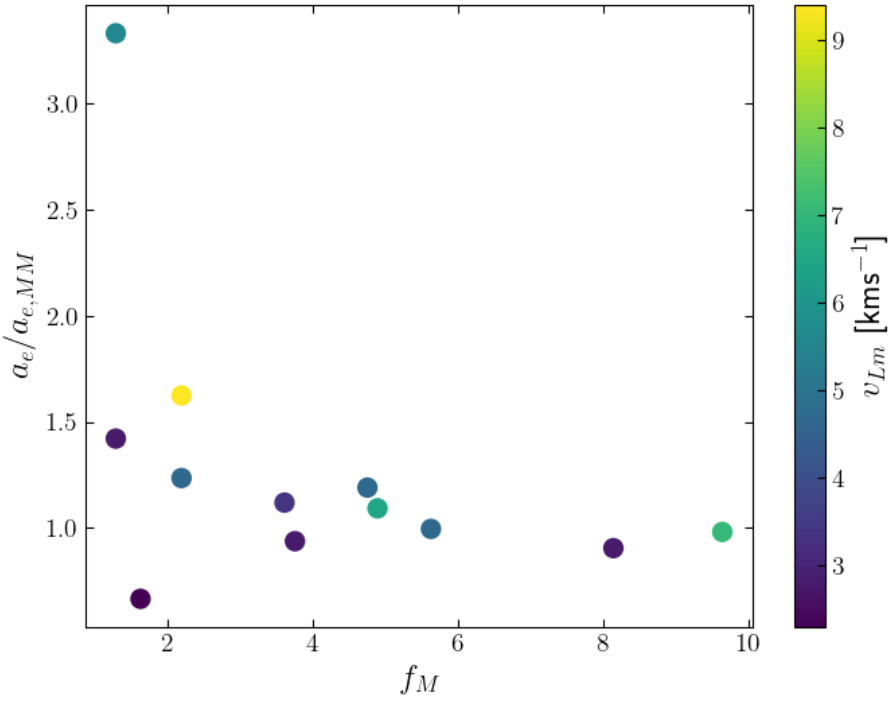

FIGURE 3.13: Best fit EFF scale radii a_e of resultant cluster normalized by that of the more massive cluster before the merger against f_M for the stellar component.

more centrally concentrated than at higher ends of the f_M and v_{LM} axes (as indicated by a high W_0). In other words major mergers can produce more centrally concentrated best fit King profiles, while minor mergers produce shallower models. However, more simulations would help further solidify this conclusion.

Note, for the King model fits, the best fit r_t follows either components L_{90} fairly well. This is a due to the fact that the tidal radius is defined as L_{100} with only slight scatter. The tidal radius is consistently the radial location of the outermost bin in all of our simulations. We therefore refrain from discussing it here as the total L_{90} is more important and has been discussed in section 3.2.2.

We now discuss the stellar components best fit EFF parameters. All of the γ values

for our simulations lie between 4.3 and 4.9 which is growth from the $\gamma = 4$ associated with the Plummer density profile used to initialize our clusters. To compare our best fit EFF scale radii for all of our simulations, we perform a similar analysis to that of the cluster growth: we normalize our resultant cluster's best fit EFF scale radii a_e by that of the more massive cluster before the merger process $a_{r,MM}$. To find $a_{e,MM}$, we do not simply take the scale radius used to set up the Plummer spheres before numerical relaxation. Rather, we fit the cluster to an EFF profile after it has numerically relaxed giving us an initial scale radius and γ_{MM} which we use to normalize our resultant cluster's best fit parameters.

For all of our simulations, we see that the best fit scale radii follows a similar trend as the stellar core and half mass radii found in figure 3.9, namely: there is a slight trend of decreasing scale radius a_e and increasing f_M as can be seen in figure 3.13. However, this decrease towards unity happens much faster for the scale radii and most of the simulations have their scale radii increase by a factor of ≈ 1.2. The best fit γ of the resultant cluster normalized by that of the more massive cluster on the other hand, shows a spread. We find that our resultant cluster's best fit γ increase by a factor of ≈ 1.3 on average. This shows us that the merger process has caused the radial density profiles of the stellar component of our clusters to steepen which is in line with what we find from the best fit King profiles: our clusters become more centrally concentrated.

For the gas component, we see similar behaviour. The King model W_0 values are consistently between 8.4 and 9 and there is no clear trend with either v_{LM} or f_M. However, the χ^2_{red} for all the gas component simulations are orders of magnitude higher than those of the stellar component implying that the gas fits, overall, produce much more poorly than those of the stellar component. The scale radius of the EFF fits of the resultant cluster normalized by that of the more massive cluster follows the same trend as that of the stellar component: decrease in value with increase in f_M. However, while

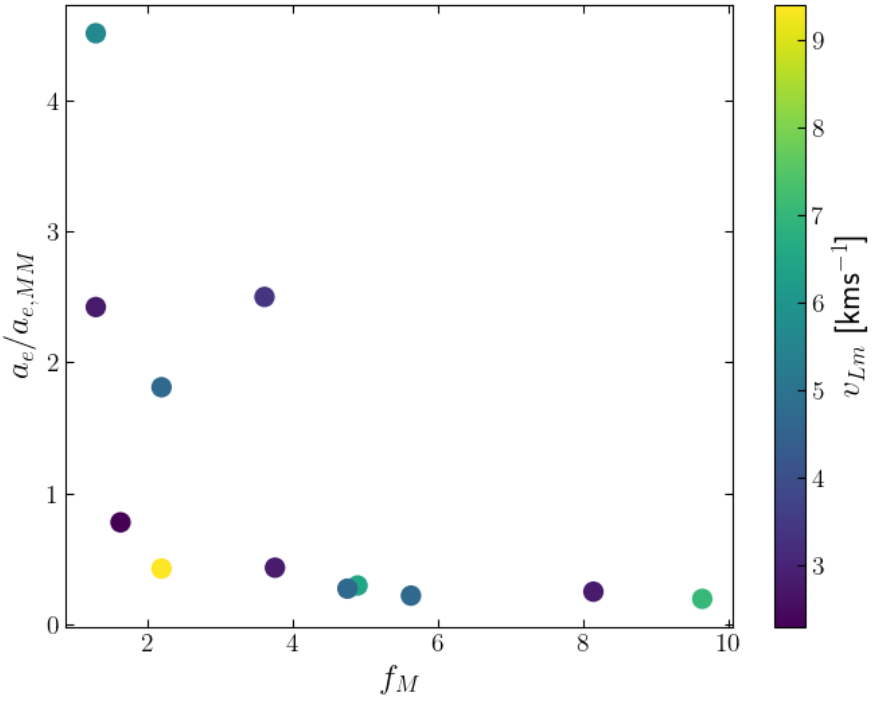

FIGURE 3.14: Same as figure 3.13 but for gas component.

the stellar component's $a_e/a_{e,MM}$ plateaus at 1 with small scatter, the gas component's $a_e/a_{e,MM}$ plateaus below 1 at around 0.3 as seen in figure 3.14 implying that the radial density profiles of the gas components are able to have denser cores after the merger process when compared to the stellar component. As well, converse to that of the stellar component, γ for the gas component EFF fits of the resultant cluster normalized by that of the more massive cluster before the merger shows scatter between 0.07 to 0.8 but always lies below 1. This implies that the power of the tail part of the resultant gas component's best fit EFF model decreases for all of our mergers when compared to that of the more massive cluster. Therefore, the gas components density profile tail becomes shallower which is consistent with the outer regions of the gas component expanding throughout our simulations as seen in the previous sections.

We note here briefly that the Plummer model χ^2_{red} represent very poor fits for all simulations' stellar and gas component. We therefore have refrained from discussing them here.

3.4 Non monolithic Resultant Cluster Cases

We now discuss the simulations whose final resultant cluster does not reach monolithicity by the time our simulation is finished (i.e $t_{mon} > t_{sim}$). The three simulations that satisfy this criteria are run2_2p8v, run5, and run4_2p5v. Their initial conditions can be seen in table 2.1. They all have collisional velocities $\gtrapprox$ 10kms^{-1} and have fairly low mass ratios. To draw an analogue to the sink particle prescription, these simulations should be represented by two sink particles merging and not remaining together as one sink particle, but rather, still being represented as two. We now briefly discuss the merger process for these three simulations. We aim to define what is meant by a "resultant cluster" for these non monolithic simulations.

Beginning with run2_2p8v, as before, the less massive cluster is initiated a distance away from the more massive cluster and given a velocity kick towards the origin. The mass of these clusters is comparatively small when looking at the other runs in our suite. Therefore, any massive stars in these clusters will have a stronger gravitational effect on the system as a whole than on larger clusters. By virtue of the Kroupa IMF used to sample stellar masses for our clusters, a 40M$_\odot$ star is found in our more massive cluster where the average mass is $\approx$ 1M$_\odot$. As the simulation evolves before the merger, both components of the more massive cluster move slightly off the origin. This leads to a merger that does not involve the collision of the two densities centres of both of our clusters. Rather, because the density centre of the more massive cluster has moved off the trajectory of that of the less massive cluster, the density centre of the less massive cluster collides with a diffuse part of the more massive cluster gas cloud. This leads to a

much weaker shock and less energy dissipation allowing for the gas component of the less massive cluster to travel through that of the more massive cluster. Furthermore, due to the collisionless nature of the stellar component, coupled with the high collisional velocity of the merger, the stellar component of the less massive cluster travels through that of the more massive cluster and does not recombine before our simulation is completed (i.e $t_{mon} > t_{sim}$). Therefore, the result of this simulation is two clusters each with their own stellar and gas component, rather than one resultant cluster.

Next, we look at run5. The stellar components of the clusters that make up the run5 simulation act in a similar way to those in the run2_2p8v simulation. That is, they pass through each other and do not recombine by the time our simulation is finished. However, because the stellar components are more massive for both clusters than their counterparts in the run2_2p8v simulation, there is no significant movement of the clusters off of the $y = z = 0$pc axis and the mergers are head on (i.e the density centres of both clouds collide). However, we find that gas originally from the less massive cluster pushes through that from the more massive cluster with only a fraction of it remaining merged with the more massive cluster gas cloud. This process can be seen in figure 3.15. We find that roughly half of the gas remains attached to the more massive cluster after the collision, and the other half leaves with the stellar component of the less massive cluster, thus again resulting in two clusters after the merger. To make the distinction between both clusters, we use the density weighted centre of all of the gas particles belonging to the less massive cluster. This density weighted centre is roughly half way between both of the new clusters for the duration of our simulation. We therefore call all gas to the left of the density weighted centre the new less massive cluster, and all to the right is the new more massive cluster. With this definition, the less massive cluster loses a large fraction of its gas mass, and the more massive cluster gains a significant amount of gas mass at the collision time. We discuss this more in the following sections.

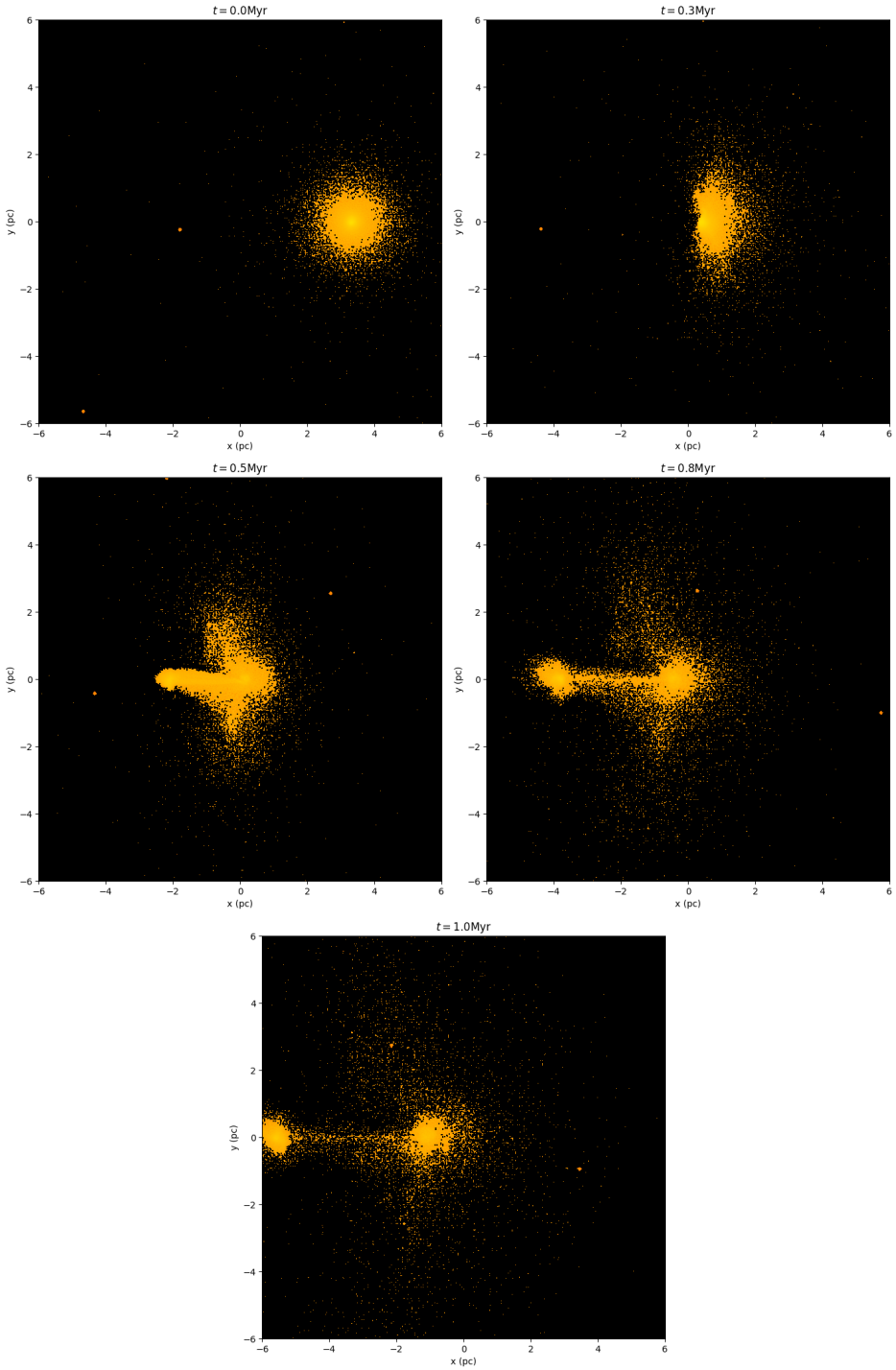

FIGURE 3.15: Evolution of the gas particles that originally belonged to the less massive cluster in run5. We omit the particles that belonged to the more massive cluster here to illustrate that the gas from the less massive cluster mixes with that of the more massive cluster and splits off into its own cluster after the collision.

Lastly, we describe run4_2p5v. This is the fastest of our simulations and the gas clouds are on the larger end in our suite. Because of this, the shock is very efficient at dissipating the kinetic energy of the moving less massive cluster leading to a single monolithic gas component after the collision time. The stellar component however, behaves in a similar way to the previous two runs discussed. Stars belonging to the less massive cluster fly through those of the more massive cluster, and do not recombine by the end of our simulation. Therefore the result here is still two isolated clusters, however the less massive cluster no longer has a gas component and the more massive cluster has gained a large amount of gas mass.

From here on, we refer to this subset of simulations as the non monolithic simulations for simplicity.

3.4.1 Bound Fraction

We begin with a discussion of the bound fraction of stars and gas for these simulations. This is handled differently than section 3.1.1 because we are no longer considering the bound stars with respect to the single resultant cluster. We now change our reference frame to each cluster individually. To do so, we calculate the potential energy of a given star or gas particle in our simulation and compare it to that particles kinetic energy after subtracting the clusters net velocity. This allows us to determine how many of a given components' particles are still bound to each individual cluster after the merger which we translate to a mass fraction by dividing the total mass by that of the clusters before the merger.

We show the unbound percentage of stellar mass for each cluster in each of the three simulations in figure 3.16. From top to bottom, the collisional velocities of these runs are $v_{LM} = 7.8, 10$, and 16kms^{-1}. The green vertical line in each figure shows the collision time of each respective simulation. We see, in the highest velocity case, the less massive

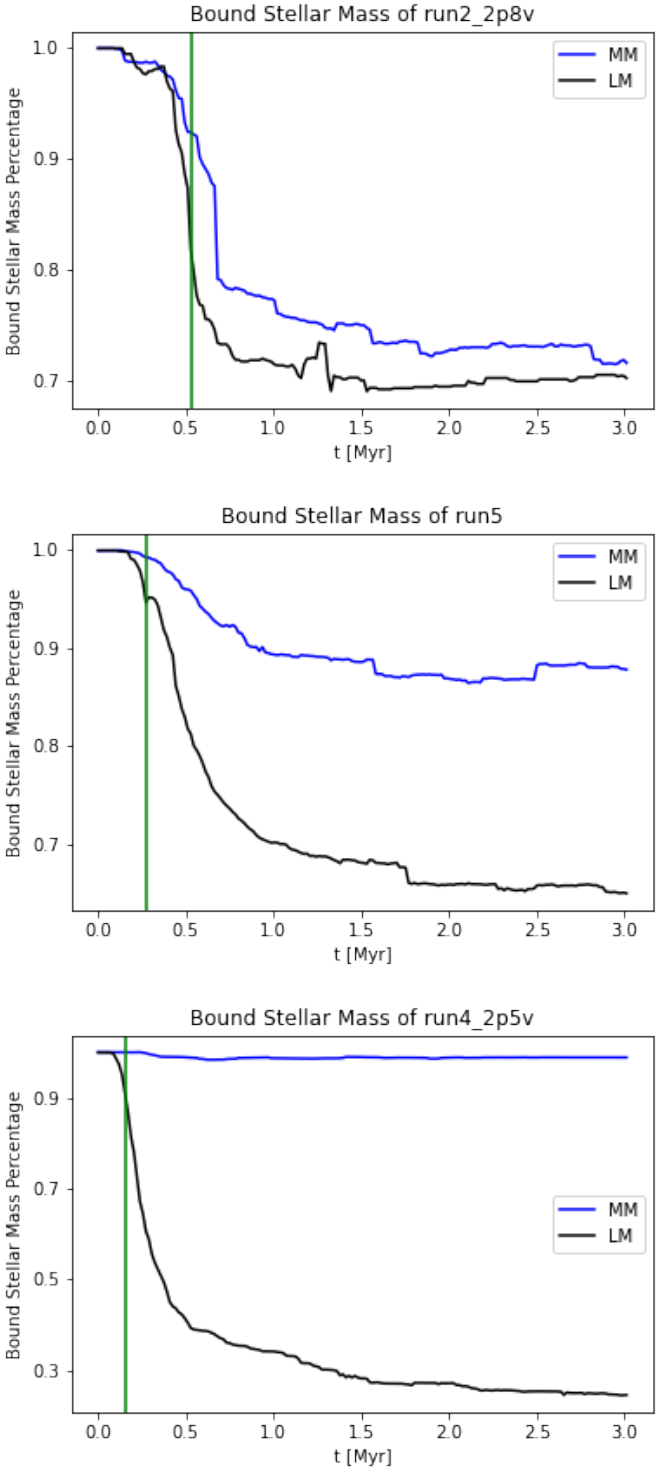

FIGURE 3.16: Remaining bound stellar mass of more massive (MM) and less massive (LM) clusters for the three runs whse result is not one monolithic cluster. The green lines show the collision time for each respective simulation.

cluster loses up to $\approx 72\%$ of its total stellar mass after the merger process yet the more massive cluster is nearly unaffected, losing only $\approx 4\%$ of its total stellar mass. In the lower velocity cases however, the more massive cluster does lose a non-negligible amount of stellar mass compared to that of the less massive cluster. In the lowest velocity case, the more massive cluster even ends up losing a comparable amount of stellar mass to that of the lower mass cluster. This result implies that sink mergers whose resultant cluster is not a monolithic cluster, such as the ones shown here, must account for mass loss much more than those whose resultant sink is monolithic as they are much more sensitive to higher velocity mergers. We note that the mass loss here is much higher than in the case of a monolithic resultant cluster where the maximum stellar mass lost was only slightly above 10 per cent.

We now perform the same analysis for the gas component of the resultant clusters after the merger has taken place. Recall, for the special cases of run5 and run4_2p5v, the gas component of the result is not the same as the initial gas components before the merger as described above. All of these mergers can be seen in 3.17. For run5, we see that the more massive cluster gains an amount of mass after the collision time and that the less massive cluster loses a very significant amount of its total mass. The bound gas mass of run4_2p5v behaves very similarly to the bound gas mass of the monolithic simulations in the previous section due to its monolithicity after the merger. However, it loses more mass than those clusters. Lastly, run2_2p8v has both the gas clouds losing mass in a similar way to the monolithic gas cloud cases, but at a slightly higher rate. Compared to the <5 per cent bound gas mass loss of the previously analyzed monolithic simulations, the gas mass loss (or gain) is much more drastic here due to the high velocity of these mergers. Furthermore, we find that in the run where the resultant gas component remains monolithic, the stronger shock that takes place turns much of the kinetic energy into heat and therefore, causes less of the total gas mass to become gravitationally unbound.

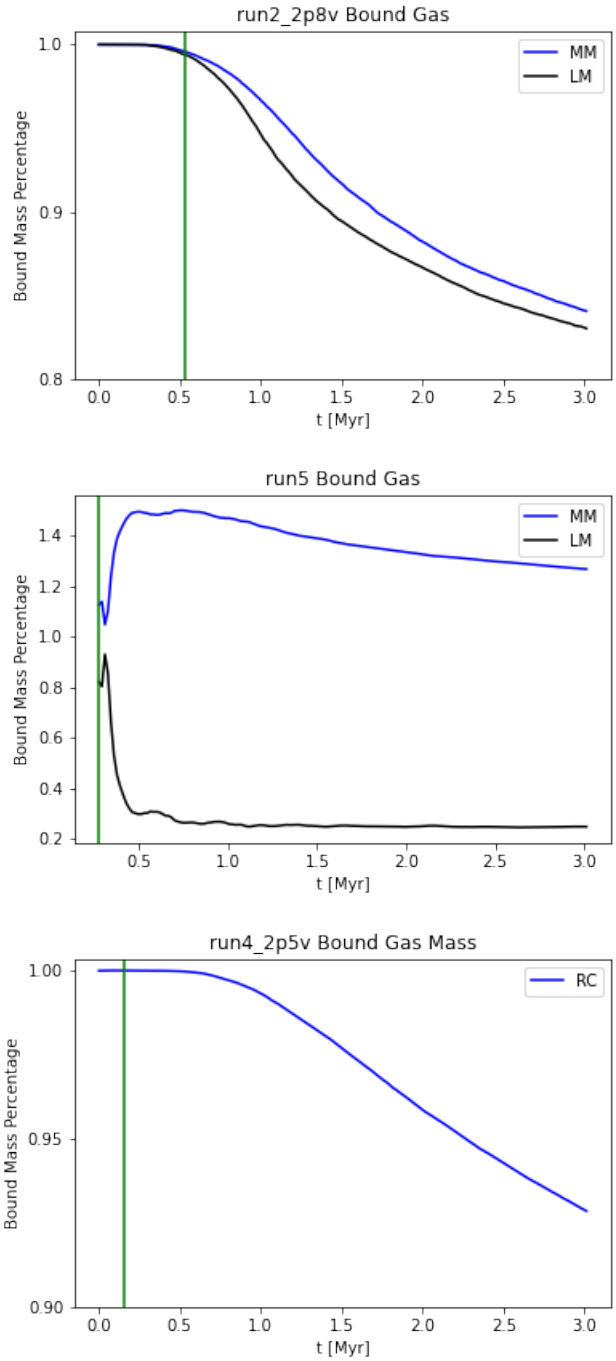

FIGURE 3.17: Same as figure 3.16 but for gas. Final plot only contains bound mass fraction of gas for final monolithic gas component *RC*

As seen in figures 3.16 and 3.17, all of these resultant clusters lose significant amounts of stellar and gas mass by the time they are expected to merge with another cluster. If we look at these unbound fractions at $t - t_{col} \approx 1$Myr, we find that the bound mass lost is a fairly large fraction of the total mass of the cluster. In a GMC simulation involving sink particles, this behaviour would result in a large discrepancy in the final mass of the YMC sink particle meaning that mergers with collisional velocities $\gtrapprox 10\text{kms}^{-1}$ should have their unbound stellar and gas mass accounted for.

3.4.2 Cluster Size

After the collision time, we look at how the core radius and half mass radius of our clusters evolves with time. For runs 2_2p8v and 4_2p5v, the half mass radii of both clusters do not change significantly and for run5, the core radii of both clusters, on average, do not change after the collision. The core radii of these simulations show much noise around a given value making it difficult to discern any trend for these clusters. On the other hand, the noise in the evolution of the half mass radii for these simulations is much less prevalent throughout the cluster's evolution. We show these half mass radii in figure 3.18. The only significant change in the stellar component half mass radii occurs in the clusters from run5 where we see increases for both clusters. In the other two simulations the only movement away from $L_{50}/L_{50,0}$ is around the collision time. We therefore see that the merger process introduces little to no expansion in either cluster's stellar component for our monolithic runs although.

Plotting these onto figure 3.9 along with the stellar component core radii for our non monolithic clusters, allows us to compare our non monolithic resultant cluster simulations to our monolithic ones. This can be seen in figure 3.19. We see that for the core radius, our non monolithic resultant cluster simulations lie below the trend discussed for our monolithic resultant cluster simulations. Both clusters stellar components that come out of these non monolithic simulations tend to grow less than the one resultant cluster in our

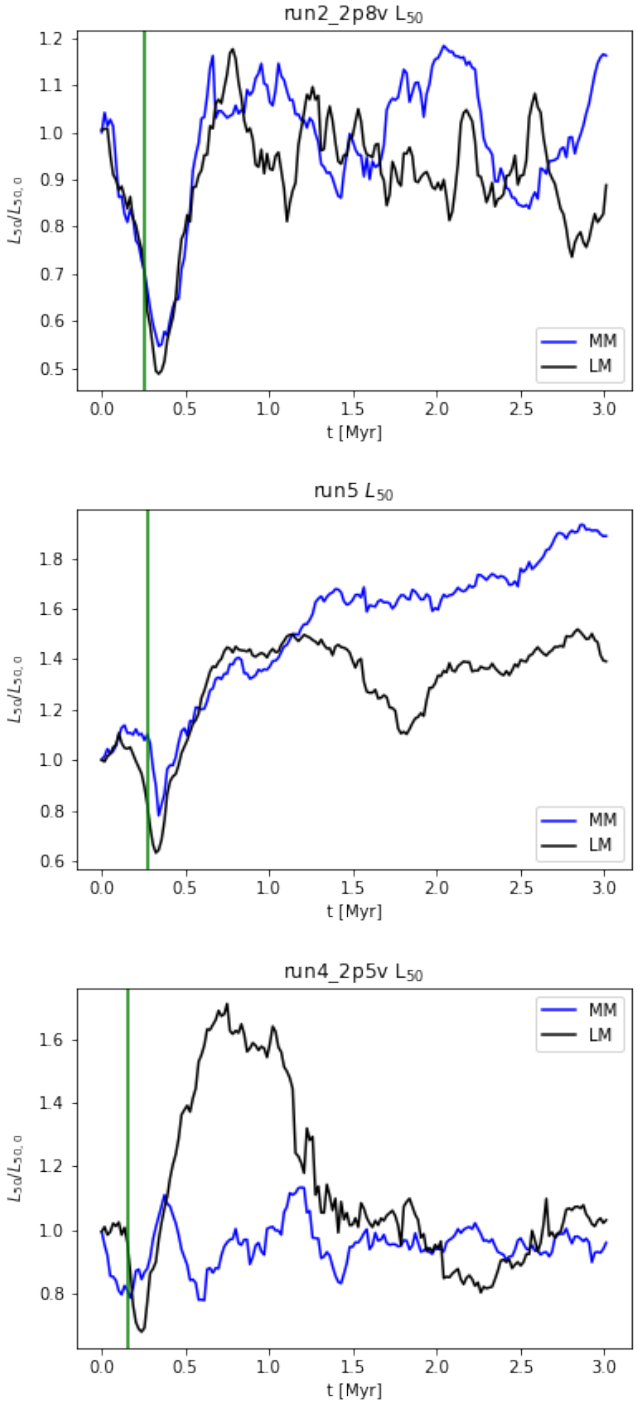

FIGURE 3.18: Evolution of the half mass radii of both clusters from all non-monolithic runs. The y-axis has been normalized by the value of the half mass radius of the cluster before the merger. The green vertical line shows the collision time for each simulation.

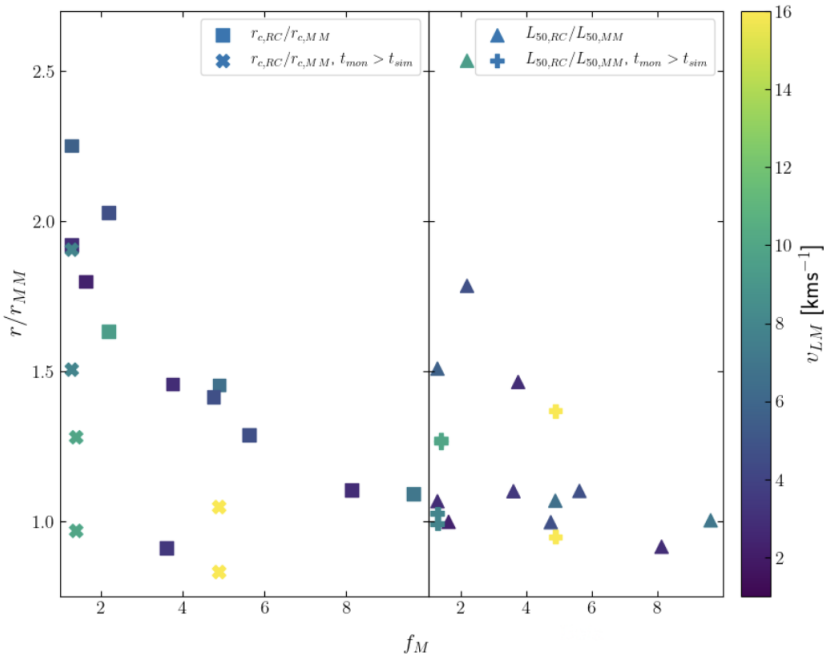

FIGURE 3.19: Same as figure 3.9 but now including non monolithic resultant cluster simulations.

monolithic simulations. This is expected as the single resultant cluster of our monolithic simulations contains most the material of both clusters involved in the merger (save for some unbound stellar and gas mass). Conversely, the non monolithic resultant clusters pass through each other and lose much more mass as a result of the collision.

We now perform the same analysis as above for the gas component of our resultant clusters. The growth of the gas component's core radii and half mass radii can be seen in figure 3.20 where we have normalized the values of the resultant clusters core and half mass radii by those of the initial clusters before the merger.

We see from these plots that there is growth in both the core radii, and half mass radii of the gas components of all clusters after the mergers. We also see that the growth of the gas components of runs 2_2p8v and 5 is much higher than that of any simulation whose final gas component is monolithic as seen by comparing these results to those

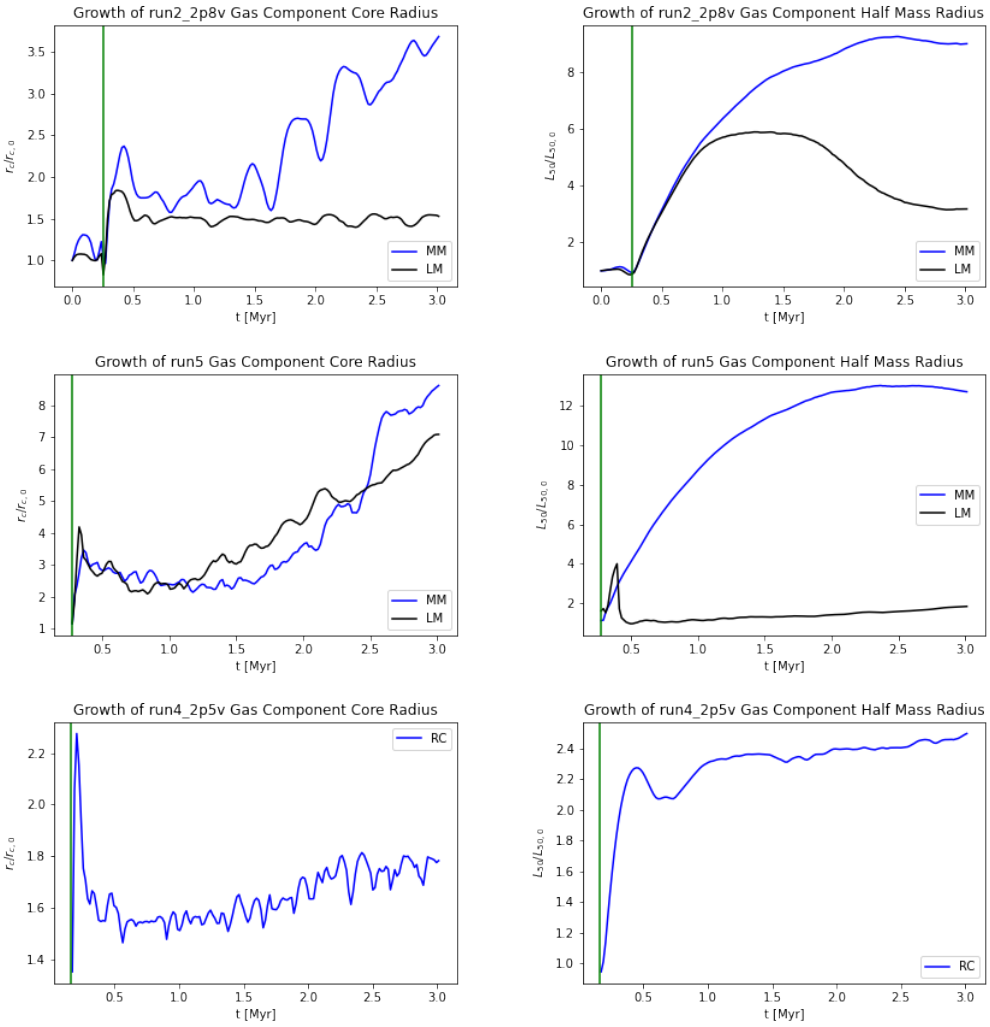

FIGURE 3.20: Growth of the gas component of all simulations whose $t_{mon} > t_{sim}$. We focus on the growth of the core radii and half mass radii of each cluster that results from the given merger. In all plots, the green vertical line shows the collision time for that merger simulation. For runs 5 and 4_2p5v, the green line is at the beginning of the plot because either the definition of each cluster changes after the merger (run5) or the resultant cluster gas component is monolithic (run4_2p5v).

shown in figure 3.10. Lastly, the evolution of the core radii and half mass radii for these cluster after the merger differ from the rest of the clusters shown in figure 3.10: they do not remain constant after the merger. In particular the half mass radii of runs 2_2p8v and 5 show change throughout the entirety of the simulation. Because of this, we cannot average over a given time period to obtain a single value that can be plotted on figure 3.10 as we did with figure 3.19.

As done for our $t_{mon} < t_{sim}$ simulations, we can look at how our sink particle accretion radius analogue, the 90 per cent total mass radius $L_{90,RC}$, changes after the merger simulation. The difference here is that we are concerned with this value for both of our clusters rather than just the single monolithic cluster after the merger. However, for the case of run4_2p5v, the less massive cluster loses all of its gas at the collision time and the more massive cluster now has the stars it originally contained including the gas components from both clusters.

These plots can be seen in figure 3.21 where we have normalized $L_{90,RC}$ by this value of each respective cluster before the merger $L_{90,OC}$. As before, this would result in further delay of gas accretion onto the sink particles in a GMC simulation context. We see here that run4_2p5v is the only simulation in which the more massive cluster's $L_{90,RC}$ grows more than that of the less massive cluster due to the extra gas mass it has picked up from the merger process as described above. Furthermore, the less massive cluster loses much of its stellar mass by the end of the simulation implying a much smaller bound component and, in turn, a smaller increase in $L_{90,RC}$.

Very similar to the simulations whose $t_{mon} < t_{sim}$, our sink particle accretion radius analogue grows throughout our simulations after the collision time for each of the non monolithic simulations. We plot our sink radius analogue for the non monolithic clusters in figure 3.22. By comparing with figure 3.11, we can see that the slope of the growth of the $L_{90,RC}$ tends to be similar for mergers with similar collisional velocities. Higher

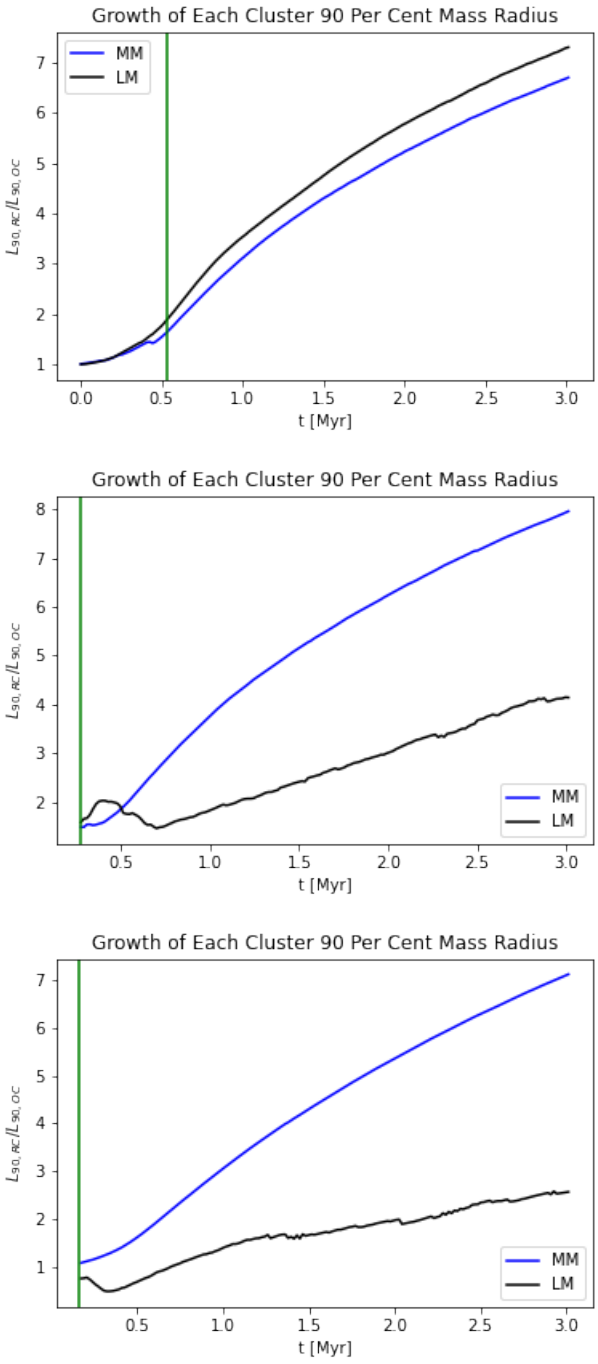

FIGURE 3.21: Evolution of both the more and less massive cluster's total 90 per cent mass radius normalized by that cluster's same radius before the merger takes place for runs 2_2p8v, 5, and 4_2p5v from top to bottom respectively. The green line shows the collision time for each respective simulation. For the final two plots, because the our definition of the more and less massive clusters change after the collision time, we begin the x-axis at the collision time.

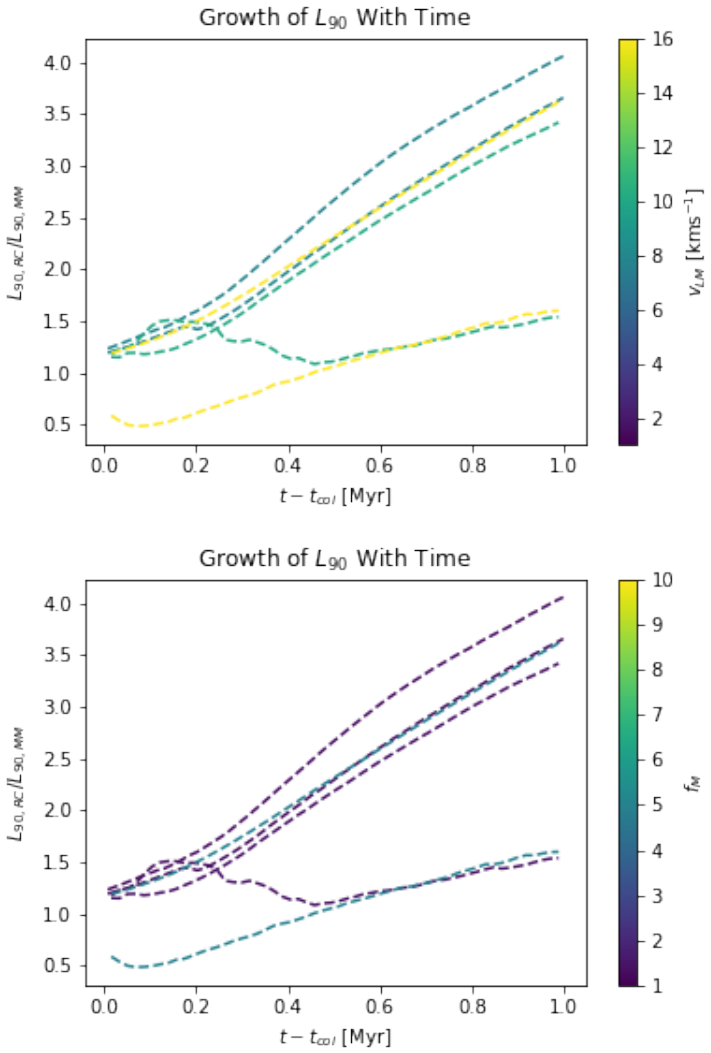

FIGURE 3.22: Same as figure 3.11 but for the non monolithic clusters.

collisional velocities tend to lead to faster growth of the $L_{90,RC}$ for our clusters. There are two outliers in figure 3.22. The first is the less massive cluster of run4_2p5v which, as stated in a previous section, has lost all of its gas due to the collision. The second, is the less massive cluster from run5 which has lost a sizeable amount of its gas mass. However, both of these outliers still grow after the respective clusters have formed and do not show any sign of stopping by the end of our simulations.

This time, because our result is not one monolithic cluster, both cluster's accretion radii would need to increase such that they are not missing out on any potential accreted gas before their next merger.

3.4.3 Best Fit Density Profiles

We finish this section with a brief discussion regarding the best fit density profiles for the stellar and gas components of the clusters after the collision time for the non monolithic simulations. From the previous two subsections, we see that the stellar component of the less massive clusters for all of these simulations lose much of their mass and expand implying that the radial separation of remaining stars in each bin of our radial density profile, has a high error. This is especially true for the less massive cluster in run2_2p8v which is the smallest single cluster in our suite, and in turn, is the cluster with the smallest number of stellar members. For this simulation, it is impossible to keep the number resolution of ≈ 80 stars in each bin without only using 4 bins to describe the resulting density profile of the entire cluster. The same is true for the more massive cluster in this simulation which means that both clusters in this simulation are too sparse for us to model using any of the theoretical density profiles used in the previous sections. Similarly, for the less massive cluster of run4_2p5v which stabilizes at stellar mass loss of up to $\gtrapprox 70$ per cent, we cannot perform fits with any certainty due to the extremely low number of stellar members. Lastly, as stated in the previous section, the gas component that makes up the resultant less massive cluster in run5 is very diffuse

because of all the mass it lost at the collision. Similar to the previous cases, this makes us unable to resolve the radial density profile with any significant certainty and we refrain from showing fits here.

This therefore leaves us with both components from the more massive cluster of run4_2p5v and the more massive cluster of run5, and the stellar component of the less massive cluster from run5.

We begin with the stellar components of both of the run5 clusters as seen in figure 3.23 where we only show the King fit of the more massive cluster. Neither are good fits to the density profiles. We note again that the Plummer fits are so poor that we do not show them here. For both of these clusters, the W_0 values are similar to those of the the stellar components of the clusters in the monolithic simulations. Again, after the merger, the stellar components become more centrally concentrated. Furthermore, the increase in the EFF fits' γ_{eff} is similar as well to those in the monolithic run which again shows that the radial stellar density profiles have steepened which is by a factor of 1.1 and 1 for the more and less massive cluster respectively. The scale radii increase by 2 and 1.6 respectively which is the same trend for this mass ratio as the monolithic simulations.

Moving on to the gas component of the more massive cluster of run5, we find that, after the merger, the best fit King model parameters behave similarly to those of the monolithic clusters. Namely, W_0 has become more centrally concentrated and now lies at 8.7. Regarding the EFF model, the best fit scale radius has decreased slightly by a factor of ≈ 0.7 and the best fit γ_{eff} has stayed roughly the same converse to the monolithic cluster simulations showing that for this simulation, the merger does not greatly affect the tail of the gas density distribution.

Lastly, we show the stellar and gas components for the more massive cluster in

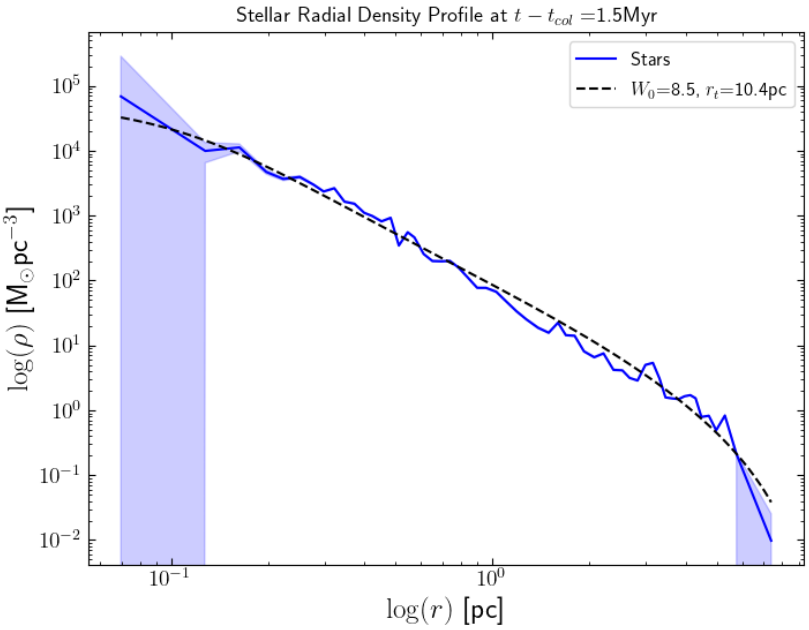

FIGURE 3.23: Best fit stellar radial density profile for the more massive clusters of run5 at the time which minimizes the χ^2_{red}.

run4_2p5v. The King fits can be seen in figure 3.24. Similar to the monolithic cases, the clusters become more centrally concentrated as evidenced by the best fit King W_0 values. Both the gas and stellar component best fit W_0 values lie within the range described by the monolithic runs.

3.5 Star Formation Density Thresholds

Lastly, we can look at the amount by which gas above star forming densities grows during the merger. The subgrid model for star formation employed in H18 involves sampling the gas mass inside a given sink using a Chabrier (2005) IMF at an efficiency of 20 per cent to match star formation efficiencies found in Lada and Lada (2003). This sampling is done once every $t = 0.36$Myr which corresponds to 1 free-fall time for a sink particle in the H18 simulation. By looking at the amount of gas above star forming density

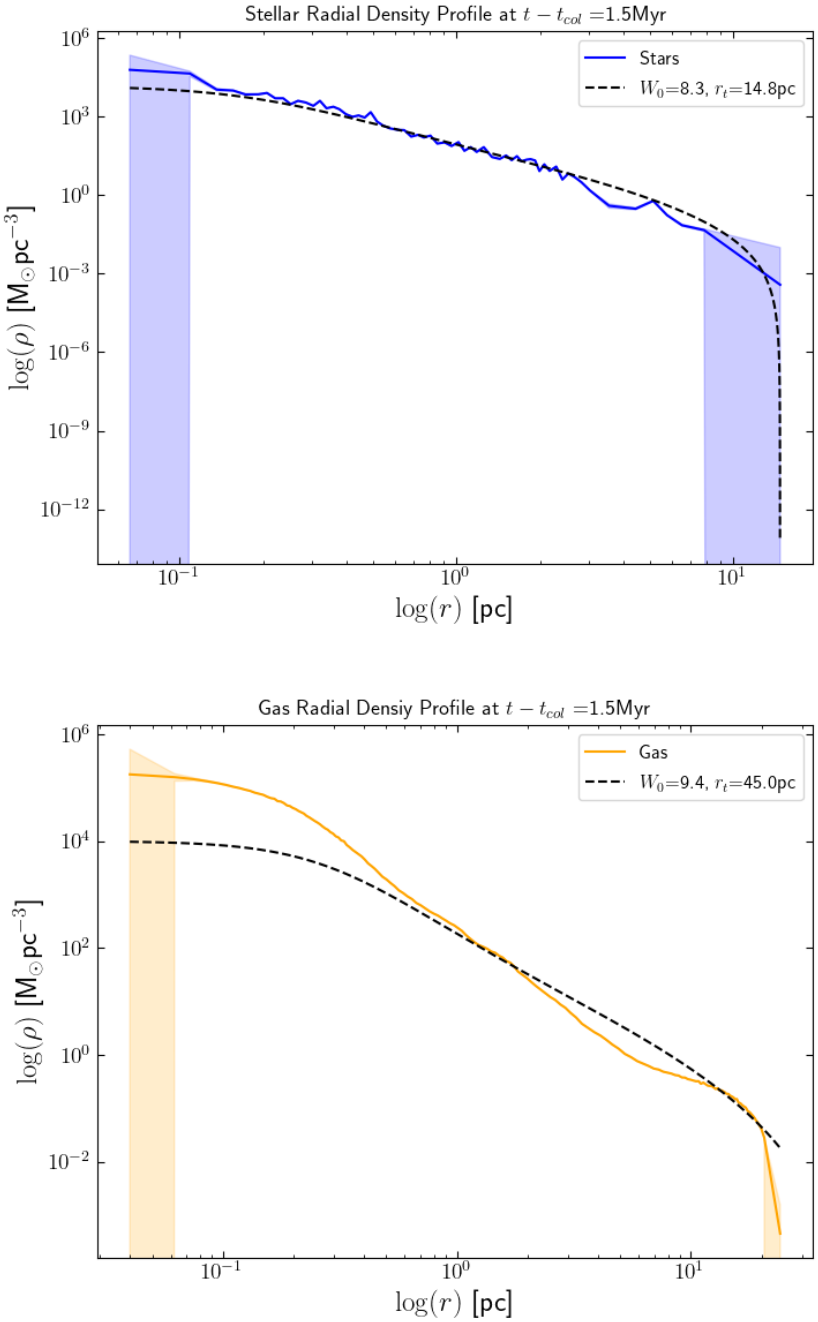

FIGURE 3.24: Best fit theoretical profiles against stellar (top) and gas (bottom) radial density profiles at times that have minimized the χ^2_{red} for that given component for run4_2p5v.

thresholds in our simulations throughout the merger process, we can see how consistent this sampling of 20 per cent is throughout the merger process.

We look at the gas with densities above 10^{4-5}cm^{-3} which is a commonly quoted density above which dense star-forming cores begin to form (e.g Evans et al. 2009, Heiderman et al. 2010, Lada et al. 2010, Lada et al. 2012). Throughout the simulation, we track what percentage of the total gas consists of gas with densities above these values. We show these percentages for gas above $n_1 = 10^4\text{cm}^{-3}$ and $n_2 = 10^5\text{cm}^{-3}$ for run3 in figure 3.25. In these figures, the x axis is in units of 1 free-fall time t_{ff} corresponding to the given density threshold. We see that, around the collision time, the gas percentage above either density threshold peaks. The difference between this peak percentage and the percentage at the beginning of our simulation is approximately 5 per cent for n_1 and 11 per cent for n_2. However, we see that this peak lasts for less than a free-fall time for the gas above n_1 and approximately one free fall time for n_2. Therefore, the increase in sampling efficiency would not be required if the star formation density threshold is chosen to be above n_1 for this merger, as it is for the sink particles in H18. Furthermore, we see that after the merger, the percentage of gas with densities above n_1 and n_2 has decreased by approximately 10 and 7 per cent respectively. Because this decrease lasts for the rest of our simulation, it is important for the sink particle prescription to decrease the efficiency at which it samples its gas mass into stars after the merger has taken place for this run.

Generalizing to all our simulations, on average, the increase in gas mass above n_1 and n_2 is approximately 3 per cent, and 7 per cent respectively. Similar to run3 as discussed above, the peak lasts for less than 1 free-fall time for all our simulations when looking at gas with densities above n_1, and approximately 1 free-fall time for all our simulations when look at gas with densities above n_2. Therefore, during the merger, the sink particle prescription need not change its star forming percentage because the sink particles from

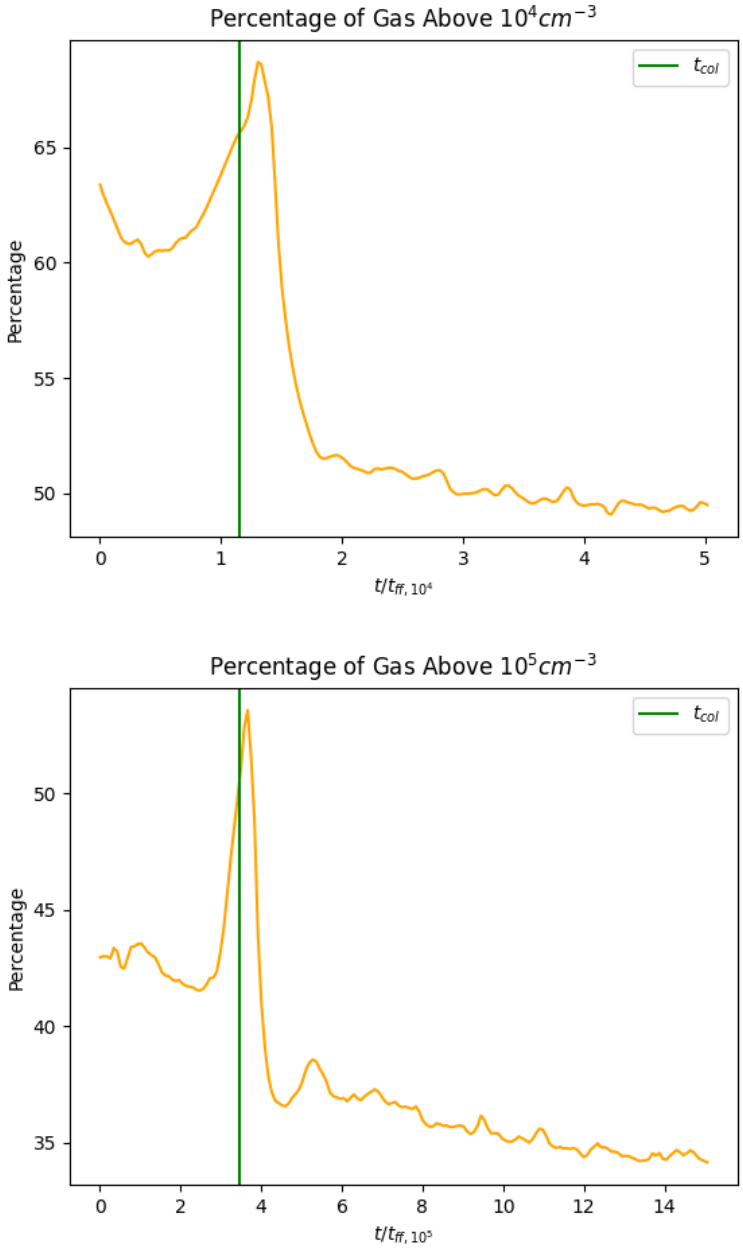

FIGURE 3.25: Percentage of gas above 10^4 (top) and 10^5 (bottom) cm^{-3} throughout run3. Time on x axis is given in units of the free-fall time for that density threshold. The green line shows the collision time t_{col} for this merger simulation.

H18 are at densities of n_1 and this peak lasts for less than a free-fall time. However, for sink particles with densities of n_2, sampling at a constant rate would be underestimating the amount of star formation at the time of the merger. We also find that on average, the gas mass with densities above n_1 and n_2 decrease by approximately 15 and 10 per cent respectively after the merger of two clusters. After the merger, the sink particle prescription is overestimating the amount of star formation inside the sink particle when compared to our simulations.

Chapter 4

Discussion and Future Work

4.1 Resolving Star Cluster Mergers in GMC Simulations

We have taken simulation results from Howard et al. (2018) (H18), who found subcluster formation in the filaments of a collapsing GMC, and have resolved a key component of the subcluster's evolution at higher scales. We have resolved 10 H18 subclusters and have run 15 merger simulations of these clusters. We have shown that most of our mergers result in one monolithic cluster, and all exhibit stellar and gas mass loss after the merger process. This is concerning as it is contrary to the sink particle prescription used in H18 which does not allow for the loss of any mass after a merger between two sinks. However, the mass loss we found was consistently less than 5 per cent which is negligible. We advise that sink particle users keep this mass loss in mind when looking at particularly high velocity sink mergers. In such cases, we find that the unbound stellar mass percentage increases to upwards of 12 per cent. More drastically, in mergers whose collisional velocity is so high that the resultant cluster does not become monolithic by the time our simulations are finished, we find stellar mass loss of at least 30 per cent from the lower mass cluster. It is important to note that these high speeds assoviated with the non-monolithic clusters are not extremely common in the H18 simulations. Furthermore, it is likely that such high speeds are a byproduct of the high mass of their simulated

GMC. Accounting for this mass loss in GMC simulations would require sink particles to be able to release stars into the surrounding environment as N-body particles. The simulations performed by Wall et al. (2019) and Cournoyer-Cloutier et al. (2021) for example, use sink particles as a star particle "factory" that allows sink particles who have accreted enough gas mass to release star particles after sampling from a Kroupa IMF. Such small fractions of mass loss may eventually lead to larger mass discrepancies concerning the final YMC formed in GMC collapse simulations in the following way: we may expect that subsequent mergers will continue to lose mass in stars and gas converse to the sink particle prescription of H18 which does not allow for mass loss in either stars or gas. Therefore, the sink mass quoted by H18 is higher than what we find in our simulations.

We have also investigated how the size of the resultant clusters change after a merger has taken place. Through our analysis of the 15 merger simulations, we have found that all of the resultant clusters grow after the merger process. This, similar to above, is contrary to the sink particle prescription which only allows clusters to be contained inside r_{sink}. The growth of the sink particle accretion radius in a GMC collapse simulation with time would require a change in resolution of the simulation which could lead to problems. However, not allowing the accretion radius of a sink particle may lead to a lag in gas accretion onto sink particles in GMC simulations which may in turn result in further mass discrepancy by the time the next merger takes place as shown by tests performed by Dobbs et al. (2021). The authors find that through increasing their accretion radius by a factor of ≈ 2.5, the mass attainable by a sink particle can increase by one order of magnitude illustrating the importance the accretion radius plays on a sink particle's mass. We therefore suggest that a given sink particle's accretion radius be allowed to grow after mergers with other sink particles.

We have found that while commonly used radial density profiles do not provide good

fits to our resultant cluster's stellar or gas radial density profile, they do help with putting constraints on what is considered an acceptable representation of the radial profile of a merged cluster. For instance, we see that the overall shapes match the three theoretical models tested.

4.2 Future Work

We have developed a method by which we can simulate subcluster formation mechanisms with higher precision, but only in the context of mergers. In the future, we will be simulating the next of the two important subcluster evolutionary mechanisms shown in H18: gas accretion. We can explore the simulating of gas accretion through many avenues. Because H18 found that their subclusters formed mostly inside dense filaments of gas, we can try to emulate this by taking our fully realized clusters (both stellar and gas component), and initiating cylinders of gas around them. These cylinders of gas, as shown by Zavagno et al. (2020), can have radial density profiles similar to Plummer profiles as seen by the filamentary structure inside the galactic HII region RC 120. This may allow us to easily set up Plummer cylinders of gas that we can then let our star clusters accrete. Furthermore, with the accretion data from H18, we have the accretion rates of gas onto each of their sink particles throughout their simulations. We can use these data to help our simulations more accurately represent GMC simulations by ensuring that our accretion rates match those found in H18.

Another method by which to include the ambient environment in our simulations is through background gas representative of the local GMC around these subclusters. Previous studies have been conducted in which the star cluster as a whole (stars and gas) has been modelled using an analytic potential energy function which is allowed to move through a medium of gas (e.g Naiman et al. 2011). Other studies which have included individual stars have not only omitted the gas component of their star clusters, but

have also only included ≈ 32 stars all of equal mass (e.g Kaaz et al. 2019) which is not representative of the subclusters that form in the GMCs. We can improve this by taking our star clusters comprised of stars and gas and allowing them to travel through ambient gas. We can apply similar analysis techniques as those used here to see how a subcluster responds to constant interactions with an ambient medium. For example, at $T = 10$K, the sound speed in GMCs is on the order of 0.2kms^{-1} which is fairly small compared to the velocity the subclusters travel through the GMC with implying that shocks may arise in the gas component of our star clusters. These shocks may, in turn, have an affect on the overall dynamical evolution of the subclusters as they travel through the GMC environment as the kinetic energy of the gas is irreversibly turned into heat.

Our future work also involves the implementation of stellar feedback effects in our gas accretion and merger simulations. As stated in chapter 1, stellar feedback plays a vital role in the survival of a star cluster after its birth in a GMC. Gas expulsion from stellar feedback has been found to be a vital part of star cluster evolution (e.g Baumgardt and Kroupa 2007, Krause et al. 2016) and resolving subcluster formation with stellar feedback would allow us to understand what the sink particle prescription is masking with regards to this expulsion and how it affects the merger process. Not only would the implementation of stellar feedback effects help our clusters become more realistic, they would allow us to run our simulations for longer times. Right now, we cannot run our simulations beyond 3Myr due to our choice to not include supernovae which occur $\approx$ 3Myr after the birth of a massive star (e.g Meynet and Maeder 2003). This would allow us to investigate multiple merger in a single simulation and how this affects the resultant star cluster. Furthermore, we can analyze how stellar feedback effects influence the accretion of gas onto our star clusters and how this influences the overall star formation efficiency of our clusters.

Finally, once we have included stellar feedback in our merger and future gas accretion

simulations, we aim to study all the important star cluster evolution mechanisms in one single simulation. This will involve taking the sink particles from H18 and re-simulating their entire evolution through the GMC using our new star cluster model (stars and gas). We will finally be able to see how a star cluster responds to all of the important evolutionary mechanisms it undergoes inside the GMC environment.

Bibliography

Aarseth, S. J. (1974). Dynamical evolution of simulated star clusters. I. Isolated models. *Astronomy and Astrophysics* 35, 237–250.

Allison, R. J., Goodwin, S. P., Parker, R. J., Portegies Zwart, S. F., and de Grijs, R. (2010). The early dynamical evolution of cool, clumpy star clusters. *Monthly Notices of the Royal Astronomical Society* 407, 1098–1107.

André, P., Di Francesco, J., Ward-Thompson, D., Inutsuka, S. .-I., Pudritz, R. E., and Pineda, J. E. (2014). From Filamentary Networks to Dense Cores in Molecular Clouds: Toward a New Paradigm for Star Formation. In: *Protostars and Planets VI*. Ed. by H. Beuther, R. S. Klessen, C. P. Dullemond, and T. Henning, 27.

Banerjee, S. and Kroupa, P. (2015). The formation of NGC 3603 young starburst cluster: 'prompt' hierarchical assembly or monolithic starburst? *Monthly Notices of the Royal Astronomical Society* 447, 728–746.

Banerjee, S. and Kroupa, P. (2017). How can young massive clusters reach their present-day sizes? *Astronomy and Astrophysics* 597 A28, A28.

Barnes, J. and Hut, P. (1986). A hierarchical O(N log N) force-calculation algorithm. *Nature Astronomy* 324, 446–449.

Baumgardt, H. and Kroupa, P. (2007). A comprehensive set of simulations studying the influence of gas expulsion on star cluster evolution. *Monthly Notices of the Royal Astronomical Society* 380, 1589–1598.

Bertoldi, F. and McKee, C. F. (1992). Pressure-confined Clumps in Magnetized Molecular Clouds. *Astrophysical Journal* 395, 140.

Bleuler, A. and Teyssier, R. (2014). Towards a more realistic sink particle algorithm for the RAMSES CODE. *Monthly Notices of the Royal Astronomical Society* 445, 4015–4036.

Bovy, J. (2015). galpy: A python Library for Galactic Dynamics. *Astrophysical Journal Supplement* 216 29, 29.

Cartwright, A. and Whitworth, A. P. (2004). The statistical analysis of star clusters. *Monthly Notices of the Royal Astronomical Society* 348, 589–598.

Chabrier, G. (2005). The Initial Mass Function: From Salpeter 1955 to 2005. In: *The Initial Mass Function 50 Years Later*. Ed. by E. Corbelli, F. Palla, and H. Zinnecker. Vol. 327, 41.

Chen, Y., Li, H., and Vogelsberger, M. (2021). Effects of initial density profiles on massive star cluster formation in giant molecular clouds. *Monthly Notices of the Royal Astronomical Society* 502, 6157–6169.

Courant, R., Friedrichs, K., and Lewy, H. (1967). On the Partial Difference Equations of Mathematical Physics. *IBM Journal of Research and Development* 11, 215–234.

Cournoyer-Cloutier, C., Tran, A., Lewis, S., Wall, J. E., Harris, W. E., Mac Low, M.-M., McMillan, S. L. W., Portegies Zwart, S., and Sills, A. (2021). Implementing primordial binaries in simulations of star cluster formation with a hybrid MHD and direct N-body method. *Monthly Notices of the Royal Astronomical Society* 501, 4464–4478.

Dobbs, C. L., Bending, T. J. R., Pettitt, A. R., and Bate, M. R. (2021). The formation of massive stellar clusters in converging galactic flows with photoionisation. *arXiv e-prints* arXiv:2110.09201, arXiv:2110.09201.

Dobbs, C. L., Liow, K. Y., and Rieder, S. (2020). The formation of young massive clusters by colliding flows. *Monthly Notices of the Royal Astronomical Society* 496, L1–L5.

Duncan, M. J., Levison, H. F., and Lee, M. H. (1998). A Multiple Time Step Symplectic Algorithm for Integrating Close Encounters. *Astronomical Journal* 116, 2067–2077.

Elson, R. A. W., Fall, S. M., and Freeman, K. C. (1987). The Structure of Young Star Clusters in the Large Magellanic Cloud. *The Astrophysical Journal* 323, 54.

Evans Neal J., I., Dunham, M. M., Jørgensen, J. K., Enoch, M. L., Merín, B., van Dishoeck, E. F., Alcalá, J. M., Myers, P. C., Stapelfeldt, K. R., Huard, T. L., Allen, L. E., Harvey, P. M., van Kempen, T., Blake, G. A., Koerner, D. W., Mundy, L. G., Padgett, D. L., and Sargent, A. I. (2009). The Spitzer c2d Legacy Results: Star-Formation Rates and Efficiencies; Evolution and Lifetimes. *Astrophysical Journal Supplement* 181, 321–350.

Federrath, C., Banerjee, R., Clark, P. C., and Klessen, R. S. (2010). Modeling Collapse and Accretion in Turbulent Gas Clouds: Implementation and Comparison of Sink Particles in AMR and SPH. *The Astrophysical Journal* 713, 269–290.

Feigelson, E. D., Townsley, L. K., Broos, P. S., Busk, H. A., Getman, K. V., King, R. R., Kuhn, M. A., Naylor, T., Povich, M. S., Baddeley, A., Bate, M. R., Indebetouw, R., Luhman, K. L., McCaughrean, M. J., Pittard, J. M., Pudritz, R. E., Sills, A., Song, Y., and Wadsley, J. (2013). Overview of the Massive Young Star-Forming Complex Study in Infrared and X-Ray (MYStIX) Project. *Astrophysical Journal Supplement* 209 26, 26.

Fryxell, B., Olson, K., Ricker, P., Timmes, F. X., Zingale, M., Lamb, D. Q., MacNeice, P., Rosner, R., Truran, J. W., and Tufo, H. (2000). FLASH: An Adaptive Mesh Hydrodynamics Code for Modeling Astrophysical Thermonuclear Flashes. *Astrophysical Journal Supplement* 131, 273–334.

Fujii, M. S., Saitoh, T. R., and Portegies Zwart, S. F. (2012). The Formation of Young Dense Star Clusters through Mergers. *The Astrophysical Journal* 753 85, 85.

Fujii, M., Iwasawa, M., Funato, Y., and Makino, J. (2007). BRIDGE: A Direct-Tree Hybrid N-Body Algorithm for Fully Self-Consistent Simulations of Star Clusters and Their Parent Galaxies. *PASJ* 59, 1095.

Fukushima, H. and Yajima, H. (2021). Radiation hydrodynamics simulations of massive star cluster formation in giant molecular clouds. *Monthly Notices of the Royal Astronomical Society* 506, 5512–5539.

Gingold, R. A. and Monaghan, J. J. (1977). Smoothed particle hydrodynamics: theory and application to non-spherical stars. *Monthly Notices of the Royal Astronomical Society* 181, 375–389.

Gnedin, O. Y. and Ostriker, J. P. (1997). Destruction of the Galactic Globular Cluster System. *Astrophysical Journal* 474, 223–255.

Grudić, M. Y., Guszejnov, D., Hopkins, P. F., Lamberts, A., Boylan-Kolchin, M., Murray, N., and Schmitz, D. (2018). From the top down and back up again: star cluster structure from hierarchical star formation. *Monthly Notices of the Royal Astronomical Society* 481, 688–702.

Guszejnov, D., Grudoć, M. Y., Hopkins, P. F., Offner, S. S. R., and Faucher-Giguère, C.-A. (2020). Can Magnetized Turbulence Set the Mass Scale of Stars? *Monthly Notices of the Royal Astronomical Society* 496, 364–378.

Heggie, D. C. and Mathieu, R. D. (1986). Standardised Units and Time Scales. In: *The Use of Supercomputers in Stellar Dynamics*. Ed. by P. Hut and S. L. W. McMillan. Vol. 267, 233.

Heiderman, A., Evans Neal J., I., Allen, L. E., Huard, T., and Heyer, M. (2010). The Star Formation Rate and Gas Surface Density Relation in the Milky Way: Implications for Extragalactic Studies. *Astrophysical Journal* 723, 1019–1037.

Howard, C. S., Pudritz, R. E., and Harris, W. E. (2017). Simulating radiative feedback and star cluster formation in GMCs - II. Mass dependence of cloud destruction and cluster properties. *Monthly Notices of the Royal Astronomical Society* 470, 3346–3358.

Howard, C. S., Pudritz, R. E., and Harris, W. E. (2018). A universal route for the formation of massive star clusters in giant molecular clouds. *Nature Astronomy* 2, 725–730.

Kaaz, N., Antoni, A., and Ramirez-Ruiz, E. (2019). Bondi-Hoyle-Lyttleton Accretion onto Star Clusters. *Astrophysical Journal* 876 142, 142.

King, I. (1962). The structure of star clusters. I. an empirical density law. *Astronomical Journal* 67, 471.

King, I. R. (1966). The structure of star clusters. III. Some simple dynamical models. *The Astronomical Journal* 71, 64.

Könyves, V., André, P., Men'shchikov, A., Schneider, N., Arzoumanian, D., Bontemps, S., Attard, M., Motte, F., Didelon, P., Maury, A., Abergel, A., Ali, B., Baluteau, J. .-P., Bernard, J. .-P., Cambrésy, L., Cox, P., di Francesco, J., di Giorgio, A. M., Griffin, M. J., Hargrave, P., Huang, M., Kirk, J., Li, J. Z., Martin, P., Minier, V., Molinari, S., Olofsson, G., Pezzuto, S., Russeil, D., Roussel, H., Saraceno, P., Sauvage, M., Sibthorpe, B., Spinoglio, L., Testi, L., Ward-Thompson, D., White, G., Wilson, C. D., Woodcraft, A., and Zavagno, A. (2010). The Aquila prestellar core population revealed by Herschel. *Astronomy and Astrophysics* 518 L106, L106.

Krause, M. G. H., Charbonnel, C., Bastian, N., and Diehl, R. (2016). Gas expulsion in massive star clusters?. Constraints from observations of young and gas-free objects. *Astronomy and Astrophysics* 587 A53, A53.

Kroupa, P. (2001). On the variation of the initial mass function. *Monthly Notices of the Royal Astronomical Society* 322, 231–246.

Kuhn, M. A., Feigelson, E. D., Getman, K. V., Baddeley, A. J., Broos, P. S., Sills, A., Bate, M. R., Povich, M. S., Luhman, K. L., Busk, H. A., Naylor, T., and King, R. R. (2014). The Spatial Structure of Young Stellar Clusters. I. Subclusters. *Astrophysical Journal* 787 107, 107.

Lada, C. J., Forbrich, J., Lombardi, M., and Alves, J. F. (2012). Star Formation Rates in Molecular Clouds and the Nature of the Extragalactic Scaling Relations. *Astrophysical Journal* 745 190, 190.

Lada, C. J. and Lada, E. A. (2003). Embedded Clusters in Molecular Clouds. *Annual Reviews of Astronomy and Astrophysics* 41, 57–115.

Lada, C. J., Lombardi, M., and Alves, J. F. (2010). On the Star Formation Rates in Molecular Clouds. *Astrophysical Journal* 724, 687–693.

Lahén, N., Naab, T., Johansson, P. H., Elmegreen, B., Hu, C.-Y., and Walch, S. (2020a). Structure and Rotation of Young Massive Star Clusters in a Simulated Dwarf Starburst. *Astrophysical Journal* 904 71, 71.

Lahén, N., Naab, T., Johansson, P. H., Elmegreen, B., Hu, C.-Y., Walch, S., Steinwandel, U. P., and Moster, B. P. (2020b). The GRIFFIN Project—Formation of Star Clusters with Individual Massive Stars in a Simulated Dwarf Galaxy Starburst. *Astrophysical Journal* 891 2, 2.

Levenberg, K. (1944). A method for the solution of certain non-linear problems in least squares. *Quart. Appl. Math.* 2, 164–168.

Mackey, A. D. and Gilmore, G. F. (2003a). Surface brightness profiles and structural parameters for 53 rich stellar clusters in the Large Magellanic Cloud. *Monthly Notices of the Royal Astronomical Society* 338, 85–119.

Mackey, A. D. and Gilmore, G. F. (2003b). Surface brightness profiles and structural parameters for 53 rich stellar clusters in the Large Magellanic Cloud. *Monthly Notices of the Royal Astronomical Society* 338, 85–119.

Makino, J. and Aarseth, S. J. (1992). On a Hermite Integrator with Ahmad-Cohen Scheme for Gravitational Many-Body Problems. *PASJ* 44, 141–151.

Matzner, C. D. and McKee, C. F. (2000). Efficiencies of Low-Mass Star and Star Cluster Formation. *Astrophysical Journal* 545, 364–378.

Meynet, G. and Maeder, A. (2003). Stellar evolution with rotation. X. Wolf-Rayet star populations at solar metallicity. *Astronomy and Astrophysics* 404, 975–990.

Monaghan, J. J. (1992). Smoothed particle hydrodynamics. *Annual Reviews of Astronomy and Astrophysics* 30, 543–574.

Naiman, J. P., Ramirez-Ruiz, E., and Lin, D. N. C. (2011). External Mass Accumulation onto Core Potentials: Implications for Star Clusters, Galaxies, and Galaxy Clusters. *Astrophysical Journal* 735 25, 25.

Parker, R. J. and Meyer, M. R. (2012). Characterizing the dynamical state of star clusters from snapshots of their spatial distributions. *Monthly Notices of the Royal Astronomical Society* 427, 637–650.

Pelupessy, F. I. and Portegies Zwart, S. (2012). The evolution of embedded star clusters. *Monthly Notices of the Royal Astronomical Society* 420, 1503–1517.

Pelupessy, F. I., van Elteren, A., de Vries, N., McMillan, S. L. W., Drost, N., and Portegies Zwart, S. F. (2013). The Astrophysical Multipurpose Software Environment. *Astronomy and Astrophysics* 557 A84, A84.

Plummer, H. C. (1911). On the problem of distribution in globular star clusters. *Monthly Notices of the Royal Astronomical Society* 71, 460–470.

Portegies Zwart, S., McMillan, S. L. W., van Elteren, E., Pelupessy, I., and de Vries, N. (2013). Multi-physics simulations using a hierarchical interchangeable software interface. *Computer Physics Communications* 184, 456–468.

Portegies Zwart, S. and McMillan, S. (2018). *Astrophysical Recipes; The art of AMUSE*.

Portegies Zwart, S., McMillan, S., Harfst, S., Groen, D., Fujii, M., Nualláin, B. Ó., Glebbeek, E., Heggie, D., Lombardi, J., Hut, P., Angelou, V., Banerjee, S., Belkus, H., Fragos, T., Fregeau, J., Gaburov, E., Izzard, R., Jurić, M., Justham, S., Sottoriva, A., Teuben, P., van Bever, J., Yaron, O., and Zemp, M. (2009). A multiphysics and multiscale software environment for modeling astrophysical systems. *New Astronomy* 14, 369–378.

Portegies Zwart, S. F., McMillan, S. L. W., and Gieles, M. (2010). Young Massive Star Clusters. *Annual Reviews of Astronomy and Astrophysics* 48, 431–493.

Salpeter, E. E. (1955). The Luminosity Function and Stellar Evolution. *Astrophysical Journal* 121, 161.

Schmeja, S. and Klessen, R. S. (2006). Evolving structures of star-forming clusters. *Astronomy and Astrophysics* 449, 151–159.

Sills, A., Rieder, S., Scora, J., McCloskey, J., and Jaffa, S. (2018). Dynamical evolution of stars and gas of young embedded stellar sub-clusters. *Monthly Notices of the Royal Astronomical Society* 477, 1903–1912.

Spitzer Lyman, J. (1940). The stability of isolated clusters. *Monthly Notices of the Royal Astronomical Society* 100, 396.

Spitzer Lyman, J. and Hart, M. H. (1971). Random Gravitational Encounters and the Evolution of Spherical Systems. I. Method. *The Astrophysical Journal* 164, 399.

Springel, V. (2005). The cosmological simulation code GADGET-2. *Monthly Notices of the Royal Astronomical Society* 364, 1105–1134.

Springel, V. and Hernquist, L. (2002). Cosmological smoothed particle hydrodynamics simulations: the entropy equation. *Monthly Notices of the Royal Astronomical Society* 333, 649–664.

Stahler, S. W. and Palla, F. (2004). *The Formation of Stars*.

Trumpler, R. J. (1930). Preliminary results on the distances, dimensions and space distribution of open star clusters. *Lick Observatory Bulletin* 420, 154–188.

Vázquez-Semadeni, E., González-Samaniego, A., and Colín, P. (2017). Hierarchical star cluster assembly in globally collapsing molecular clouds. *Monthly Notices of the Royal Astronomical Society* 467, 1313–1328.

von Hoerner, S. (1957). Internal structure of globular clusters. *Astrophysical Journal* 125, 451.

Wall, J. E., McMillan, S. L. W., Mac Low, M.-M., Klessen, R. S., and Portegies Zwart, S. (2019). Collisional N-body Dynamics Coupled to Self-gravitating Magnetohydrodynamics Reveals Dynamical Binary Formation. *Astrophysical Journal* 887 62, 62.

Whitehead, A. J., McMillan, S. L. W., Vesperini, E., and Portegies Zwart, S. (2013). Simulating Star Clusters with the AMUSE Software Framework. I. Dependence of Cluster Lifetimes on Model Assumptions and Cluster Dissolution Modes. *The Astrophysical Journal* 778 118, 118.

Wisdom, J. and Holman, M. (1991). Symplectic maps for the N-body problem. *Astronomical Journal* 102, 1528–1538.

Zavagno, A., André, P., Schuller, F., Peretto, N., Shimajiri, Y., Arzoumanian, D., Csengeri, T., Figueira, M., Fuller, G. A., Könyves, V., Men'shchikov, A., Palmeirim, P., Roussel, H., Russeil, D., Schneider, N., and Zhang, S. (2020). The role of Galactic H II regions in the formation of filaments. High-resolution submilimeter imaging of RCW 120 with ArTéMiS. *Astronomy and Astrophysics* 638 A7, A7.

Zeidler, P., Sabbi, E., Nota, A., and McLeod, A. F. (2021). The Young Massive Star Cluster Westerlund 2 Observed with MUSE. III. A Cluster in Motion—The Complex Internal Dynamics. *The Astronomical Journal* 161(3) 140, 140.

Zhang, Q., Fall, M. S., and Whitmore, B. C. (2001). A Multiwavelength Study of the Young Star Clusters and Interstellar Medium in the Antennae Galaxies. *Astrophysical Journal* 561, 727–750.

Zocchi, A., Bertin, G., and Varri, A. L. (2012). A dynamical study of Galactic globular clusters under different relaxation conditions. *Astronomy and Astrophysics* 539 A65, A65.